A Dissertation

entitled

Toward Realistic Stiffness-Matched NiTi Skeletal Fixation Plates

by

Ahmadreza Jahadakbar

Submitted to the Graduate Faculty as partial fulfillment of the requirements for the

Doctor of Philosophy Degree in

Mechanical Engineering

_____

Dr. Mohammad Elahinia, Committee Chair

_____

Dr. David Dean, Committee Member

_____

Dr. Matthew J. Franchetti, Committee Member

_____

Dr. Mohammad Mahtabi, Committee Member

_____

Dr. Reza Rizvi, Committee Member

_____

Dr. Amanda Bryant-Friedrich, Dean
College of Graduate Studies

The University of Toledo

May 2020

An Abstract of

Toward Realistic Stiffness-Matched NiTi Skeletal Fixation Plates

by

Ahmadreza Jahadakbar

Submitted to the Graduate Faculty as partial fulfillment of the requirements for the
Doctor of Philosophy Degree in
Mechanical Engineering

The University of Toledo
May 2020

The standard of care for mandibular segmental defects is the use of Ti-6Al-4V (i.e. surgical grade 5 Titanium or Ti64) skeletal fixation plates and screws. There is a significant stiffness mismatch between the Ti64 skeletal fixation plates and the cortical bone. Although these high stiff Ti64 skeletal fixation plates provide enough immobilization immediately after the surgery, when the bones heal, the high level of stiffness disturbs the loading distribution. The result is stress shielding in the surrounding bone which may lead to bone resorption and eventually could lead to failure of the surgery.

NiTi (i.e. Nickel-Titanium or Nitinol) is a biocompatible, shape memory alloy that offers interesting features, such as superelasticity. Additionally, NiTi has a lower stiffness than Ti64 which can be further reduced by imposing porosity. With the proper choice of the level and type of porosity, one can reduce the NiTi stiffness to that of the cortical bone. Thanks to the superelastic property of NiTi, the risk of stress concentration and increased strain levels due to imposing porosity does not lead to early failure of the

porous NiTi structure than if it were formed from Ti64. Therefore, making superelastic NiTi a more suitable candidate for such applications.

Additive manufacturing (AM) is a relatively new method of fabrication that enables the fabrication of parts directly from a CAD file. In this method, the CAD file is sliced into thin layers, and then the part is fabricated in a layer-by-layer approach. Recently, additive manufacturing has been used for the fabrication of NiTi parts. It is, therefore, possible to fabricate complex-shape porous NiTi components such as the devices for mandibular segmental repair surgery.

As a solution to the stress shielding problem of the mandibular reconstruction surgery, in this work, we have introduced NiTi patient-specific, stiffness matched bone fixation plates. The proposed bone fixation plates are designed based on a 3D model of the patient and their stiffness is adjusted by imposing porosity to the level of the patient's cortical bone. Thus, the stiffness and geometry are designed based on CT scan data of the patient's mandible. Eventually, additive manufacturing is used for the fabrication of the patient-specific, stiffness-matched porous NiTi skeletal fixation plates.

In this dissertation, after providing a comprehensive literature review on NiTi, additive manufacturing technique, and mandibular reconstruction surgery, the proposed skeletal fixation plates are introduced, and the first generation is designed, modeled, and fabricated via the AM technique. The first generation provides a simplified geometry and is used to show the possibility of design and fabrication of skeletal fixation plates with the engineered level of porosity. As a first step toward biocompatibility, the corrosion response of the implants is investigated.

Using the results of the first generation, and to achieve superelastic skeletal fixation plates Ni-rich powder (i.e. Ni50.8Ti at. %) is used for the second generation of the skeletal fixation plates. The overall geometry, pore size, and shape of the implants improved in the second generation. In order to evaluate the thermomechanical properties, a skeletal fixation plate with the critical dimensions and level of porosity was designed and fabricated. A chemical polishing methodology developed to remove the un-melted powders fused to the internal surfaces and to improve the dimensional accuracy with respect to the computer model. Using standard samples, the mechanical properties of the skeletal fixation plates were predicted and showed good compatibility with the polished skeletal fixation plates. As an additional evaluation step, the chemical composition of the fabricated skeletal fixation plates analyzed based on ASTM standards and compared with that of the conventionally fabricated NiTi.

Followed by evaluating the skeletal fixation plates and based on the literature, we investigated the effect of laser re-melting on the surface condition and on the relative density of the AM fabricated parts. By evaluating a series of re-melting procedures, we obtained optimized process parameters that increased the relative density by 1 % and improved the surface condition. The effect of re-melting was further investigated by analyzing the thermomechanical features and SEM observations.

Eventually, to improve the homogeneity of the AM fabricated NiTi parts, improve the superelasticity, and to further modulate the thermomechanical properties, we conducted a series of heat treatment procedures on the samples. It was observed that by utilizing heat treatment procedures, different thermomechanical and superelastic properties can be achieved that significantly affect the performance of the implants at

body temperature. In addition to the thermomechanical behavior of the heat-treated parts, we performed initial microstructural studies for a better understanding of the heat treatment procedure.

This dissertation is dedicated to my beautiful wife, Parisa, who has been a constant source of support and encouragement during the challenges of graduate school and life. I am truly thankful for having you in my life. This work is also dedicated to my family, who have always loved me unconditionally and whose good examples have taught me to work hard for the things that I aspire to achieve...

Acknowledgements

First and foremost, I would like to express my sincere gratitude to my Ph.D. advisor Prof. Mohammad Elahinia for the endless support, patience, motivation, immense knowledge, and invaluable experiences. His mentorship and precious guidance significantly helped me both as an individual and a researcher. He provided me with so many opportunities that allowed me to grow and I could not have imagined having a better advisor and mentor for my graduate school.

A special thanks to Dr. David Dean who provided me with insightful biomedical and surgical inputs and for serving as a committee member for my dissertation. I would like to thank my other committee members Dr. Reza Rizvi, Dr. Mohammad Mahtabi, and Dr. Matthew Franchetti for their precious comments, guidance, and support.

I thank my fellow lab-mates for the stimulating discussions, for all the projects that we did together, for all the help, and for all the fun we have had in the last six years. I also appreciate the generous help of other professors, technicians, and staff of the College of Engineering at The University of Toledo.

Words are not enough to express how grateful I am to my wife, Parisa, who has also been the best lab-mate that I could ever ask for, and to my amazing family, particularly my parents, and my sister for their love, support, and constant encouragement, I have gotten over the years.

Table of Contents

List of Tables

List of Figures

Chapter 1

1. Introduction

The field of biomaterials is constantly developing and evolving in a search for better solutions. Biomaterials are used in different parts of the human body with temporary to long-lasting applications. There are different concerns and parameters that must be considered for biocompatible materials based on their applications. High strength, ductility, low level of stiffness, and high corrosion and wear resistance are some of the most important required features of biocompatible materials [1]. 316 stainless steel, titanium (Ti-6AL-4V) and cobalt-chromium are some of the most common metals used for long-lasting applications. These metals usually have a high level of strength and benefit from an acceptable corrosion resistance that makes them good biocompatible candidates [1].

In order to minimize the release of non-compatible metals ions by the implants into the body, the base material must have a high wear and corrosion resistance. These ions can accumulate in adjacent tissues and transport to other parts of the body and cause allergic and toxic reactions [2]. Low wear resistance might cause aseptic loosening of components and the resulting wear debris leads to an adverse inflammatory response in

the tissues [2]. Biocompatibility of the material must be evaluated to assess any potential inflammatory or allergic reaction in the body. The host response to the material and material degradation in the body are the two main factors that affect the biocompatibility of a material [3]. Similarly, to evaluate these factors the material response and degradation in body fluid must be studied. An ideal biocompatible skeletal fixation or bone replacement material has a minimum corrosion and therefore negligible metal ion release and has minimum wear and negligible release of debris [3].

Osseointegration is another important factor for materials used as internal bone implants. Osseointegration is the ability of an implant surface to attach to the adjacent bone tissues and create an integrated region. An implant with poor osseointegration does not fuse to the bones and could be loosened. In this case, unwanted fibrous tissues develop between the bone and the implant and cause infection [3].

Joint replacements for knees, hips, and elbows, as well as dental and other implants, are predominantly made of biocompatible metals [4]. Although these metals provide high levels of strength, they usually have a high stiffness in comparison with the targeted body tissues. This mismatch between the levels of stiffness disturbs the load distribution on the adjacent bone and causes bone deformations. In addition, bone material is able to recover up to 2% of strain and restore back to its original shape after deformation or impact forces [5]. This feature provides a high energy absorption rate for the bone tissue and delays failure of bones. Unlike the bone, the conventional metallic implants are only able to recover low levels of strains (i.e. less than 2 percent) and because of this mismatch mechanical failure is a common issue [6].

1.1 Problem statement

Mandibular reconstruction surgery for patients with trauma, tumors, or cancer, is an example of the cases where the mismatch between the level of stiffness of the bone tissue and metallic implants could lead to major complications that could necessitate revision surgeries. In this surgery, after resecting the defective region of the mandibular bone, a healthy piece of bone is used for filling the gap, and eventually metallic fixations and screws are used for immobilizing the mandible. Although immediately after the surgery this metallic fixation system provides enough immobilization, after the bones heal, due to the mismatch between the levels of stiffness stress shielding happens in the affected bone that could lead to bone resorption and eventually failure of the surgery.

1.2 Objectives

In a search for a biocompatible, lightweight, material that can undergo large deformation without failure and also has a closer level of stiffness to the bone tissues, we have suggested the use of NiTi (a Nickel-titanium alloy, also called Nitinol). NiTi is a shape memory alloy that has unique properties. By modifying the geometry (e.g. imposing porosity) and using a relatively new method of fabrication (i.e. additive manufacturing) we have introduced stiffness matched NiTi implants that minimize stress shielding and prevent bone resorption.

The main objectives of this project can be summarized as below.

1. Modeling and finite element simulation of the mandibular reconstruction surgery using the conventional skeletal fixation plates
2. Designing of the patient-specific, stiffness-matched skeletal fixation plates based on computed tomography (CT) scan data

3. Modeling the reconstruction surgery with the proposed skeletal fixation plates and comparing with the conventional implants
4. Designing the standard-shape skeletal fixation plates with a varying stiffness that can be fabricated via selective laser melting and mechanically tested
5. Fabricating the required samples for mechanical evaluation and corrosion assessment
6. Mechanically evaluating the fabricated samples under realistic loading condition
7. Finite element modeling the samples fabricated for mechanical testing and verifying the simulations
8. Evaluating the corrosion resistance of the additively manufactured porous NiTi parts and comparing with the conventional ones
9. Evaluating the chemical composition of the AM fabricated skeletal fixation plates based on standards as the first step toward biocompatibility
10. Investigating a chemical polishing methodology to remove the un-melted powder particles fused to the surface of the parts
11. Achieving superelasticity and optimizing the mechanical properties by utilizing Ni-rich NiTi powder as well as heat treatment
12. Improving the surface condition and relative density of the AM fabricated parts by developing and utilizing a re-melting approach
13. Improving the superelasticity and optimizing the mechanical properties by investigating a heat treatment mechanism

1.3 Approach

At first, a comprehensive literature review is conducted on three different subjects. (I) Thermomechanical properties of NiTi as a shape memory alloy, its unique

properties and the applications in medical devices. (II) Additive manufacturing as a relatively new method of fabrication that has recently been used for fabrication of NiTi components. (III) Mandibular reconstruction surgery, classifications, challenges, and state of the art.

Next, we modeled the reconstruction surgery using a mandible model created based on CT scan data. The model includes cortical and cancellous bone, teeth, periodontal ligaments, and muscle forces. Different types of skeletal fixation plates were later assessed using this finite element model. We also calibrated a user material subroutine (UMAT) to simulate the thermomechanical response of NiTi components in our models [7, 8].

Stiffness matched skeletal fixation plates were designed and modeled under realistic loading conditions. Realistic muscle forces were used for modeling the chewing process. Finite element simulations were used for evaluating the proposed skeletal fixation plates [8].

The designed skeletal fixation plates, as well as a set of standard-shape skeletal fixation plates with varying levels of stiffness, were fabricated using selective laser melting method. In addition, two sets of samples for immersion and electrochemical evaluation of the additively manufactured skeletal fixation plates were fabricated [9, 10].

The fabricated skeletal fixation plates with the standard shape were mechanically evaluated via tensile test at body temperature. The results were then compared with the computer simulations of the samples, as a verification step. Electrochemical and immersion tests were used for corrosion assessments of the additively manufactured NiTi parts [9, 10].

By changing the powder and adding more details to the design of the skeletal fixation plates, the second generation of skeletal fixation plates with superelastic response were achieved. A non-mechanical chemical polishing methodology developed to remove the un-melted powder fused to the surface of the part and to improve the geometrical accuracy of the parts. The geometrical accuracy of the polished skeletal fixation plates investigates verified via mechanical testing. Chemical composition of the final parts was also investigated based on ASTM standards [10].

In order to improve the relative density as well as the surface condition of the AM parts, a study was designed to investigate the effect of re-melting process on the additive manufactured NiTi parts. The re-melted parts analyzed by density measurements, surface roughness measurements, and thermomechanical assessments.

Eventually, in order to homogenize the AM fabricated parts, improve the superelasticity, and to further tune the mechanical properties, a study designed to study the effect of a series of heat treatment on the AM fabricated parts.

1.4 Outline

Chapter 1 presents the motivation and objectives of this research work. A general idea of the research approach is proposed, as well. Chapter 2 provides a comprehensive literature review for the project. Chapter 3 discusses the methods used for the design, fabrication, simulations, and experiments. Chapter 4 presents the results of the designs, simulations, as well as experiments. Eventually, chapter 5 presents the summary, conclusion and the suggested future works.

1.5 Contributions

Thanks to the unique properties of NiTi, as well as the ultimate freedom provided by additive manufacturing, realistic stiffness matched skeletal fixation plates were introduced, designed, fabricated and mechanically evaluated. The corrosion resistance of the additively manufactured NiTi parts was also evaluated for the first time.

In addition to this thesis, a utility patent has been filed on this project. The patent has been licensed by a university-based startup company, “RegenFix, LLC”. The company is moving toward commercialization of this product through an animal study, FDA submission and working on good manufacturing practice (GMP).

1.6 Publications

To this date, the journal publications that have resulted from this study are listed in this section. There are an additional conference papers and presentations that are not listed [11, 12].

1. Jahadakbar, Ahmadreza, Mohammadreza Nematollahi, Keyvan Safaei, Parisa Bayati, Govind Giri, Hediyeh Dabbaghi, David Dean, and Mohammad Elahinia. "Design, Modeling, Additive Manufacturing, and Polishing of Stiffness-Modulated Porous Nitinol Bone Fixation Plates Followed by Thermomechanical and Composition Analysis." Metals 10, no. 1 (2020): 151. [10]
2. Jahadakbar, Ahmadreza, Narges Shayesteh Moghaddam, Amirhesam Amerinatanzi, David Dean, and Mohammad Elahinia. "Mechanical evaluation of the SLM fabricated, stiffness-matched, mandibular bone fixation plates." In Behavior and Mechanics of Multifunctional Materials and Composites XII, vol. 10596, p. 1059610. International Society for Optics and Photonics, 2018. [13]

3. Ibrahim, Hamdy, Ahmadreza Jahadakbar, Amir Dehghan, Narges Shayesteh Moghaddam, Amirhesam Amerinatanzi, and Mohammad Elahinia. "*In Vitro* Corrosion Assessment of Additively Manufactured Porous NiTi Structures for Bone Fixation Applications." Metals 8, no. 3 (2018): 164. [9]
4. Shayesteh Moghaddam, Narges, Ahmadreza Jahadakbar, Amirhesam Amerinatanzi, Roman Skoracki, Michael Miller, David Dean, and Mohammad Elahinia. "Fixation release and the bone Bandaid: A new bone fixation device paradigm." Bioengineering 4, no. 1 (2017): 5. [14]
5. Jahadakbar, Ahmadreza, Narges Shayesteh Moghaddam, Amirhesam Amerinatanzi, David Dean, Haluk E. Karaca, and Mohammad Elahinia. "Finite element simulation and additive manufacturing of stiffness-matched niti fixation hardware for mandibular reconstruction surgery." Bioengineering 3, no. 4 (2016): 36.[15]
6. Moghaddam, Narges Shayesteh, Ahmadreza Jahadakbar, Amirhesam Amerinatanzi, Mohammad Elahinia, Michael Miller, and David Dean. "Metallic fixation of mandibular segmental defects: Graft immobilization and orofacial functional maintenance." Plastic and Reconstructive Surgery Global Open 4, no. 9 (2016). [8]

Chapter 2

2. Literature review

2.1 Shape memory alloys

Shape memory alloys (SMAs) are distinguished from conventional alloys by their ability to exhibit a direct coupling between temperature and mechanical behavior, a thermomechanical coupling. This means that changes in either thermal or mechanical condition of the material, can significantly affect the other domain. Although SMAs are mainly well known for their ability to recover their shape following a large deformation, due to the thermomechanical coupling, they exhibit other interesting features. These unique features, such as shape memory effect and superelasticity enable SMAs to act as solid-state actuators, sensors, and dampers [16, 17].

There are other active materials that exhibit mechanical coupling, such as piezoelectric and electrostrictive (coupled with electric fields), and piezomagnetic and magnetostrictive (coupled with magnetic fields). It is worth noting that among all active materials, SMAs exhibit the highest energy density [18]. This makes SMAs a great candidate for the development of lightweight, high force/displacement sensors and actuators, and for any other application that requires high energy absorption [19-23].

A thermomechanical, solid-state, reversible phase transformation between a high-temperature phase (austenite) and a low-temperature phase (martensite) is the underlying reason for the behavior of SMAs which are the Shape Memory Effect (SME) and the Super Elastic effect (SE) [24]. There are critical temperatures that define the phase stabilities for SMAs. These critical temperatures, also known as transformation temperatures, depend on the material composition, structure, and post-fabrication treatments, such as heat treatments and coldworks. In general, SME occurs when an SMA plastically deforms in its martensitic phase and then recovers its shape in a heating process. On the other hand, an SMA in its austenitic phase is able to recover large deformations (i.e. significantly higher than elastic limits of other materials) right upon unloading without any heating process, which is called the Superelastic Effect. Ag-Cd, Au-Cd, Cu-Al-Ni, Cu-Sn, Cu-Zn-(X), In-Ti, Ni-Al, Ni-Ti, Fe-Pt, Mn-Cu, and Fe-Mn-Si are some of the well-known SMAs.

The shape memory phenomena were first reported by Ölander in Au-Cd in 1932. He described this phenomenon as a rubber-like response [25-27]. In 1938, Greninger and Mooradian observed and reported the formation of a temperature dependent martensitic phase in Cu-Zn alloys [28]. In 1949, Kurdyumov and Khandros [29] reported the crystallographic and kinetic basis for the thermal reversibility of martensite. In 1949, Chang and Read [30] conducted further research on martensitic twins in Au-Cd. Later the thermoelastic phenomena were observed in NiTi compositions and led to the wide popularity of shape memory alloys.

2.2 NiTi

The discovery of the Nickel-Titanium as a shape memory alloy was made quite accidentally in 1963 by Buehler and his colleagues while investigating the heat and corrosion resistance of intermetallic materials for thermal shields at the Naval Ordnance Laboratory (NOL) [31-33]. While the group was investigating the thermal properties of different materials, it was observed that NiTi exhibited very unusual properties including temperature dependent acoustic damping characteristics. This interesting discovery caused extra attention to the NiTi composition by the lab members. In a routine lab meeting, a bent corrugated strip of NiTi recovered its shape to the straightened form while it was heated up by an associate technical director's pipe lighter. Buehler and his colleagues continued to study this surprising observation in NiTi which led to the terms shape memory and nitinol (Ni-Ti-NOL) [34].

NiTi quickly gained attention among scientists and become the most widely used shape memory alloy. By 1970, the researchers could develop a fundamental understanding of the crystallographic mechanisms [35-37], as well as stress-induced martensitic transformations [38, 39]. Most of these researches were conducted on Cu-based alloys because of the low cost and ease of processing single crystals. It should be noted that Cu-based alloys are quite brittle in their polycrystalline state and on the other hand, nitinol has better functional properties [40]. Nitinol benefits from features, such as high ductility, high strain recoverability, excellent corrosion resistance, stable transformation temperatures, relatively low elastic modulus, high biocompatibility and good magnetic resonance imagining [41, 42].

While Nitinol has been used in different applications, the largest market has been the biomedical applications [19, 43, 44]. Orthopedic and cardiovascular devices and orthodontics wires are the main and well-known applications of NiTi. Superelastic NiTi has been used in eyeglass frames and some toys [45]. Sensors and actuators made of NiTi have been widely used in micro-electronic mechanical systems (MEMS) [46]. Solid-state heat engines and shrink-fit pipe couplers for aircraft are the other commercialized applications of NiTi [47]. In the following sections unique mechanical features of NiTi, post-processing, biocompatibility, and its medical applications are discussed in detail.

2.2.1 Transformation Behavior

The shape memory and superelastic properties in NiTi are due to a diffusion-less, solid-solid, first-order phase transformation [46, 48, 49]. Nitinol has two stable temperature-dependent solid phases; a) the parent phase, austenite, which is stable at high temperatures and has an interpenetrating cubic B2 crystal structure, b) martensite, the low-temperature product phase which has a low-symmetry monoclinic B19' structure. The forward transformation from austenite to martensite can either directly happen in a single step, B2 → B19', or as a two-step transformation, B2 → R → B19'. The R-phase is an intermediate phase with a trigonal crystal structure [46, 50]. The existence of the R-phase depends on the composition and material processing. The reverse transformation from martensite to austenite always happens in a single step; B19' → B2 [18]. Moreover, the martensite structure can be organized in two shapes: twinned and detwinned. martensite can have different orientation directions which are called variants. Twinned martensite phase in NiTi is made of several self-accommodating martensitic variants, while detwinned martensite consists of a single, dominant variant. For NiTi, there are 24

possible martensitic variants [18]. During NiTi transformation, there are four important temperatures: austenite start (A_s), austenite finish (A_f), martensite start (M_s), and martensite finish (M_f). These temperatures are called transformation temperatures (TTs).

2.2.2 Phase diagram

In addition to the temperature, the phase stability of NiTi is a function of the applied stress. Stress-temperature phase diagram indicates the transformation temperatures as a function of applied stress. The transformation zones of an SMA with a fixed composition can be recognized using the phase diagram. Figure 2-1 shows the general shape of a phase diagram. As it can be seen in the figure, the transformation temperatures increase in response to applied stress. In addition, the phase stability of NiTi is not only a function of the temperature and stress states of the material, but also depends on load history (hysteretic transformation).

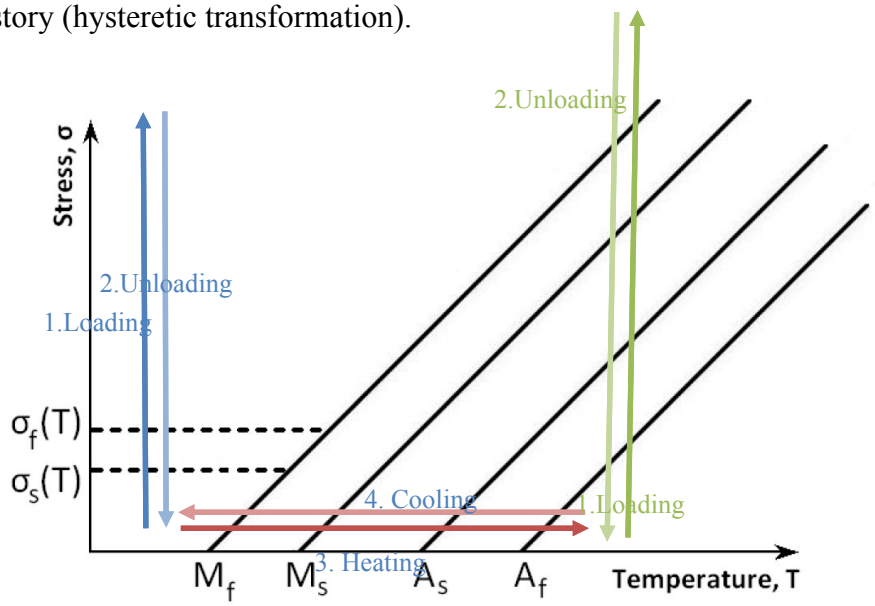

Figure 2-1 Phase Diagram of the transformation temperatures of nitinol as a function of applied stress

The superelasticity and shape memory phenomena can be illustrated by the phase diagram. In Figure 2-1, numbers 1 to 4 in blue show the shape memory response, and

numbers 1 and 2 in green show the superelastic response. The stress-temperature phase diagram is discussed in more details below.

An SMA at a temperature above A_f in a zero-stress state is fully austenite. Cooling the SMA at this stage initiate the forward transformation and the austenite transforms completely to twinned martensite by passing M_f. During the forward transformation, the martensite crystals form in a combination of twenty-four self-accommodating variants and no macroscopic deformation occurs. Heating the sample at this stage, initiate the reverse transformation and following that the twinned martensite transforms to austenite. The reverse transformation starts by passing A_s and concludes at A_f. As it can be seen in Figure 2-2, at a temperature (T) between M_s and A_s the material may exist in either austenite or martensite form which depends on the loading history. If the material is on the forward transformation, %100 austenite exists and if the SMA is on the reverse transformation fully martensite exists (Hysteretic behavior) [18].

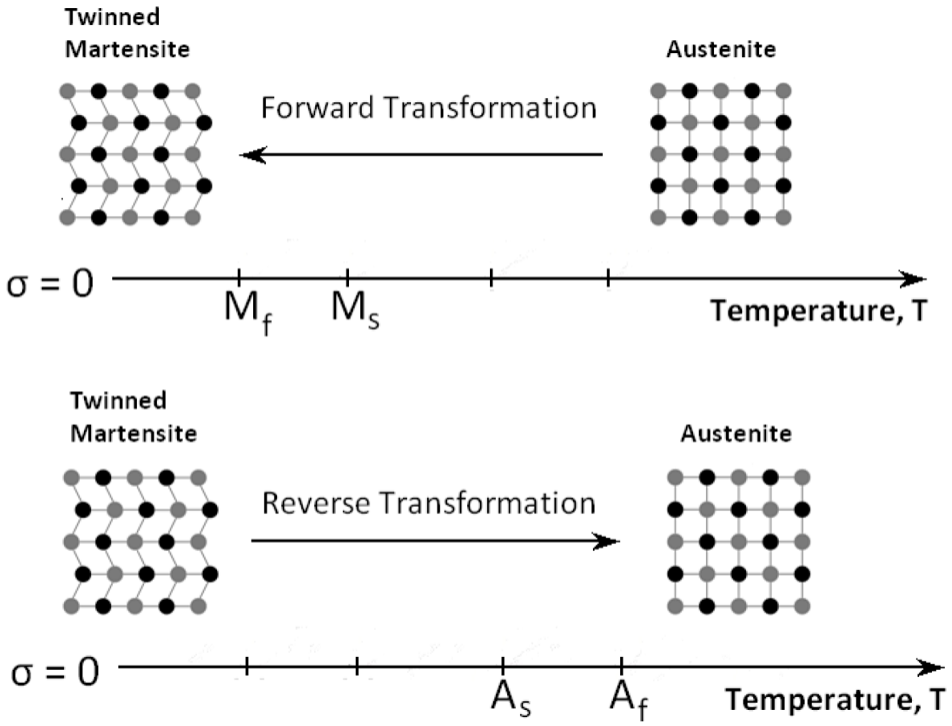

Figure 2-2 Temperature-induced forward phase transformation in a zero stress state _ Temperature-induced reverse phase transformation in a zero stress state [18]

The Shape Memory Effect (SME) causes an SMA to recover its original shape via heating, after a relatively large deformation. To illustrate this effect, first consider an SMA in its austenite parent phase. The SMA at this stage is fully austenite and cooling down the material to a temperature lower than M_f forms twinned martensite (zero-stress cooling). At this stage, loading the SMA with twinned martensite phase, forces the different martensite variants to align into a single, geometrically favorable variant which is called detwinned martensite. During the detwinning process which begins and completes at critical stresses, σ_s and σ_f, a macroscopic deformation happens (Figure 2-3.a). Upon unloading, the SMA remains in the detwinned stage and has been deformed to a second shape (Figure 2-3.b). Finally, heating up the detwinned martensite to a temperature higher than A_f, causes the reverse transformation and the material transforms

to its austenite parent phase (Figure 2-3.c). During this transformation, the SMA recovers the macroscopic deformation caused by the detwinning process, and reforms to its original shape. This process can be seen in Figure 2-3 [18].

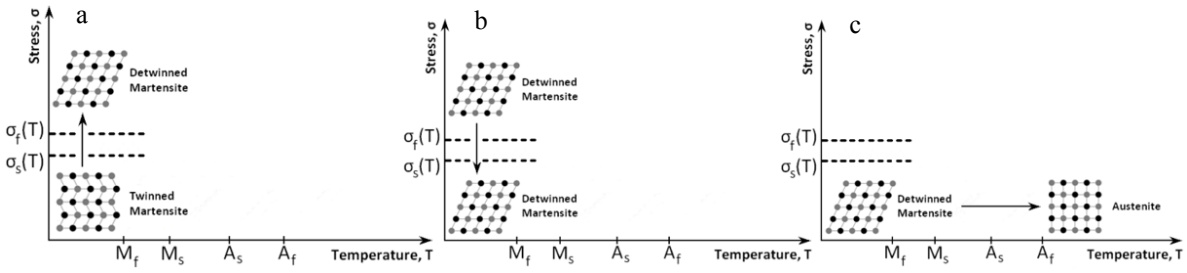

Figure 2-3 Twinned martensite is detwinned by an applied load; macroscopic deformation is observed_ martensite remains in the detwinned state when the applied load is removed; macroscopic deformation remains _ Upon heating past A_f, detwinned martensite transforms into [18]

The Superelastic effect (SE) is a stress-induced transformation for the parent phase of an SMA, austenite. An SMA in a temperature higher than A_f is fully austenite. Isothermal loading at this stage creates a macroscopic strain which is accompanied by a phase transformation to detwinned martensite. By unloading the detwinned martensite at the same temperature, the SMA immediately recovers the macroscopic deformation and transforms back to austenite (Figure 2-4).

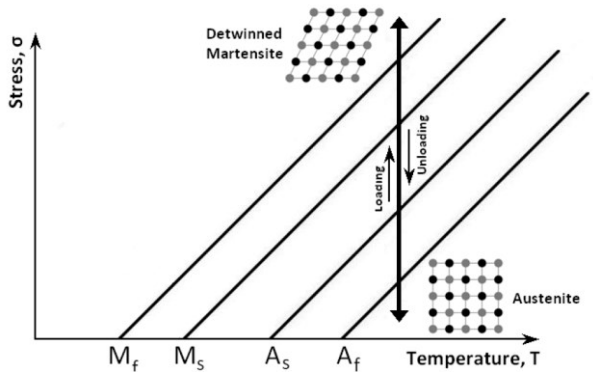

Figure 2-4 Superelastic effect: Isothermal loading above Af induces a reversible phase transformation from austenite to detwinned martensite [46]

2.2.3 Mechanical behavior of the SMAs

The mechanical response of an SMA depends on the temperature and initial phase condition. This is because of the thermoelastic and hysteretic nature of shape memory alloys. To study the mechanical response of SMAs different working temperatures can be considered as follow:

a) **For martensite with T< A_s**

When an SMA in the austenite phase is cooled down below M_f in a stress-free condition, a martensitic transformation with no macroscopic deformation happens. This transformation is achieved through self-accommodation of martensite variants. While the temperature is below A_s, the SMA in the martensitic phase remain stable. In the zero-stress stage, the SMA is consisting of many martensitic variants in twin form (twinned martensite). Loading the twinned martensite initially cause an elastic deformation in the twinned martensite. While the stress increases above a critical value, σ_s, the martensite twins transform via detwinning into a single preferred variant. The single preferred variant depends on the crystal orientation of the texture and the loading direction. The

detwinning process concludes at a critical value of stress, σ_f. During the detwinning process, between σ_s and σ_f, the stress rises slightly and creates a plateau. By unloading the material, a small amount of strain will be recovered elastically but the material remains the detwinned martensite phase. The detwinned martensite is stable at temperatures below A_s. At this stage, the residual strain and the deformed shape of the SMA can be completely recovered via reverse transformation, which is heating beyond A_f. Cooling down the austenite below M_f in a zero-stress process creates twinned martensite again.

b) **For austenite with M_s<T<A_s**

If a fully austenite SMA is cooled down in a zero-stress process to a temperature higher than M_s and below A_s, no transformation happens, and the material remains in the austenite phase. Now at this temperature region, if the SMA is isothermally loaded, first the austenite deforms plastically. By increasing the level of stress beyond a critical level, the transformation to martensite begins with a near-constant stress level, forming a plateau. The plateau is created because of the martensite phase ability to form variants during the transformation. By increasing the level of stress after the phase transformation, the martensite phase deforms elastically with its own modulus. Since the temperature is below As, the created martensite phase is thermodynamically stable and upon unloading the SMA, similar to the case (a), just a small portion of the strain will be recovered, and the material remains in the martensite phase.

c) **For austenite with A_s<T<A_f**

In this case similar to the case (b), we should start from a fully austenite phase with T>A_f. Cooling down the sample to a temperature above A_s does doe induce phase transformation and the material remains in the austenite phase. Isothermal loading of the sample at this temperature follow the same procedure as the case (b). Initially, the austenite deforms in elastic form with austenite modulus up to a critical level. Beyond this critical level, the stress-induced transformation occurs in a near-constant stress level and concludes at another critical stress level. Increasing the stress level at this stage causes elastic deformation of the martensite according to its modulus. The martensite is stable above Af due to the applied stress. By isothermal-unloading the martensite at this stage, the martensite becomes unstable and a reverse transformation to austenite occurs. The reverse transformation is occurred by the development of another stress plateau. The reverse transformation stress plateau occurs at a lower stress level in comparison with the loading transformation. Since the temperature is between A_s and A_f, the phase transformation will not be completed and in the end, there is some residual strain. Similar to the case (b), the residual strain can be recovered by heating the sample to a temperature above A_f.

d) **For austenite with T>A_f**

This final case illustrates the pure superelastic effect. Similar to the case (c) increasing the stress on an SMA with T>A_f initially creates elastic deformation. After reaching to a critical value of stress the stress-induced transformation begins and concludes at another critical stress. Additional loading causes elastic deformation of the

SMA with the martensite modulus. The only difference with the previous case is that the reverse transformation completes, and the remaining strain completely recovers elastically according to the austenite modulus. For NiTi in the superelastic mode, the recoverable strain has been reported up to %11, although in most conditions the maximum is found to be around 8%. It is worth noting that additional strains beyond the recoverable strain limit induce crystallographic slip, thus leading to unrecoverable plastic strains. Figure 2-5 shows the mechanical response of the discussed conditions.

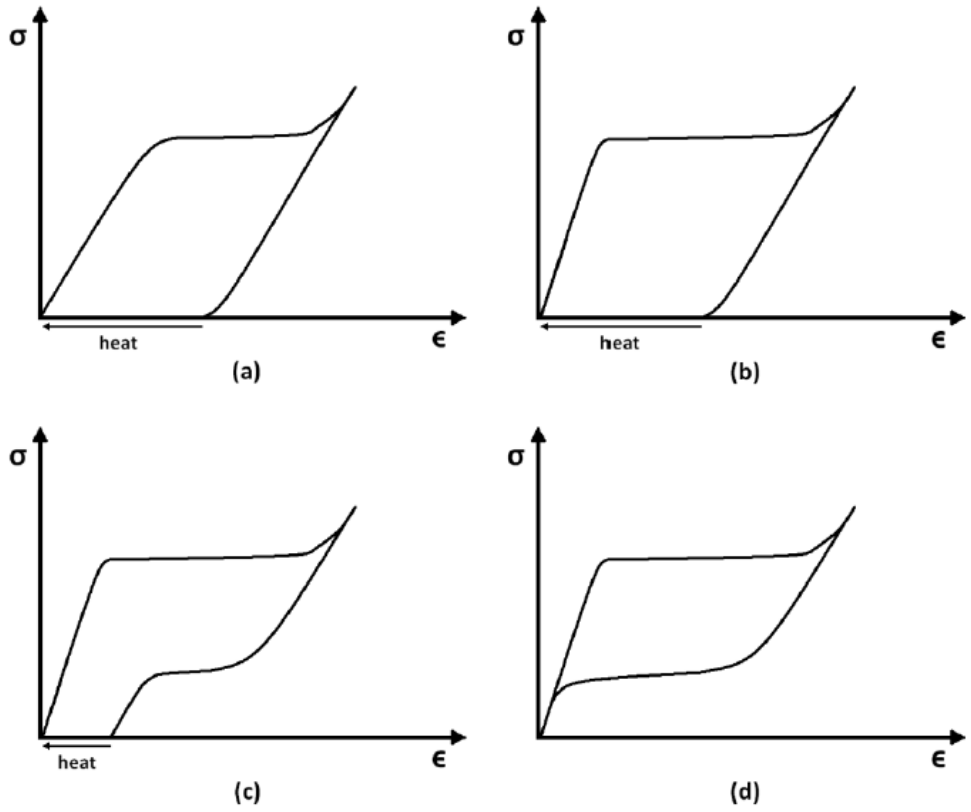

Figure 2-5 Stress-strain behavior of nitinol at different operating temperatures and initial phase. (a) martensite, T < A_s (b) austenite, M_s < T < A_s (c) austenite, A_s < T < A_f (d) austenite, T > A_f [18]

2.2.4 Physical metallurgy and composition

There are two main factors that greatly affect the phase transformation behavior of the NiTi: Elemental composition and thermomechanical treatments. Elemental composition is the basic characteristic of an SMA. The single phase NiTi only presents in near equiatomic composition Nickel-Titanium alloys. Figure 2-6 shows the phase diagram of the Nickel-Titanium Alloy. As it can be seen in the phase diagram, the NiTi region is bounded by Ti_2Ni to the left and $TiNi_3$ to the right. The TiNi region is almost vertical on the Ti-rich side right about 50-50 atomic percent. On the right side, the Nickel atomic percent can be as high as 56 % at 1115℃. This is a critical point and below this temperature, the boundary decreases as temperature decreases. Because of that Nickel does not have a fixed composition. While the alloy can dissolve up to 6 % excess Ni at high temperature, it cannot dissolve excess Ti. The solid solution at high temperatures can be preserved to room temperature without precipitation via quenching [33].

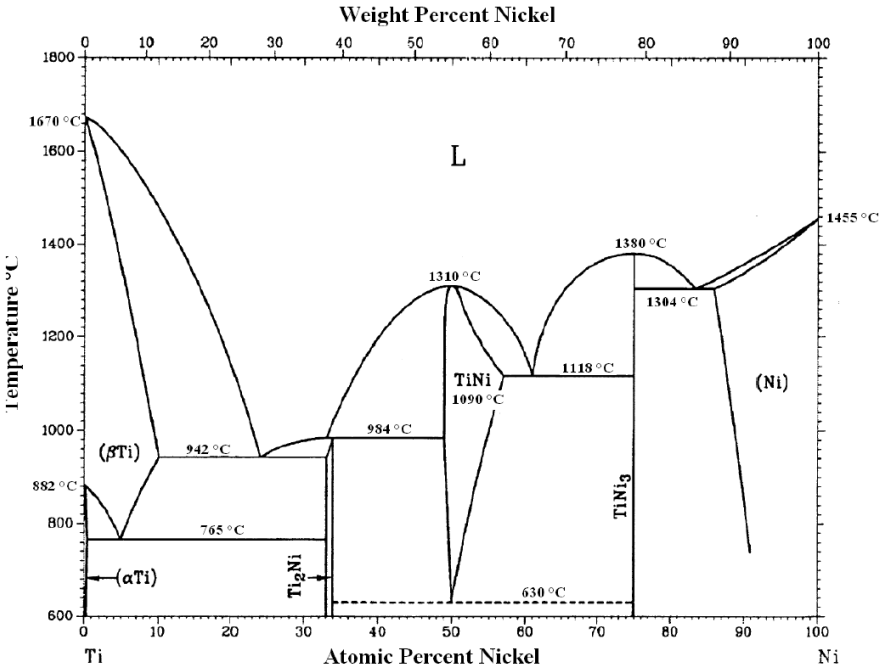

Figure 2-6 Phase diagram of a Ti-Ni alloy [51]

As shown on the phase diagram, Nitinol is typically composed of approximately 50 to 51 at. % nickel (~55 to 56% weight percent). It has been shown that Nitinol composition with more than 50.6 at.%, which is also called Ni-rich NiTi, is more sensitive to heat treatment and have superior cyclic stability compared to equiatomic NiTi SMAs [52]. The near equiatomic Nitinol has limitations such as poor cyclic stability and low strength [33]. In addition, the transformation temperatures of the equiatomic NiTi alloys are too high for biomedical applications.

Binary NiTi alloys' transformation temperatures are in the range of -40 to 100 ℃ and show a temperature hysteresis of 20-40 ℃ [52]. Small changes in the Nickel content leads to a significant change in transformation temperatures of the alloy [53]. In the quenched NiTi alloys the transformation happens in a single-step from austenite to martensite and the transformation temperature highly depends on the alloy composition. Meier *et al.* showed that changing Nickel concentration by 0.1% in Ni-rich alloys can

shift M_s by more than 10℃ [54]. Tang predicted the martensite start temperature for various compositions based on the literature [53, 55, 56]. This data has been shown in Figure 2-7 with respect to the atomic percent Nickel of the alloy [56]. On the Ti-rich side, the martensite start temperature (M_s) virtually remains constant at 60℃, while on the Ni-rich side the M_s decreases with increasing the Ni content. Based on this plot, while there are other characteristics and mechanisms that govern transformation temperatures, the nickel content should be considered to adjust the transformation temperatures of a Nitinol alloy.

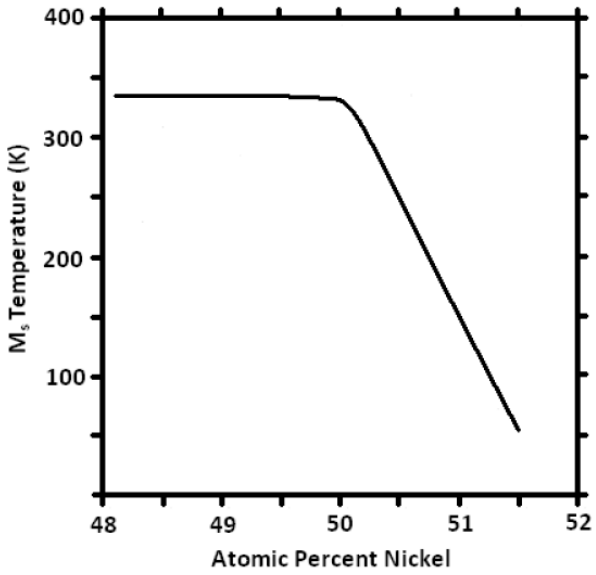

Figure 2-7 Approximate martensite start temperature (M_s) as a function of nickel content in quenched NiTi alloys (predicted by Tang [57])

In addition to the Nickel content in binary NiTi alloys, alloying also affects the transformation temperatures of the NiTi compositions. Some elements, such as Hf, Zr, Pd, Au, and Pt are shown to increase the transformation temperatures of nitinol shape memory alloys [56]. Adding the third element, such as Hf to the NiTi alloy has introduced a new category of shape memory alloys called high-temperature shape

memory alloys which benefit from a higher range of transformation temperatures (200 to 400℃) and can potentially be used in aerospace and other industrial applications [58].

For different applications including superelastic and shape memory effect of a NiTi, the transformation temperatures must be adjusted precisely based on the working temperature. As it is discussed, the transformation temperatures are highly dependent on the Nickel content of the alloy. Because of that, the composition is used as the starting point and then thermomechanical treatments are utilized to fine-tune the transformation temperatures.

2.2.5 Heat treatment

Another factor that affects the transformation temperatures of NiTi components is the introduction and manipulation of precipitates in the Nitinol matrix. One can utilize aging treatments to introduce Ni-rich precipitates into nickel-rich alloys [59]. Ti_3Ni_4 precipitates appear at lower temperatures and shorter treatment times. On the other hand, Ti_3Ni_4 precipitates absorb into the NiTi matrix and Ti_2Ni_3 precipitates appear by aging at higher temperatures and longer times. Additional aging at even higher temperatures and longer times causes the absorption of the Ti_2Ni_3 precipitates and creation of $TiNi_3$ precipitates. The $TiNi_3$ is the equilibrium phase while the other two precipitates are intermediate phases. However, it should be noted that by normal aging, only the metastable Ti_3Ni_4 precipitates are observed which are stable below 600℃. According to the literature, the Ti_3Ni_4 is stable at temperatures up to 680℃ [60]. Therefore, the transformation temperatures of NiTi matrix can be tuned by manipulation of the Ti_3Ni_4 precipitates.

Horikawa in 1989 was the first one who reported the heat treatment technique for adjusting the Ni-rich transformation temperatures [60]. He discovered that alternatively, aging Ni-rich alloy between two temperatures results in the repetitive changing of TTs. It was shown that aging at higher temperatures (~550℃) results in decreasing M_s, while subsequent aging at a lower temperature (440℃) results in elevating M_s. This procedure may be used to adjust the transformation temperatures in consecutive cycles. Horikawa also showed that aging time had no significant effect of the transformation temperatures and the transformation temperatures could be controlled by aging temperatures alone, with a negligible dependence on the number of cycles.

Zhang *et al.* [61] performed a series of experiments to further study the aging of Ni-rich alloys. They showed by an aging process, a precipitation reaction occurs and Ti_3Ni_4 precipitates form which leads to a decrease in Nickel content in the TiNi matrix. Because of the phase equilibrium between the Ti_3Ni_4 precipitates and the TiNi matrix, aging at lower temperatures results in a larger decrease of Nickel content and therefore results in increased transformation temperatures and vice versa [61].

Pelton *et al.* [61] conducted a comprehensive study on the effect of heat treatment on the transformation temperatures. They used $Ti_{50.8}Ni$ (at. %) wires and performed aging for different temperatures and durations. Figure 2-8 shows the effect of aging time on the austenite finish temperature of the samples with starting A_f of 11℃. As it can be seen, the transformation temperatures are more sensitive for higher temperatures. Also, at 550℃ first the transformation temperatures decrease and then increase. The other useful plot is shown in Figure 2-9. This figure can be used for calculating the required time and temperature for achieving the desired transformation temperatures. The plot is also

called, Time-Temperature-transformation (TTT) diagram. As it can be seen in Figure 2-9, the maximum precipitation rate is at about 400°C. Since for the shape memory and superelastic responses A_f plays a significant role, the TTT plots introduced by Pelton *et al.* can be used as a practical method for adjusting the transformation methods.

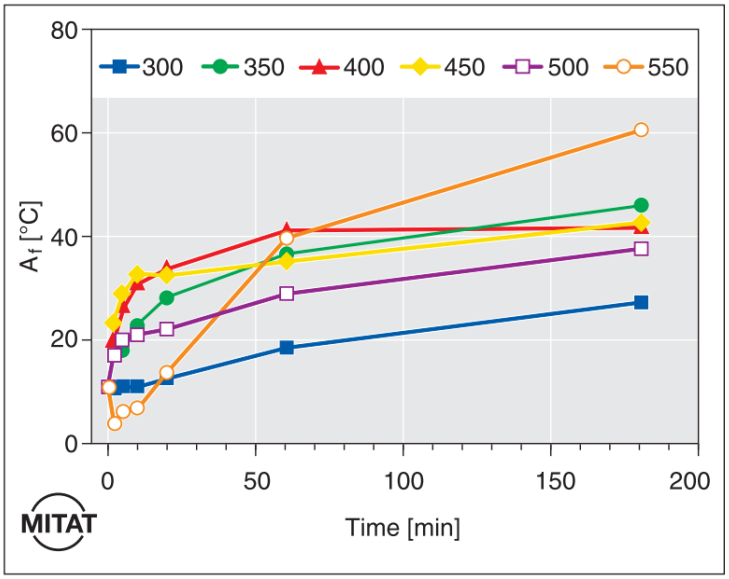

Figure 2-8 Effect of aging temperature and time on the transformation temperature of Ti50.8% Nitinol wire with a starting A_f of 11°C [60]

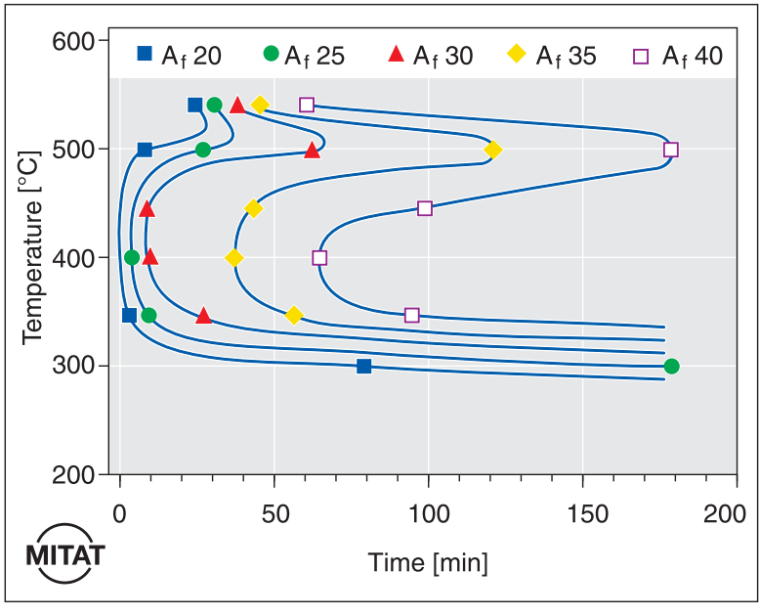

Figure 2-9 Effect of aging temperature and time on the transformation temperature of Ti 50.8 % Nitinol wire with starting A_f of 11°C.This plot is also known as the time-temperature-transformation (TTT) diagram. [62]

Ni-rich NiTi alloys inherently have a higher strength and as it is mentioned before are more sensitive to aging [63]. On the other hand, NiTi alloys with extremely low Ni content, such as Ti-50Ni and Ti-50.5Ni (at. %) do not show superelasticity in the solutionized conditions due to low strength [63]. The effect of Ni content in the superelastic response of NiTi wires annealed at 400°C and tested at 37°C under tensile has been shown in Figure 2-10. As it can be seen in the figure, the critical stress required for martensitic transformation and strain recovery are both increasing with increasing Ni content of the alloy [63]. In addition, increasing the Ni content also decreases the transformation temperatures and therefore causes the material to exhibit superelastic response at the testing temperature.

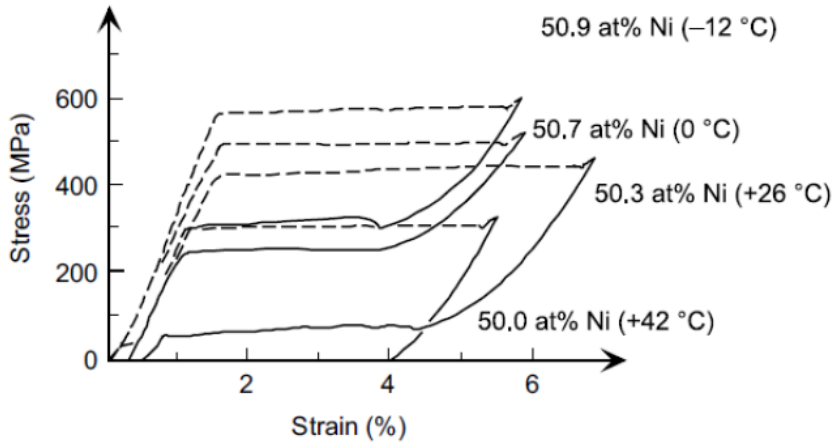

Figure 2-10 The effect of Nickel content on the transformation temperatures and the superelastic response of NiTi wires [64]

2.2.6 Biocompatibility of NiTi

The biocompatibility of a material evaluates its compatibility with the human body. In general, for an internal implant, there are two factors to be considered for the biocompatibility; the induced reaction of the host or adjacent tissue in existence of the implant, and the degradation and corrosion of any particle in the body environment [65]. Among different materials, Titanium is one of the highly biocompatible materials and has been used in orthopedic implants since the 1950's. In this material a thin TiO_2 layer forms on the surface and creates an excellent corrosion resistance [66]. For the Nitinol the same TiO_2 protective layer forms on the surface. However, the major concern is about the Nickel ion release which could be toxic for the human body [67].

Nickel is considered as a toxic element for the human body and dissolution of Ni ions could cause allergic, toxic, and carcinogenic effect [68-70]. However human tissue contains approximately 5 ppm Nickel and this level of Ni is essential for the biological function of the human body. It has been shown that 5% of the general population show allergic reactions to nickel [71]. In an animal study, pure nickel was implanted on a rabbit

bone and severe local tissue irritation, necrosis, and toxic reaction were observed [72]. Due to the high nickel content in nitinol composition, nickel ions could dissolve out of the not-processed NiTi. However, MP35N is a well-known biocompatible material used in orthodontics, orthopedics, and cardiovascular applications that contain high nickel content (35% Ni) [73, 74]. In addition, atomic bonding forces between Ni and Ti in equiatomic nitinol are significantly higher than in Ti alloys with a small amount of Ni [75] and will not produce the same reactions as pure Nickel.

In practice, the corrosion resistance of nitinol controls the *in vivo* nickel ion release. Corrosion resistance in most of the metallic alloys is a result of passivation, which is the formation of a protective oxide coating layer in contact with oxygen. Regarding NiTi, controlled processing consideration and heat treatment are required to maintain the desired mechanical properties, and proper passivation is needed to achieve a high level of corrosion resistivity and biocompatibility. The ASTM F86 [76] standard recommends a chemical treatment of metallic implants to ensure proper passive surface condition. For stainless steel, the recommended surface treatment involves a nitric acid passivation or electropolishing to modify the surface oxide characteristics and improve the biocompatibility. NiTi is also a passive alloy similar to titanium and stainless steel, and a stable oxide layer protects the base material. This oxide layer can be further enhanced by modifying the thickness, topography and chemical composition by selective treatments [77, 78].

It has been shown after controlled passivation, a 3-4 nm thick TiO_2 film forms on the NiTi surface [76]. Although TiO_2 is the main element of the coated layer, a small amount of Nickel oxides (NiO and Ni_2O_3) and metallic Ni are also observed. An *in vitro*

study showed that in the case of proper passivation only metallic Ni was observed on the surface [77]. In this study, samples were etched in a Hf-HNO_3-H_2O (1:2:3 vol. %, 30 mins) solution, pre-deformed, ultrasonically cleaned in ethanol and sterilized by X-ray at room temperature for passivation. No major changes were observed in the composition after 4 and 12 months.

In 1973, Cutright [79] reported the first study on the biocompatibility of NiTi. In this study wire sutures of NiTi ($Ni_{55}Ti$, also called 55-Nitinol) were implanted subcutaneously in 45 rats. The tissue reaction was monitored for 9 weeks. After 6 weeks, dense, relatively vascular fibrous tissues were formed around the NiTi wires and a minimal tissue reaction for the entire period was reported. Based on this study the biocompatibility of 55-NiTi was reported similar to stainless steel and deep tissue implantation was possible.

In 1976, femoral bone plates made of pure nitinol were implanted in dogs and were removed and examined after 3, 6, 12, and 17 months [80]. No evidence of localized or generalized corrosion on the implants was observed on any of the plates. In addition, gross clinical, radiological, and morphological observations of the adjacent tissue were evaluated and showed no adverse tissue reaction. The NiTi response was compared with cobalt-chromium skeletal fixation plates and no significant difference was reported.

In a study in 1996, the biocompatibility of NiTi screws was compared with Vitallium, titanium, duplex austenitic-ferritic stainless steel (SAF), and 316L stainless steel [81]. The screws were implanted in a rabbit tibia and studied after 3, 6, and 12 weeks after implantation. The biocompatibility of NiTi screws was in the same range as traditional materials. However, diminished activity of bone cells and osteonectin

synthesis in accordance with slower bone-remodeling around the nitinol screws were reported.

In 1997, Takeshita *et al.* used cylindrical nitinol implants in the medullary canal of rat tibiae to study the bone reaction using a histomorphometric analysis [82]. The authors compared the biocompatibility of NiTi with identical implants made of titanium, anodic oxidized Ti (AO-Ti), Ti-6Al-4V, and nickel. The NiTi, Ti, AO-Ti and Ti-6Al-4V implants were integrated with connective tissues over 168 days. Based on histometric analysis no significant difference in tissue reaction was observed in case of using Ti, AO-Ti, and Ti-6Al-4V implants. NiTi implants exhibited a lower percentage bone contact and bone contact area than other Ti-based alloys. However, Ni implants showed no bone contact at any time during the experiment.

In 1999, Ryhanen *et al.* studied the osteotomy healing, bone mineralization, and the remodeling in presence of NiTi [83]. Intramedullary nails made of NiTi and stainless steel were used to fix femoral osteotomies in rats (n=40). Radiographs, peripheral quantitative computed tomography (pQCT), and histology were used to analyze the bone healing, and electron microscopy (FESEM) was used for evaluation of the corrosion of the implants. After 2, 4, 8, 12, 26, and 60 weeks, the bones and implants were analyzed. In the early stages (4 and 8 weeks) NiTi group had more healed bone unions than stainless steel group. At the later stages, no significant difference in bone healing between the two groups was observed. Both NiTi and stainless steel group reached full healed none unions by the week 60. It was observed that NiTi does not impair the osteotomy healing response, consolidation, mineralization, or remodeling of bone compared to stainless steel. In addition, Nickel ion release of the implants was negligible.

Ryhanen *et al.* also evaluated new bone formation, modeling and cell-material interface responses induced by NiTi periosteal implants [84]. In this study, the femoral periosteum was in contact with NiTi, Ti-6Al-4V, and stainless steel implants. Histomorphometry with digital image analysis was used for evaluation of the bone formation. At 12, and 26 weeks no statistical difference between bone formation for NiTi and other implants was observed. The soft tissue around the NiTi implant did not show any toxic or irritating response based on the histomorphometry analysis. It was concluded that NiTi exhibits similar effects as other biocompatible materials on the new bone formation.

In 2000, Kapanen *et al.* studied the effect of NiTi, Stainless steel, and Ti-6Al-4V implants on bone formation under the fascia of the latissimus dorsi muscle in rats [85]. The bone mineral density values were measured for different implants after 8 weeks. It was reported that NiTi group had nearly equal bone mineral density compared with healthy subjects. However, the stainless steel and Ti-6Al-4V group showed lower bone mineral density. In addition, the largest proportional cartilage and new bone area were observed for the NiTi group.

2.2.7 Biocompatibility of Porous Nitinol

Although the biocompatibility of bulk and dense NiTi implants have been well established, for porous NiTi because of the increased surface area and different methods of fabrication different biological responses may be observed. The cytotoxicity of porous NiTi has been evaluated since 1995 in several articles [83-94].

In 1995, Simske and Sachdeva evaluated uncoated porous NiTi craniofacial implants in a rabbit study [88]. The subjects were analyzed 2, 6, and 12 weeks after

implantation for tissue reaction and bone formation. After 2 weeks, the soft and connective tissues were successfully attached to the implant and no sign of tissue inflammation was reported. The new bone formed on the implant was examined using microhardness and histologic assessments and showed similar properties to the surrounding bone. Rhalmi *et al.* [88] in a similar study in 1999 reported similar results in tibial osteotomies. Rhalmi *et al.* reported an integrated connection between the bone and the implant with no adverse effect on the surrounding tissues.

In 2003, Assad *et al.* studied the surface corrosion and nickel-ion release of porous NiTi implants [4]. In this study porous NiTi interbody fusion devices (Actipore by Biorthex, Inc.) were compared with Ti-6Al-4V samples. The two types of samples were implanted in a sheep model and evaluated after 3, 6, and 12 months. No evidence of surface corrosion in any of the specimens was observed after scanning electron microscopy (SEM). The blood Nickel level was within the acceptable range during the experiment. The nickel content in adjacent tissues to the implants was tracked and no difference was reported. Furthermore, using histomorphometric and radiological analysis, authors reported a better radiological fusion for NiTi implants [90]. Based on this study porous NiTi could be a great candidate as a substrate for osteogenic integration and represents a new osteoconductive biomaterial with better fusion characteristics than conventional Ti-6Al-4V.

A desired bone implant not only must provide sufficient bone contact and ingrowth, but also must minimize allergic, toxic, and carcinogenic effects. Likibi *et al.* [4] evaluated the osseointegration of porous NiTi implant using a 12-month study on intervertebral lumbar implants in sheep. Titanium and NiTi implants were used in this

study. Based on the radiological analysis, 15 out of 16 (93.75%) porous NiTi implants demonstrated bone integration, while only 4 out of 16 (25%) Titanium implants performed well.

In 2003, Kujala *et al.* studied the effect of porosity on the osseointegration of nitinol implants in a rat study [4]. In this study authors compared implants with different levels of porosity. Based on this work, the implant with 66.1% porosity and mean pore size of 30 microns showed the best bone contact compared to the two other implants with 59.2%, and 46.6% porosity and pore size of 272 and 505 microns, respectively.

2.3 Fabrication of NiTi

2.3.1 Melting and casting

There are several well-established methods of fabrication for NiTi. Among different recipes, Vacuum Arc Melting (VAM) or Vacuum Induction Melting (VIM) followed by hot working, cold working, and machining are considered as the conventional methods of fabrication. Since NiTi is highly activated in contact with oxygen, and to minimize the possibility of contamination during melting, an inert gas, usually Argon, is used [4]. In addition, due to the high reactivity of Titanium, high-temperature processing such as melting, and alloying is accompanied by the formation of Ti-rich phases and higher impurity levels. Pure elemental Ni pellets and Ti rods in a graphite crucible are used for the VIM process and Figure 2-11 illustrates this procedure [4, 95]. The VIM process uses an induction coil heated graphite crucible which contaminates the melt with carbon. However, the fabricated ingots have good homogeneity since mixing is assisted by eddy currents [4]. Vacuum arc remelting (VAR) technology uses a DC current to melt compacted Ni and Ti electrodes into a water-cooled

copper crucible. The contamination is much lower than VIM method since the melted region is never in direct contact with the crucible [4].

In addition to conventional casting processes, electron beam melting (EBM) can be used for fabrication of NiTi alloys. In EBM, melting occurs in a water-cooled copper crucible and it is under a high vacuum (pressure below 0.01 Pa) which minimized carbon and oxygen contamination [4].

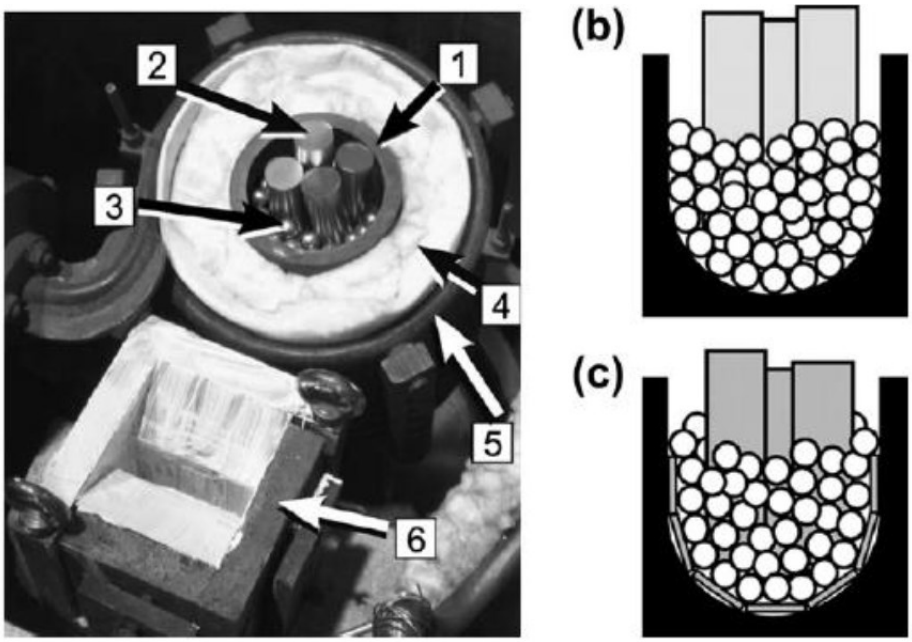

Figure 2-11 (a) a setup for VIM processing of binary NiTi (1: graphite crucible; 2: Ti rods; 3: Ni pellets; 4: isolation; 5: water-cooled copper coil; 6: mold); (b) & (C) schematic illustration of the crucible filling with Ni pellets in contact with the graphite [4, 96, 97]

2.3.2 Machining

The ingots fabricated by melting and casting methods can be used for fabrication of parts with desired and more complex geometries. The machining can be done by conventional and also by advanced machining methods. Lin *et al.* [98], Weintert and Petzold [4], and Wu *et al.* [96] have worked on conventional machining characteristics of

SMAs, especially NiTi. In summary, machining of NiTi is very challenging [99] due to special properties of SMAs. The challenging machining is due to the presence of intermetallic compounds, strain hardening effect, cyclic hardening and fragments of alloy adhered on the surface of the tool. In addition, the time required for machining, depressing in cutting ability, higher tool wear, hardening of the machined surface, and poor surface finish are the other factors that limit the conventional machining of SMAs. Due to these limitations, the non-conventional machining has been adopted for manufacturing economic functional parts made of NiTi. Although these non-conventional methods still have some limitations, they have been used in the fabrication of commercialized NiTi implants in the market and should be covered.

2.3.3 Non-Conventional machining:

Several non-conventional machining techniques, such as laser machining, water jet machining (WJM), electric discharge machining (EDM), electrochemical machining (ECM), wire-EDM (WEDM), and hybrid machining have been used for fabrication of NiTi. In this section, a summary of these methods is discussed. However, special machining methods have their own limitations [100-102].

Laser machining, EDM, and Wire EDM have been widely used for machining of NiTi parts. Laser machining is preferred for less thermally and electrically conductive materials. Due to the surface alteration and formation of residuals, the laser treated surface must undergo further removal process [103]. Electrically conductive materials, regardless of the hardness, can be machined effectively via EDM [104]. Wire EDM (WEDM) has the ability to machine precisely 3D irregular structures. WEDM provides parts with lower residual stresses and better surface finish [105]. Based on the literature,

EDMed and WEDMed NiTi based alloys with thickness of up to 0.6 mm exhibit perfect shape recovery at 3% strain and 5% bending strain [106].

2.3.4 Powder metallurgy (PM): Conventional

Powder metallurgy (PM) methods have been used for fabrication of dense and porous NiTi from elemental and pre-alloyed powders. The main advantage of powder metallurgy methods is the capability of fabricating near net shape components and the possibility of fabricating porous structures [107]. Different conventional PM methods, such as conventional sintering (CS) [108], spark plasma sintering (SPS) [96], self-propagating high-temperature synthesis (SHS) [109, 110], sintering at elevated pressure via a hot isostatic pressing (HIP) [111], and metal injection molding (MIM) [112] have been used for fabrication of NiTi parts. Each of these conventional methods has their own advantages and disadvantages. In general, due to several reasons, such as the large specific surface area of the powder, and high-temperature processes (e.g. for powder preparation and the main PM procedure), final NiTi components produced by PM contain higher levels of impurities and contamination in comparison with the conventional methods and may have degraded functional structural properties [106, 113]. The pre-alloyed powder has been shown to have a better outcome in comparison with the elemental powder, due to the formation of secondary phases and non-homogeneous composition in case of using elemental powders [114].

Conventional sintering (CS) has relatively low cost, and provides good dimensional precision, high production rate and eliminates the need for secondary machining [108, 115]. On the other hand, the CSed parts contain a large amount of pores up to 40%, and there is no good control over the pore size and amounts [96]. Advantages

of the SHS method are the low level of energy, and the relative simplicity of the process and equipment [107, 115]. On the other hand, the fabricated parts using SHS method, contain large size and amount of porosities and does not exhibit perfect functional properties due to the short forming time, high heating rates, and formation of secondary phases [116]. The SPS method provides high energy efficiency and requires low sintering temperature and short processing time and can be used for fabrication of different materials (e.g. metals, ceramics, composites, etc.) [117]. The downside is that expensive pulsed DC generator is required for SPS and only simple geometries can be fabricated.

Sintering at elevated pressure via a hot isostatic pressing (HIP) enables fabrication of dense parts with almost no pores and good mechanical properties. There is a good control of pore size and the procedure requires low sintering temperatures [114]. Based on the literature, the inert gas may cause porosities for up to 40% and the creation of secondary phases is possible [114]. HIP requires costly equipment and does not allow high production rate [117]. Metal injection molding (MIM) allows fabrication of more complex geometries with higher production rate [114]. The material properties are close to the wrought material and there is good dimensional tolerance control using MIM. On the other hand, fabricated parts via MIM have limitations in size, may have residual pores, and the process requires high sintering temperature and costly tooling [65, 110, 118].

The powder preparation has a significant effect on the final part fabricated by PM. The particle size, shape, distribution, composition and impurities, and flowability must be carefully monitored for fabrication of the desired parts [113]. Among different techniques for preparing the powder, such as mechanical attrition or ball milling, atomization in

water or gas, hydrating and creating powder by laser ablation, the gas atomization methods have shown the most promising results [119].

Most PM methods do not allow fabrication of parts with engineered porosity (i.e porosity with a controlled amount, pore size, and pore shape) and do not provide a good control over impurity content, and homogeneity. In addition, the formation of secondary phases in the case of using elemental powder is unavoidable, since their formation is more favorable thermodynamically compared to the formation of NiTi [120]. Undesirable secondary phases eliminate the mechanical properties and make the porous structure brittle and change the transformation temperatures.

2.3.5 Additive manufacturing

Additive manufacturing (AM) is one of the most recent powder metallurgy methods with tremendous advantages over both conventional and other powder metallurgy techniques [121, 122]. Additive manufacturing (AM) is a relatively new method of fabrication that provides a solution for manufacturing complex nitinol components using elemental or pre-alloyed powder. In earlier literature, AM is also known by layer manufacturing, solid freeform fabrication, rapid prototyping, and 3D printing as well. However, in 2009 the ASTM committee F42 on additive layer technologies introduced and standardized the Additive manufacturing (AM) term for all layer-by-layer methods of fabrication [123].

All AM techniques enable fabrication of components directly from the 3D Computer Aided Design (CAD) files. As a general step, the CAD file is first sliced into thin layers (20 to 150 micron) and the fabrication starts by creating each layer sequentially in the z-direction on top of the previous layer [124-126]. Parts with complex

geometries, such as engineered porosities, scaffolds, hollow parts, filigree structures, and other geometries that are not possible to fabricate through traditional techniques, can be fabricated via AM techniques. In addition, fabrication directly from the CAD file reduces the timescale from concept to prototype and facilitates fabrication of reliable custom-designed components [125].

According to ASTM, AM methods can generally be categorized as material extrusion, material jetting, vat photopolymerization, sheet lamination, binder jetting, Direct Energy Deposition (DED), and Powder Bed Fusion (PBF) [119]. For AM of metallic parts, Direct Energy Deposition (DED) and Powder Bed Fusion (PBF), that both use powder as the base material, have shown the most promising results [127]. In DED, the powder is blown and *in situ* laser melts the powder. In PBF, the powder is spread on a platform (bed) and a laser or electron beam, as a thermal source, induces fusion between metal powder particles. DED has been implemented in different commercialized technologies, such as Laser Engineered Net Shaping (LENS), Direct Light Fabrication (DLF), Laser Consolidation (LC), Laser Cladding, and Shape Deposition Manufacturing (SDM) [128].

Powder Bed Fusion (PBF) techniques include selective laser sintering (SLS), direct metal sintering (DMLS), selective laser melting (SLM), and LaserCUSING [129]. Electron beam melting (EBM) is also another AM technology that uses electron beam as the energy source but has not been used for fabrication of NiTi parts [118]. For all PBF methods, similar to other AM methods, the desired CAD part, which includes the main file and the required supports is sliced into layers with predefined thickness. All the sliced layers in addition to the required processing parameters are transferred to the PBF

machine. At the beginning of the fabrication, the PBF machine spread a layer of powder on the build's plate. The process usually happens by a knife or roller. The thickness of this layer of powder is the same as the slices of the CAD file. Then an energy source, which can be a laser or an electron beam, selectively melts or sinter the powder particles based on the geometrical information of the first layer. At this stage, the built substrate moves down as the thickness of a single layer and another layer of powder is spread on the build substrate. The energy source selectively melts or solidify this new layer and this procedure continues to the point that all layers are fabricated on top of each other and the final part is fabricated. Finally, the fabricated part that is surrounded by loose powder must be removed from the substrate. A schematic of this procedure is shown in Figure 2-12.

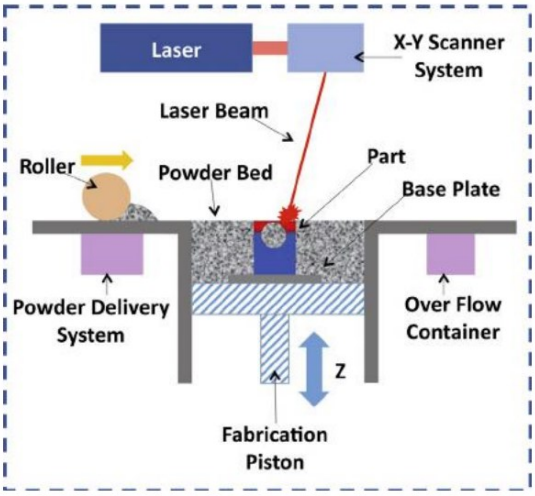

Figure 2-12 a Schematic of the powder bed fusion process

2.4 SLM of NiTi

Among different PBF technologies, we have used laser-based PBF or selective laser melting for fabrication of NiTi parts. There are several parameters that define the SLM procedure. Starting from the powder, it can be either elemental or pre-alloyed with

different particle sizes. Based on the selected powder particle size and the resolution of the machine, the layer thickness of the fabrication can be calculated. The laser power, scanning speed, and scanning strategy are the other main parameters of the build. The physical condition of the built chamber such as temperature, oxygen level, vacuum condition or existence of an inert gas are the other important parameters for the SLM method [130].

2.4.1 Powder

The first step in SLM method is to prepare the powder. Since NiTi powder is not commercially available, the process starts with powder preparation from NiTi ingots. Particle size, shape, flowability, packing density, and impurity are the main parameters of any powder for PBF [131]. The powder particles must be as small as possible that can be deposited in thin layers. The powder fraction has to have a multimodal particle size distribution for increasing the packing density. High packing density leads to the production of parts with higher density compared to loose powder [132]. Gas atomization technique is a well-known method for preparing powder from the ingots. This method allows for fabrication of spherical powder particles that increases the powder flowability compared to other shapes. Although small powder particles increase the packing density, very fine powder particles decrease the flowability due to higher surface to volume fraction. It has been shown for NiTi, powder particles smaller than 20-63 μm have insufficient flowability and only 56% packing density, while powder particles in range of 25-75 μm and 45-100 μm have packing density of about 60% and good flowability [133]. Another challenge in preparing NiTi powder is to prevent impurity pickup (e.g. oxides and carbides) during the atomization process. Electrode Inert Melting Gas Atomization

(EIGA) has been shown to be the most efficient method to avoid impurity pickup [129]. However, even for this method, high levels of oxygen pickup has been reported in some references [134]. The amount of impurity pickup is also a function of the powder particle size, and fine particles absorb a higher level of impurities due to the higher exposed surface area. Haberland *et al.* [135] in a comprehensive work studied different parameters, such as size, shape, flowability, packing density, impurity contents, transformation ability and mass fraction of NiTi powder for SLM process. Based on their work, summarized in Figure 2-13, powder particles with medium-sized fractions of 25-75 μm provide the best properties for SLM of NiTi.

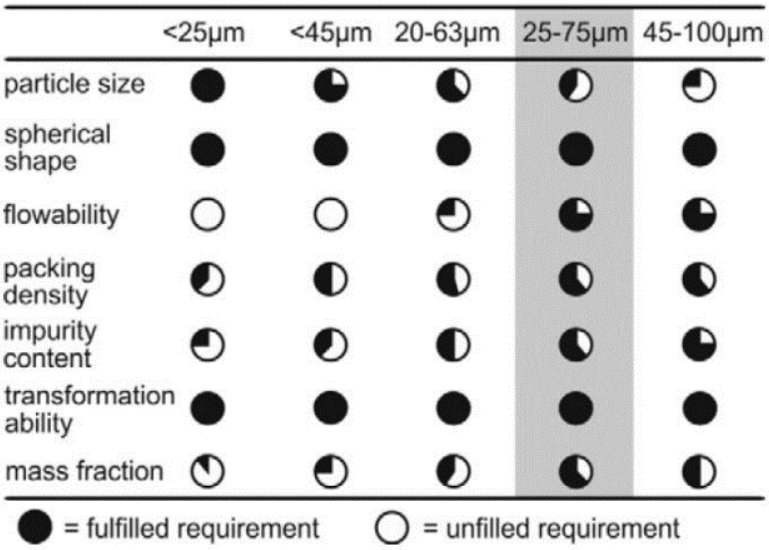

Figure 2-13 Qualitative classification of different powder fractions for their suitability for AM

2.4.2 Process parameters

In the early 2000's, Powder Bed Fusion (PBF) technology was used for the first time for fabrication of NiTi in the form of Selective Laser Melting (SLM) [136, 137]. The first studies were focused on the feasibility of the fabrication process of NiTi via SLM. Shishkovsky *et al.* [52, 138], studied the microstructure and shape memory effect

of SLM fabricated NiTi. Clare *et al.* [139], studied the shape memory effect in SLM fabricated NiTi cantilever beams for potential MEMS applications. Meier *et al.* [129, 140, 141] studied the functional properties and cyclic response of additively manufactured NiTi and compared them with that of conventionally fabricated. From 2012 to 2014, Haberland *et al.* [142-144] worked on the superelasticity and cyclic stability of the SLM NiTi samples. The effect of processing parameters in SLM of NiTi on the phase transformation response, transformation temperatures, and microstructure properties was later studied in more details. Dadbakhsh *et al.* studied the effect of process parameters on the transformation temperature, and mechanical response of the SLM fabricated dense and porous NiTi samples [145, 146]. Based on their work, the process parameters greatly influence the transformation temperatures and mechanical response of the fabricated NiTi parts. Microstructure and texture of the SLM NiTi were studied in more details by Bormann *et al.* with considering different processing parameters, such as different scanning strategies [147-149]. Speirs *et al.* [129] studied the effect of SLM process parameters on the geometrical characteristics of porous NiTi samples. Finally, Habijan *et al.* [142] studied the biocompatibility of the SLM fabricated NiTi.

In general, in addition to the powder selection, each of the process parameters including scanning speed, scanning strategy, laser power, and even the dimensional ratios affect the mechanical, structural and functional response of the SLM fabricated NiTi parts. A common relation between some of these variables has been defined by several groups as the “energy input”. Energy input is a function of laser power, scanning speed, hatching space, and the layer thickness, and is defined based on the equation (1). It has been shown that higher energy inputs lead to higher strength in the fabricated NiTi parts.

However, the impurity of the fabricated parts with high energy inputs increases as well [129, 142, 144].

$$E = \frac{P}{v.h.t} \quad (1)$$

Although different groups reported relatively different process parameters for a successful fabrication, it can be concluded that at least 100-200 J/mm^3 energy input is required for fabrication of the dense SLM NiTi [41, 150, 151]. In addition, recently computer models and machine learning methods have been used for optimizing the process parameters in AM methods [152].

2.5 NiTi and medical device applications history

NiTi properties and performance directly depends on the working temperature. Human body offers an isothermal environment and because of that NiTi performance and properties can be well designed. In the beginning, NiTi was considered as a potential material for biomedical applications. However, in 1970's and 1980's NiTi performance and properties (e.g. Fatigue life, hysteresis, nonlinear tensile/compression properties, and heating and cooling effect) were not well understood and there were many obstacles in production, and proper treatment that prevents the development of NiTi applications [41]. As a result, most of the large medical device companies lost interest in NiTi and worked on other conventional biomaterials. On the other side, the researched continued in the scientific community until the early 1990's that NiTi returns to the medical device industry [153]. In the 1990's there was a large demand on less and minimally invasive procedures in the medical industry and novel manufacturing techniques including laser cutting and micro tubing were available. All these circumstances led to the first

commercially successful nitinol medical device which was a self-expanding stent [154]. At the same time, several other major biomedical companies started focusing on NiTi applications.

The first medical devices made of NiTi in the market were self-expanding catheter-deployed devices that benefited from the superelastic property of NiTi. The large level of recoverable strain was used for applications where the use of conventional materials was not possible. One of these commercial products was the Homer Mammalok needle localizer [155, 156]. This device was equipped with a superelastic hook which could be withdrawn into a straight shape using a catheter and also recovered its hook shape after deployment. Following by superelastic medical devices, NiTi devices with shape memory properties were also introduced to the market. One such device was the Simon vena filter [157, 158]. This device is inserted to the vena cava using a catheter in a straight configuration. After placing this device at the right position, its shape starts to transform due to the shape memory effect, activated by the body temperature. The Simon filter in its transformed shape act as a filter to catch embolized blood clots. Following by these two categories of NiTi medical applications, NiTi devices have been widely used in the orthodontic [159-162] and vascular fields [163-166]. More recently NiTi has been introduced to the orthopedic fields and different applications have been invented based on the superelasticity, shape memory as well as other mechanical properties.

2.6 Nitinol in orthopedic applications

Devices for fracture fixation, including skeletal fixation plates and staples are amongst the very first applications of NiTi in medicine. One of the very first patented applications of NiTi in 1974 is for a skeletal fixation plate [167]. Following by that, NiTi

bone staples were then first commercialized to the Chinese market in 1981, to the European market in 1990, and to the U.S. market in the mid-1990 [167]. NiTi compression staples have been used for fracture treatment in different regions, especially small bones, such as toes, fingers, hand, and ankle. The advantages of bone staples include good approximation of the bone fragments, dynamic compression of the fracture surfaces, avoidance of infection issues associated with external fixations, and reduced operating time as compared to bone screws [168]. Application of NiTi bone staples usually starts with A) temporarily fixating the two pieces of bone to maintain proper alignment, B) Pre-drilling the holes to accept the bone staple, C) Inserting and seating the staple, and D) Triggering recovery of the staple's preprogrammed shape either by removal of a constraint or by application of heat [169].

To apply a typical NiTi staple, first the holes are pre-drilled and then an "open" NiTi staple is inserted into the holes. After insertion, the staple recovers either superelastically or via shape memory activation to pull the fractured bones together or apply a compressive force to the fractured surfaces. Different NiTi staple providers have implemented this approach in different ways.

2.6.1 Room temperature superelastic (SE) NiTi staples

In this type of NiTi staple, the austenite finish temperature (A_f) is slightly below room temperature and the staples must be held open by some type of device prior to deployment. This type of NiTi staples attempts to recover its shape to the "closed" form at any temperature above room temperature as soon as the constraint is removed.

2.6.2 Body temperature activated (BT) NiTi staples

This type of NiTi staple has an austenite finish temperature slightly below body temperature and above room temperature. This type of NiTi staple recovers its shape via thermal shape memory effect as the staple reaches body temperature. It is important to maintain the staple's temperature below body temperature during insertion to prevent shape recovery. This can be achieved via a combination of external cooling and sufficiently rapid insertion.

2.6.3 Controlled heat activated (HA) NiTi staples

This type of NiTi staple has an austenite start temperature slightly above body temperature, but an austenite finish temperature low enough to allow deployment without the application of excessive heat. Approximately 60℃ is recognized as the temperature at which tissue damage occurs. The activation temperature, therefore, must be kept below this temperature. This type of staple is usually activated by using a heating element such as a cautery element. Figure 2-14 shows some of the designs of the available NiTi staples, and Table 2.1 summarized some of the providers, mechanisms, and applications of NiTi staples.

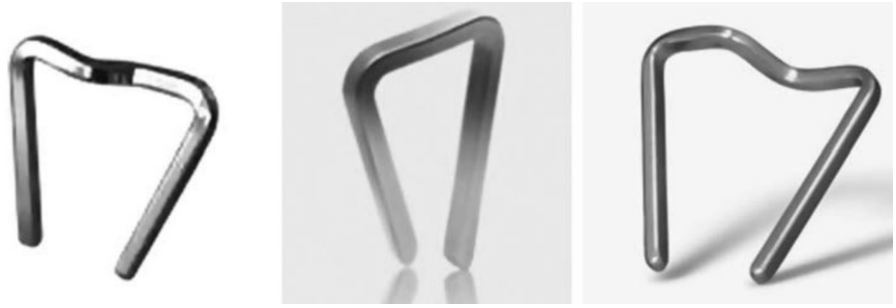

Figure 2-14 Examples of commercially available Nitinol bone staples

Table 2.1 Examples of commercially available Nitinol bone staples (BT: body temperature)

Trade name	Company	Deployment	Indications
Memory Staple	Depuy Synthes	BT activated	Foot, ankle
Memory Staple™	Intellifuse	Heat activated (Intellifuser)	Head and face, soft tissue, hand and foot, bone fragments, lower limbs
Memoclip®	Memometal	Heat activated	Hand and foot
EasyClip®	Memometal	Heat activated	Hand and foot
MEMODYN™	Telos Medical/ BioResearch Innovations	Heat activated	Foot, ankle, hand, wrist
OSStaple™, BOSS™, OSSArc™, OSSpine™, OSSAnchor Grip	BioMedical Enterprises	Controlled heat activated (OSSforce)	Head, face, sternum, pelvis, cervical spine, hand, and foot, upper and lower extremities
BioPro® Memory Staple	BioPro	BT activated	Foot, ankle, hand, wrist
JAWS™	Paragon 28	Superelastic (SE)	Small bone fragments of foot
EasyClip	Stryker	Superelastic (SE)	Small bone fragments of foot and hand
SpeedTitan, SpeedArc, SpeedTriad, SpeedShift	DePuy Synthes and Biomedical Engineering	Superelastic (SE)	Small bone fragments of foot and hand

2.6.4 Modified NiTi staples

Several other applications inspired by NiTi staples have been introduced to the market. As such devices, Stryker introduced 4Fusion (Figure 2-15.a) for hand and foot bone fragments osteotomy fixation and joint arthrodesis. EasyStep is another superelastic NiTi implant that offers step heights to allow various step depths and provide compression between the barbed legs. Easy step does not require heat activation to provide compression between barbed legs and is shown in Figure 2-15.b.

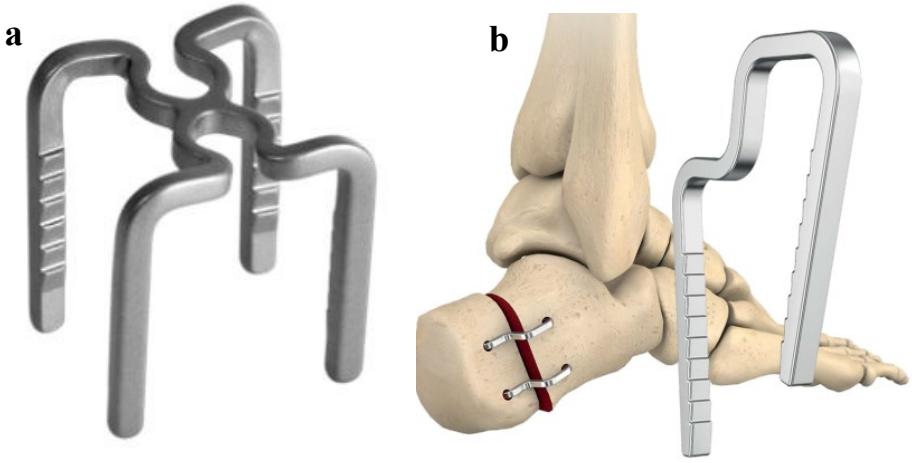

Figure 2-15 (a) 4Fusion by Stryker, (b) EasyStep staples by Stryker

DePuy Synthes provides two other modifications of NiTi staples which are both used for fracture and osteotomy fixation and joint arthrodesis of the hand and foot. SpeedTriad which is shown in Figure 2-16.a is a superelastic compression implant with three legs for stable six-point fixation specifically designed for distal first metatarsal osteotomy. BME Elite is a plate-like low-profile implant design with four legs that are available in multiple sizes. In addition to the constant compression load, the four-leg design enables the device to provide high rigidity and torsional stability compared to titanium skeletal fixation plates (Figure 2-16.c).

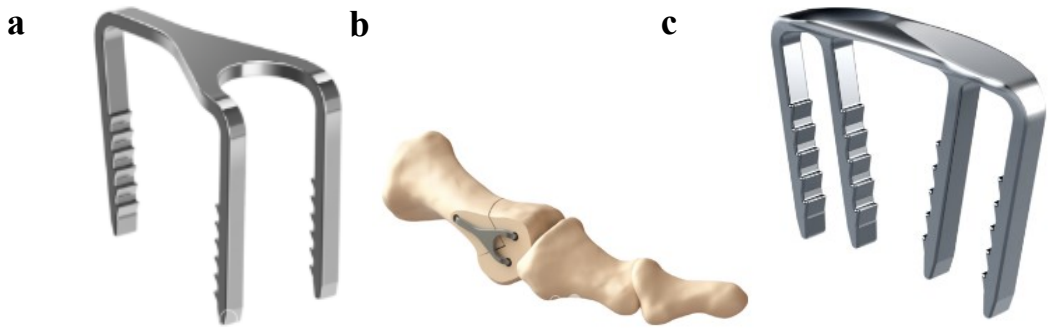

Figure 2-16 (a) and (b) SpeedTriad, (c) BME Elite by DePuy Synthes

There are several case studies on the use of NiTi staples. The successful application of NiTi staples has been also reported for patients with intra-articular fractures, including fractures of the patella, malleoli, olecranon, and lateral condyle [170]. NiTi staples have been even used for the treatment of larger bones such as mandible fractures [171]. In another study in 2018, Schipper *et al.* [172] evaluated radiographic results of superelastic Nitinol compression staples for hindfoot and midfoot arthrodesis. Based on this study radiographic union was seen in 93.8% of patient and 95.1% of joints using the NiTi staple. This study confirms the superelastic NiTi staples are safe and effective for hindfoot and midfoot arthrodesis, with a high radiographic union rate.

2.6.5 NiTi spinal applications

In 1975, Schmerling *et al.* [173], introduced Harrington rod made of NiTi for correction of scoliosis. To correct scoliosis, the spine would be distracted by an external device and a nitinol rod would be inserted. The NiTi is attached to the transverse processes of the vertebrae and adjusted to apply the correct force to the spine. Sanders *et al.* performed *in vitro* study on goats to evaluate the Harrington rod in 1993 [156, 174]. The NiTi rod was first deformed to match the existing curvature of the spine. After implementation, the rods were activated by radio frequency induction heating to apply

corrective forces to the spine. The scoliosis was corrected in all studied objects (n=6). In 2002, Wever *et al.* evaluated these NiTi rods in a pig study [175]. In this study, the NiTi rods were activated preoperatively. Inspections after 3 and 6 months showed the device was almost covered with the new bone formation. On the other hand, no correction was observed, and histologic examinations showed no evidence of a foreign body response.

The shape memory effect of NiTi has been utilized in a spinal vertebral spacer to replace a damaged intervertebral disc [175]. This implant would be deformed prior to surgery which enables a minimally invasive procedure. After insertion, the NiTi spacer recovers its shape via reaching to body temperature and no external heating is required. These NiTi spacers have also been developed via superelastic feature as well [176]. NiTi spinal spacers provide the required physiological stiffness, while titanium spinal spacers are extensively stiff and exhibit plastic strains under physiological loads [84].

2.6.6 NiTi nails

NiTi nails are another medical implant that are used for applying constant pressure for bone healing. DynaNail® Fusion System is designed for tibiotalocalcaneal (TTC) arthrodesis procedures to address degenerative conditions, correct joint deformities and revise failed total ankle replacements or arthrodesis non-unions. Once the implant is fixed in place with screws, the NiTi element applies constant compression or up to 6 mm of resorption or settling, unlike static, non-adaptive intramedullary devices that lose compression immediately upon frame removal or initial resorption. DynaNail can be used for the following indications, Post-traumatic and degenerative arthritis, Post-traumatic or primary arthrosis involving both ankle and subtalar joints, Revision after failed ankle arthrodesis with subtalar involvement, Failed total ankle arthroplasty, Non-

union ankle arthrodesis, Rheumatoid hindfoot, absent talus (requiring tibiocalcaneal arthrodesis), Avascular necrosis of the talus, Neuroarthropathy or neuropathic ankle deformity, Neuromuscular disease and severe deformity, Osteoarthritis, Charcot foot, Previously infected arthrosis.

2.6.7 NiTi foams

NiTi has also been used in the form of porous foams. A method of fabricating porous foams out of NiTi was patented in 1972 [85]. However, the corrosion resistance and biocompatibility of this type of NiTi due to the complex geometry was not well understood by the late 1990's [83, 86, 88-94, 126, 177]. Porous NiTi benefits from interesting features, including i) high strength to prevent fracture, ii) relatively low stiffness to achieve stiffness matching and minimizing stress shielding effect, iii) high toughness to avoid brittle failure, iv) shape memory behavior to facilitate implant insertion and ensure good mechanical stability within the host and provide constant force, and v) good biocompatibility to ensure healthy osseointegration [178].

Actipore™ is a porous NiTi foam introduced by the company Biorthex Inc (Montréal, Canada). For fabrication of Actipore, the pores are developed by means of solid expendable void former elements which are arranged in a selected spatial pattern in a forming cavity. Metallic particles are packed about the void former elements, the mix is densified, the void former elements are removed, such as by vaporization and the metallic particles are sintered. This porous NiTi implant has been utilized in two different applications: 1) The actipore PLF system introduced in 2001 was an interbody fusion device for lumbar fusion procedures, 2) The Actipore ACF system, introduced in 2005, was a similar device for cervical fusions. This device has received the CE mark and is

available in the European market, but not in the U.S. In 2004, the functionality of this device was evaluated in a sheep study and compared with Ti-6Al-4V intervertebral cages [179]. The osseointegration capacity of these two types of intervertebral cages were evaluated after 3, 6, and 12 months of implantation. CT-scans and histological testing showed a better osseointegration for the porous nitinol implant compared to the Ti-6Al-4V cage.

2.6.8 NiTi internal fixations

NiTi implants have been also used as a solution for hammertoe correction. Stryker and DePuy Synthes provided single piece NiTi implants which are activated using superelasticity or shape memory effect (Figure 2-17). Stryker implant, Smart Toe, is activated via body temperature and has been shown to provide fusion rates over 95% [180]. DePuy Synthes implant, Hammerlock, has a more complex geometry, provide multiaxial active stabilization, and is activated due to superelasticity feature [3].

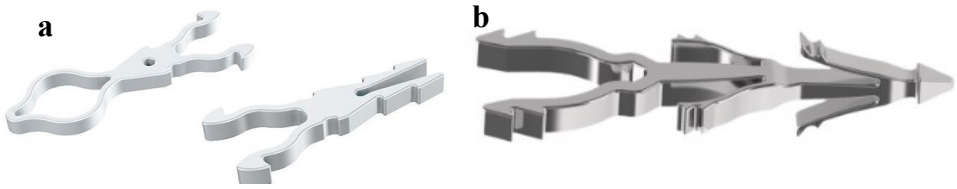

Figure 2-17 (a) Smart Toe by Stryker, (b) Hammerlock by DePuy Synthes

2.6.9 Hybrid NiTi Implants

Dynamic Compression Fixation System

The main limitation of NiTi staples is that they are only able to apply uniaxial compression load. In other word, NiTi staples are not able to bear torsional and bending loads and due to their dimension, they do not have high strength as skeletal fixation plates. In order to overcome these limitations, some researchers and companies have

combined NiTi staples with other types of fixations, such as Ti64 skeletal fixation plates. CrossRoads® Extremity Systems in 2017 introduced a hybrid fixation system called Dynaforce. This system consists of a wide variety of plate and NiTi staple options that incorporate continuous adaptive compression. Figure 2-18 shows the Dynaforce system attached to foot bone and separately. This system can be used in foot and ankle fixation.

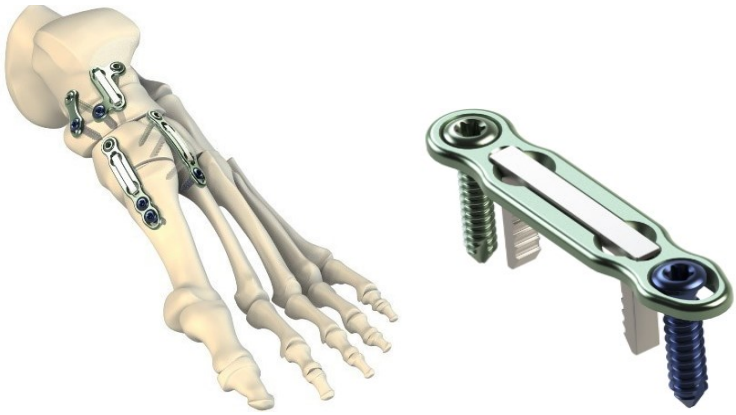

Figure 2-18 DynaFORCE™ Dynamic Compression Fixation System by CrossRoads® Extremity Systems, LLC

In another study the NiTi staples we combined with titanium fixations for fibula fracture [181]. Similar to the previous application, the Titanium (Ti-6AL-4V) skeletal fixation plates provide general stabilization and NiTi staples at different locations provide constant contact pressure. Figure 2-19 shows the CAD model and prototype of the hybrid setup.

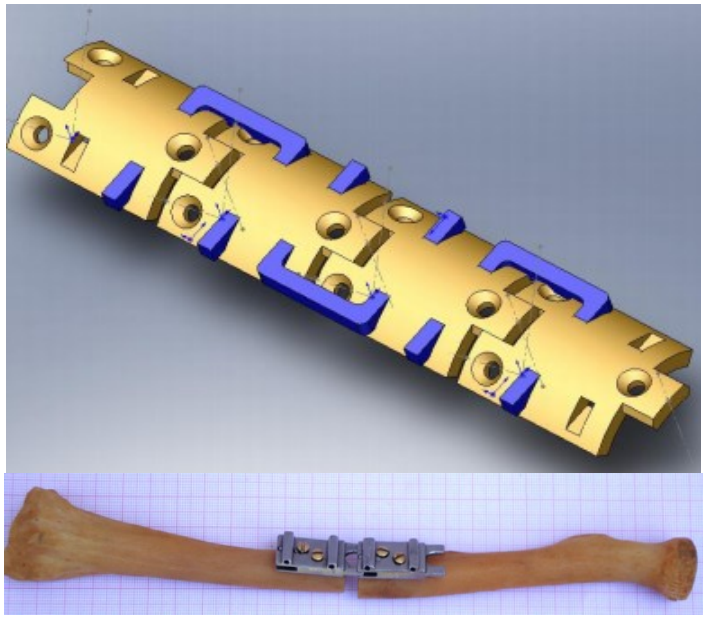

Figure 2-19 Hybrid fixation structure for fibula fractures

2.7 Mandibular reconstruction surgery

2.7.1 Bone remodeling

Bone tissue is an active material and constantly reshapes and changes its material properties. In response to mechanical forces, osteoclast cells resorb bone and osteoblast cells form new bone. This active process with which bone gradually changes its geometry and material properties is called bone remodeling [182]. Although bone remodeling is a gradual and life-long process, in conditions of disrupted mechanical loading bone remodeling happens faster. During bone remodeling, the bone resorption and bone formation are not coupled. New bones form in locations where additional strength is needed or where bone ingrowth is possible. On the other hand, bones resorb or weaken in locations where the normal forces decrease. As it was mentioned, bone remodeling can happen either internally or externally. The internal remodeling is the adoption of the density of the bone tissue, characterized by a change of porosity [183]. External or

surface bone remodeling refers to the removal or apposition of bone on the bone surface [184]. Bone remodeling serves different purposes and constantly adjusts the bone properties to meet the required mechanical needs [185] and also helps to repair micro damages in the bone matrix [186].

As a daily example, a broken arm in a cast gets weaker or in other words, its bone and muscles resorb due to the removal of the normal loads. The same thing happens to the muscles and bones of astronauts who spend a long time in space and their body is not under normal loading as on earth. On the other hand, it is well known that professional tennis players' dominant playing arm is much more built up than their other arm because of the same phenomenon [187].

Mechanical loading is the major factor that affects the bone structure. The mechanical hypothesis suggests that the mechanical loading in form of local strains on the bone causes bone loss or bone formation [188, 189]. In response to relatively consistent local strain, bone remodeling maintains a state of homeostatic. If the local strain is abnormal, local osteoblast or osteoclast are activated and cause bone remodeling. This process is called strain adaptive bone modeling and continues to the point that the local strains are normalized [187].

There is a threshold for the local strain to cause either bone formation or bone resorption and is defined by the minimum effective strain (MES) [153]. Strains that exceed the MES (50-500 microstrain) activate the bone cells in ways that change the size and configuration of the bone [190]. On the other hand, with local strains below the MES, the bone cells will have a "disuse-mode" state in which bone resorption occurs to remove the extra bone. Disuse-mode leads to local bone loss or a decrease in bone density [191].

Basic Multicellular Unit (BMU) is a group of cells responsible for controlling the bone remodeling [192]. A BMU control osteoclasts and osteoblasts in sequence to replace old pieces of bone with new bone. In addition, BMU detects and repair microscopic fatigue damage or microdamage caused by repeated strain during normal conditions. There is another threshold for a micro damage to be repaired by BMU and is called MDx (about 3000 microstrain). When the strain exceeds the MDx, BMU is no longer able to adequately repair the bone. This phenomena leads to a cycle of bone loss, increased level of strain and microdamage, and eventually cause fracture of the bone [193]. The fracture strain for young adults occurs at approximately 25,000 microstrains [194].

2.7.2 Effect of Internal Implants on Bone Remodeling

Bone architecture and properties are also affected by the presence of an internal implant. If the internal implant is used as a scaffold or a fixation structure, due to any difference in the material properties, the loading distribution on the surrounding bone will be altered. In most of the cases the implant has much higher stiffness in comparison with the bone tissue and because of that, the implant absorbs a significant portion of the normal loading. The removal of normal loading from the bone reduces the stress level on bone and is described by stress-shielding [195]. The stress shielding then reduces the microstrain level on the bone and cause unwanted bone resorption and osteopenia. As the bone resorption proceeds, a higher portion of the loads will be carried on by the implant and still the local microstrain on the surrounding bone does not increase to cause bone formation. Eventually, the implant will fail due to the increased level of loading and following by that the bone fails as well.

In addition to the mechanical effects of internal implants, there are several other parameters that characterize the host response to the implant and the ability of the implant to survive in the body [196]. The host response is characterized by three processes as Osteoinduction, Osteoconduction, and Osseointegration. Osteoinduction is the process in which the bone formation is activated. In a case of bone healing in a fracture osteoinduction is the most influential factor [195]. Osteoconduction is the ability of a material to be used as a scaffold and affects the bone attachment and bone ingrowth. Copper, silver, and bone cement that has low biocompatibility exhibit little to no osteoconduction. An osteoconductive implant must be porous to allow for bone ingrowth and fibrovascular tissue during osteoinduction [197]. Osseointegration affects the possibility of having a stable anchorage between bones and implant that results in a structural and functional connection [198]. In order to have a perfect osseointegration, the bone tissue must fill any gap between itself and the implant, and form new bone to repair any damage occurred during preparation of the implant site [199].

2.7.3 Mandibular reconstruction surgery

A variety of conditions such as oral cancer, benign and malignant tumors, and trauma affect the mandible and may necessitate removal of a segment of bone. These mandibular segmental defects cause different complexities including cosmetic deformity due to loss of facial contour, and difficulty with mastication, speech and swallowing due to loss of teeth. In addition to the bone loss, soft tissue such as the tongue, buccal mucosa, and skin may be involved and defected. Therefore, the goal of mandibular reconstruction is to address the bone and associated tissue defects by avoiding both functional and aesthetic problems.

In general, the treatment starts with resection of the defective region. A filling element which could an artificial bone, scaffold, non-vascularized or vascularized bone graft is used to fill the gap in the mandible [200-202]. Eventually, mechanical fixation plates and screws are used for providing additional immobilization. Free flaps need extra micro vascularized surgery, but on the other hand, the healing time will be reduced significantly in comparison with the other methods [203].

Although different methods and mechanisms have been used to address the segmental defects of the mandible, none of the currently available techniques can completely restore mandible function [204, 205]. Several large studies have reported the microvascular free tissue transfer with bone and the use of mechanical skeletal fixation plates and screws for the immobilization as the gold standard for reconstruction of mandible [201, 206-208]. Several donor sites can be used for providing the free flap including fibula, Radius, Scapula, iliac crest, and Femur. Numerous considerations are taken into account for choosing the best donor site for the patient. For longer defects requiring greater than 12-15 cm of bone, the fibula is a common site for bone harvesting. Although for shorter defects all other donor sites are available, the iliac crest is a great choice since it can provide sufficient mandibular height to support dental implants [209]. On the other hand, fibula cover larger defects up to 24 cm and also its removal causes minimum donor site morbidity [210]. Moreover, using a double barrel fibula graft, which is created by cutting a fibula into two segments while preserving the blood supply, and then folding the segments on top of each other increases the provided height by the fibula and allow the use of dental implants [211]. However, the associated soft tissue defects play a major role in flap selection in patients with shorter bony defects. In addition, donor

site considerations such as prior surgery or trauma, poor vascularity, or patient preference are considered by the surgeon. After healing, the newly grafted bone also provides seating for dental implant posts and improves chewing process for the patient.

2.7.4 Defect classification

Different classification systems have been proposed by researchers to describe mandible defects. Most of these schemes break up defects by the location and provide additional descriptors for the associated soft tissue. Boyd [212] uses the terms hemimandible, central, and lateral (HCL) while Urken [213] uses the standard anatomic breakdown of the mandible which is condyle, ramus, body, and symphysis. A more recent classification by Brown *et al.* [214] uses four classes. Class I (lateral), class II (hemimandibulectomy), class III (anterior), and class IV (extensive) with the addition and letter c for condylectomy as needed. For instance, “Ic” represents a lateral defect including the condyle. This recent system also captures the increasing complexity of the reconstruction procedure as the class of defect increases.

2.7.5 Plating

For the vast majority of patient titanium (i.e. Ti-6Al-4V or Ti64) skeletal fixation plate fixations are part of the reconstructive plan. These skeletal fixation plates have different shapes, thickness, and features. Thicker skeletal fixation plates also known as reconstruction plates, provide high levels of stiffness, while thinner skeletal fixation plates, also known as miniplates, provide lower levels of stiffness. In addition to the profile, bone fixation plates work either with locking or non-locking or both types of screws. In the next sections after introducing the loading mechanism and features of each

skeletal fixation plates, surgical approaches and eventually challenges of these skeletal fixation plates are discussed [215].

2.7.6 Locking and nonlocking bone fixation plates

Figure 2-20 shows a schematic of locking versus non-locking bone fixation plates. Non-locking plating works based on the friction generated between the plate and bone. Because of that, accurate contouring is required to match the bone contour. Not having a perfect match with the bone contour causes fracture initiation and lead to additional bone resorption. Furthermore, under an axial load, if the shear forces are greater than the frictional forces between the plate and bone, loss of fixation occurs due to toggling of the screws. In addition, compression of the plate to the bone surface under the plate area causes a reduction or even interruption of the blood supply to the bone. Delayed bone healing might happen as a result. In patients with reduced bone quality, screws cannot be tightened sufficiently and this may cause loosening of the screws and loss of stability. Despite these limitations, non-locking plating has shown good results in some cases with good quality bone [216].

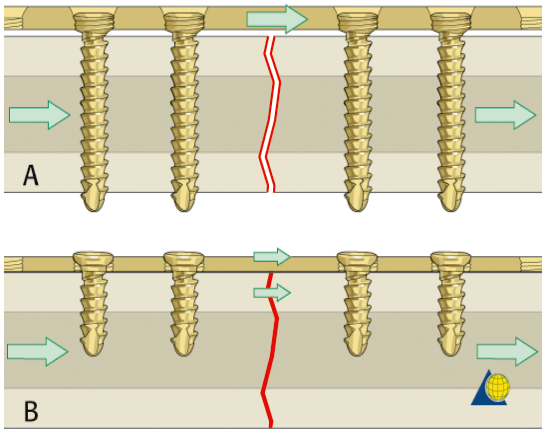

Figure 2-20 A) locking vs. B) non-locking bone fixation plates

In locking plates, screws lock to the skeletal fixation plate and create a fixed angle structure. Once the locking screw engages into the plate no further tightening is possible and therefore there is no compression between the plate and bone surface. Therefore, the periosteum will be protected and the blood supply to the bone preserved. Locking skeletal fixation plate locks the bone segments (e.g. bone graft or fractured pieces) in their relative position regardless of the tightening level. Although contouring the plate minimizes the gap between the plate and the bone, an exact match with the bone contour is not necessary for implant stability. Locking the screw to the plate, as can be seen in Figure 2-20, causes the axial force to transmit over the length of the plate and therefore the risk of a secondary loss of the intraoperative reduction is reduced [217].

2.7.7 Trauma kit, custom bend, and custom-made skeletal fixation plates

Bone fixation plates may be prepared via different methods. The first and most common type of skeletal fixation plates is available in prefabricated standard shapes and thicknesses, in trauma kits. The prefabricated skeletal fixation plates available in trauma kits are the most affordable type of skeletal fixation plates since they are mass produced.

The thickness of these skeletal fixation plates range from 1 to 3.5 mm and their profile includes straight and curved geometries with several holes for screws. After evaluating medical images of the patient (e.g. CT scan or MRI images), the surgeon decides about the required skeletal fixation plates available in a trauma kit. During the surgery, the surgical team choose the proper skeletal fixation plate, cut it to the desired length, and then bend it in a way that matches the bone's contour. The bending and forming which involves deforming around one or two axes are done manually by the surgeon right before placing the implant. Several cutting and bending tools are being used during the deformation process. In this type of surgery, deformation of the plate (especially thicker plates) could be the most challenging and time-consuming part of the surgery and might take up to several hours [218]. After shaping the skeletal fixation plates, two or more screws are used for fixing the implant to the host bone as well as the graft bone. Figure 2-21 shows a summary of the reconstruction surgery using these type of skeletal fixation plates.

Figure 2-21 Prefabricated bone fixation plates available in a trauma kit

2.7.8 Custom bend bone fixation plates

As it was mentioned in the previous section, one of the main challenges of using the prefabricated trauma skeletal fixation plates was shaping the skeletal fixation plates

during the surgery. This procedure is not straightforward and might include several trial and errors. Custom bend skeletal fixation plates are chosen and deform ahead of the surgery based on the CT scan of the patient. In this method, the 3D model of the defective region is created and usually printed ahead of time before the surgery and proper skeletal fixation plates are shaped based on that. The process of requesting a custom bend skeletal fixation plate adds additional time prior to the surgery, but on the other hand, reduce the time and complexity of the main surgery.

2.7.9 Custom made or Patient-specific bone fixation plates

Although custom-bend skeletal fixation plates reduce the time of the surgery, they are still not designed and fabricated based on the geometry of the patient and only have been deformed after the fabrication. Due to this limitation, surgeons are not able to cover every type of defected regions. As a solution, patient-specific skeletal fixation plates have been introduced to the market. In this approach, CT-scan images are used to create an exact virtual model of the patient's anatomy and then to design and manufacture customized skeletal fixation plates based on that. The patient-specific skeletal fixation plates may have variable profile thickness in different locations and the type, position, and direction of the screws are designed and customized for each patient based on the anatomy. After creating the final computer model (i.e. Computer-aided design or CAD file) of the patient-specific skeletal fixation plate, additive manufacturing or machining techniques (e.g. milling, CNC, etc) are used for the fabrication. In order to prepare a patient-specific skeletal fixation plate, followed by uploading the CT scan data to the manufacturer company, usually, video conferences between the surgeon and the manufacturer are made. The reconstruction plan is reviewed by the engineers and

surgeons and based on the input patient specific skeletal fixation plates are virtually designed. Eventually, after verification of the design, implants are fabricated and shipped to the clinic. The process of requesting, design and delivery of the patient-specific skeletal fixation plates may take about 10 business days and costs about 7 to 10 times more than the prefabricated skeletal fixation plates available in a trauma kit. However, patient-specific skeletal fixation plates not only save noticeable time during the surgery, but also perfectly fit the patient's anatomy and significantly decrease the chance of failure of the reconstruction surgery.

2.7.10 Principal risk of mandibular reconstruction surgery

Although bone fixation plates can be prepared in different ways, all different types are conventionally made of Titanium surgical grade 5 alloy (i.e. Ti-6Al-4V or Ti 64) [219]. T64 is a well-known biocompatible alloy and this biocompatibility is mainly because of its high corrosion resistance due to the resistive TiO2 oxide layer on the surface of the material. Ti64 also has a relatively high level of stiffness in comparison with the human cortical bone. Although Young's modulus and stiffness of human cortical bone depend on different factors, such as age, race, gender, and anatomy, it can be from 3 to 30 GPa, while Young's modulus for Ti64 is about 110 GPa [220]. Although the high stiff Ti64 skeletal fixation plates provide enough immobilization right after the surgery, they may cause bone resorption after the bone healing period. The reason is that due to the mismatch between the level of stiffness for the cortical bone and Ti64 skeletal fixation plates the loading condition in a reconstructed bone is disturbed. Based on the bone remodeling theory discussed earlier, the adjacent bone to the Ti64 skeletal fixation plates are shielded from the loads they normally saw and this stress shielding leads to

bone resorption and eventually failure of the surgery [221]. Although fixation plates can be removed when the bones heal, surgeons prefer not to remove the skeletal fixation plates unless in an emergency condition. The reason is that removing the skeletal fixation plates after the bone healing requires a second surgery and might injure the soft tissues as well as bones. However, in the case of an emergency, such as infection, or plate failure the skeletal fixation plate will be removed [222].

2.7.11 Patient-specific, stiffness-matched bone fixation plates

To overcome the problem of stress shielding without removing the skeletal fixation plate, one solution could be the use of bio-resorbable skeletal fixation plates that start to resorb after the bone healing period. If the hardware or some critical section of the hardware resorbs, the loading condition of the reconstructed mandible returns to its original form similar to a healthy mandible and prevent stress shielding. The main challenge in bioresorbable materials is to provide sufficient strength before the bone healing and to accurately control the resorption process. There has been some research in the field of bioresorbable materials [223], however, more research is required to have a functional bio-resorbable skeletal fixation plate.

The other solution is to modify the material properties and the mechanical response of the bone fixation plates. An ideal solution could be a skeletal fixation plate that benefits from a reduced level of stiffness that not only provides enough level of immobilization immediately after the surgery, but also prevent stress shielding after the bone healing. NiTi as introduced in the previous sections is a biocompatible material with a relatively low stiffness that offers other unique features such as superelasticity (SE). Imposing porosity to a NiTi part allows further reduction in the level of stiffness. Based

on this concept, stiffness matched patient-specific skeletal fixation plates have been introduced. The idea is to fabricate a skeletal fixation plate with the required level of stiffness for each case. To this end, Shayesteh *et al.* [53] studied the effect of a reduced level of stiffness on the stress distribution of a reconstructed mandible. In this study, a case of reconstruction on the lateral side of a human mandible was modeled and simulated using Finite Element (FE) model. This research showed a reduced level of stiffness can both provide enough immobilization after the surgery and have minimal stress shielding effect after the bone healing. In order to reduce the level of stiffness to a specific value, specific levels of porosity must be added to the structure.

2.7.12 Scope of the work

In this dissertation, the concept of stiffness-matched bone fixation plates has been applied in a realistic case. To this end, the first challenge was to calculate the required and optimized level of stiffness based on a patient's data. Followed by reaching to the desired level of stiffness by imposing porosity, different biological and mechanical features must be added to the skeletal fixation plates, such as the required supports for adding the screws and additional details to prevent infection. After finalizing the design of the stiffness matched skeletal fixation plates, the CAD files were prepared for fabrication via additive manufacturing. Stiffness matched bone fixation plates with different levels of stiffness were mechanically tested and used for calibration of the finite element simulations. Based on the first mechanical evaluations, process parameters and raw materials for additive manufacturing will be modified. The final samples will be evaluated for corrosion and Ni ion release. Eventually, the need for post-treatment and surface modification will be evaluated.

In the next chapter, the general methodology for the design, simulation, fabrication, post-processing, and mechanical evaluation of the stiffness matched skeletal fixation plates are discussed. Followed by the methodology, the results will be presented and eventually, in chapter five future works are presented.

Chapter 3

3. Methodology

In this chapter, different methodologies toward the fabrication and evaluation of the stiffness matched bone fixation plates are introduced and discussed. First, the design methodology that starts from the CT scan data is explained. Followed by the design procedure, the finite element models are discussed. By satisfying the design requirements, the additive manufacturing technique is used for fabrication of the samples and parts. Eventually, after the required post-processing procedures, the parts will be characterized. Based on the characterization outcome, proper modifications in the previous steps will be made.

3.1 Design

Three sets of samples were designed and fabricated in this project. Characterization samples were fabricated for measuring the mechanical properties and other features of the material. These samples were also used for evaluating the post-processing procedures. The second set is the patient-specific skeletal fixation plates that were designed base on medical images. Eventually, standard skeletal fixation plates similar to the ones available in a trauma kit were designed for mechanical evaluations.

3.1.1 CT scan data

CT scan, also known as computed tomography or computerized axial tomography scan, is a special X-ray test that produces cross-sectional (tomographic) images of specific areas of an object using computer-processed combinations of many X-rays measurements taken from different angles. The initial outcome of a CT scan test is grayscale cross-sectional images of an object in three perpendicular directions. The grayscale values in each pixel are known as CT values. Due to the difference in X-ray absorption and reflection, different materials may be distinguished in each cross section. CT scan data were originally used for evaluating the internal organs, diagnosis and preparing surgical or treatment plans. However, CT scan data may also be used to create 3D models of an object using the cross-sectional images. Different CT values can be assigned to different tissues or materials, and this way a 3D model including all internal parts may be created. The created model may be used for Finite Element modeling as well as the design of patient-specific implants or medical devices.

In this project, CT scan data are used for two different purposes. First, the CT scan data was used to create 3D models of the mandible. The models include cortical bones, cancellous bones, and the teeth. The models were used for different procedures from the design of the patient-specific skeletal fixation plates to the simulation of the reconstruction surgery. In addition, micro CT was used to scan a conventional standard skeletal fixation plate and to create the exact CAD model of that to be used for mechanical testing. The second use of the CT scan data was to assign material properties to the different tissues. As it was mentioned earlier in the previous chapter, mechanical properties of bone tissue differ from patient to patient and even depends on the location

in a single bone, such as mandible. The CT values unit obtained from the CT scan data at every single pixel can be used to define the material properties. To this end first, the Hounsfield unit (H) is calculated based on the CT value using the equation (2). Based on the definition the H value for water is 0 and it is -1000 for air. In this equation CT_W and CT_a are CT values of water and air, respectively [53].

$$H = 1000\frac{\mathrm{CT} - \mathrm{CT_w}}{\mathrm{CT_w} - \mathrm{CT_a}} \tag{2}$$

Bone density (ρ) is defined as the mean value expressed in Hounsfield units in each pixel. It is possible to find a relationship between the apparent density and the Young's modulus of an organ, such as the mandible bone. In this project we have used the equations in to calculate the Young's modulus of the mandible bone using the bone density measured from CT scan data [224].

Table 3.1 Young's modulus in terms of ash density [225]

E1	$E_1 = 6.382 + 0.255\,E_3$
E2	$E_2 = -13.05 + 0.013\rho$
E3	$E_3 = -23.93 + 0.024\rho$

3.1.2 Creating model of the mandible and the reconstruction case

Two types of models were prepared and used in this project. As the first step, in order to design and model the patient-specific skeletal fixation plates designed based on the mandible contour, a commercially available model of a mandible was purchased. Several validation procedures such as the design of the general geometry on the skeletal fixation plates and the effect of modulating the stiffness of the skeletal fixation plates were evaluated using this model.

The second model was created using CT scan data. CT scan data of a healthy unknown male subject was used as the baseline for the design of the stiffness marched skeletal fixation plates. CT scan data were imported to Mimics software (Materialise, Belgium) and STL files were created based on that. STL file is a type of computer modeled file that only includes surfaces. The surface is made of fine triangles and their dimension is defined based on the resolution on the STL file. 3-matic software (Materialise, Belgium) was used to create volume mesh inside the STL models. Elements with volume mesh were then imported back to Mimics and material properties for bone were assigned based on the Hounsfield unit and equation X to each volume mesh.

To create the case of reconstruction, two lateral cuts were made on the left side of the mandible models. The cuts were made vertically and created a 3 cm gap to simulate a lateral defect. In order to fill this gap, a CAD model of a double barrel fibula was created based on available CT scan images. For some cases, the same piece which was cut from the mandible was used to fill the gap. The reason for that was to evaluate the design process of the bone fixation plates where the surface of the bone is not smooth. Eventually, CAD file of the fibula and the mandible model were assembled together.

3.1.3 General geometry of the required skeletal fixation plate

The assembled structure including the resected mandible model, teeth, and the double barrel fibula graft was used as the baseline for the design of the skeletal fixation plates. In general, a single reconstruction skeletal fixation plate is designed in a way that covers the fibula section and some portion of the host mandible. The covered portion of the host mandible should contain two or more screws to prevent torsion. In some cases, one or two miniplates are added to the structure to provide additional immobilization. As

a reference to simulate and compare different types of bone fixation, we considered a reconstruction plate and two miniplates for all the cases. The surface profile of the standard skeletal fixation plates is a wave-like surface with wider width where the screws are added (Figure 3-1). However, for patient-specific skeletal fixation plates there is no need to use the standard surface profile since the screws can be added where they are needed. For the comparison purposes, we have chosen the surface profile of the standard skeletal fixation plates as the general shape of the reconstruction and mini plates.

Figure 3-1 General shape of standard skeletal fixation plates [226]

Similar to the conventional patient-specific skeletal fixation plates, by considering the anatomical structure obtained from the CT scan data, screws were selected and added to the skeletal fixation plates. The main criteria for the screws' selection and placement are to guarantee penetration to the cancellous bone and to prevent any intersection with teeth roots and other screws.

3.1.4 Required stiffness for the skeletal fixation plates

In order to calculate the required level of stiffness for the skeletal fixation plates, first, the material properties of the cortical bone must be measured. The method explained in the CT scan section was used to measure the mechanical properties of the adjacent bone to the skeletal fixation plate. The average Young's modulus of the surrounding region was considered as the reference for the design. The goal is to modulate the stiffness of the skeletal fixation plate by imposing porosity to have an equivalent Young's modulus close to the bone tissue. To this end, a cubic structure with

different levels of porosity was modeled and simulated via Finite Element method. The equivalent Young's modulus for the porous cube was defined by dividing the equivalent stress by the overall strain of the structure. The equivalent stress was defined as the load divided by the surface of the cube. The strain was calculated as the change in direction of the load divided by the initial length. With a trial and error procedure, the required level of porosity to achieve the desired level of stiffness for each case was calculated.

The other method to calculate the required level of stiffness for the skeletal fixation plates is to simulate the reconstructed mandible and set criteria for the critical stage of the reconstruction, which is when the bones still have not healed. The minimum requirement for the stiffness of the skeletal fixation plates may be calculated in a way to provide the required level of immobilization immediately after the surgery (i.e. when the bones have not healed yet). The required level of immobilization can be related to the created gap distance between the bone graft and the host mandible when the mandible is under realistic loadings. In this project, the first approach, (i.e. equivalent Young's modulus) has been used for calculating the required level of stiffness.

3.1.5 Imposing porosity to the patient-specific skeletal fixation plates based on the required stiffness

Required stiffness or equivalent Young's modulus obtained using the CT scan data is the basis for imposing the porosity. The porosity is made of an arrangement of single pore cells distributed all over the part. The unit pore cell may be designed with different criteria and, therefore, may have different geometries. Different types and levels of porosity have different effects on the mechanical response or stiffness of the part. Due to the small thickness of the skeletal fixation plates and the fabrication resolution, which

is discussed in the next sections, we had some limitation in choosing the pore type. Although different criteria may be used to produce and optimize the type of porosity, for this project we have chosen a single type. The selected pore cell is a hollow cube with only the edges. The dimension of the cubic cell is considered fixed as 1 mm and by changing the thickness of the edges the level of porosity changes.

In order to impose the above-mentioned porosity to the skeletal fixation plates, cubic samples, or any other required sample, the first step is to create an STL version of the CAD file. The reason is that due to the too many constraints in a CAD file of a porous structure, the file will be too large and almost impossible to process. On the other hand, STL files are only made of triangles on the surfaces and no other constraints are included in the STL version. After the conversion into STL, different software may be used for imposing the porosity. We have used 3-matic software to this end. In this method first, a lattice with the general shape of the pores is created inside the parts. The lattice is created in a way that only covers inside regions of the part and is created based on the unit cell. At this stage, the lattice is only made of zero thickness wires and because of that does not add complexities to the model. After reaching the desired lattice, the next step is to assign thickness to each wire and create a volume. The created volume is also an STL file. In order to create required supports for the screw heads and provide a support for the whole structure, a thin cover is added to the sides and the top portion of the skeletal fixation plates. This final step is not needed for the design of the other types of porous samples such as the corrosion samples. The process of adding porosity to the skeletal fixation plates is shown and summarized in Figure 3-2. Eventually, Figure 3-3 shows the

summarized procedure to design the stiffness-modulated skeletal fixation plates starting from the CT-scan.

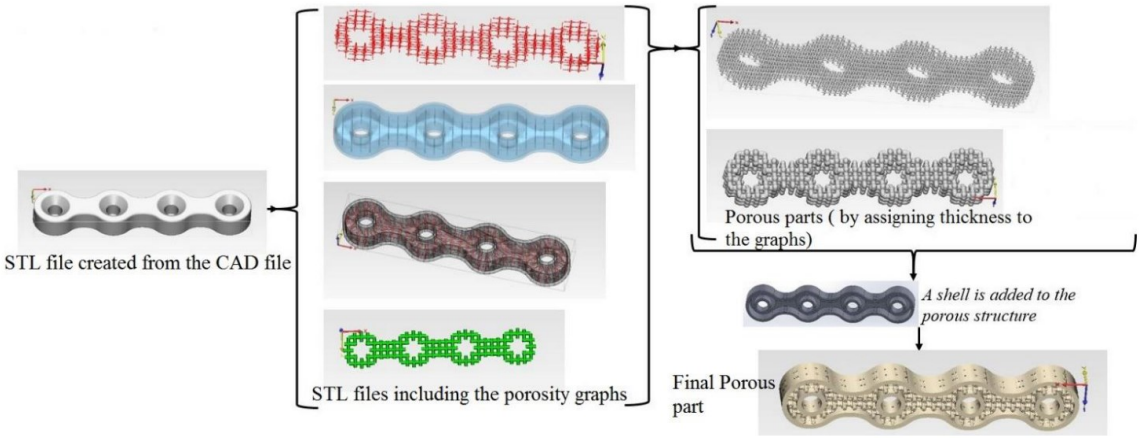

Figure 3-2 The summarized process of adding porosity to the skeletal fixation plates

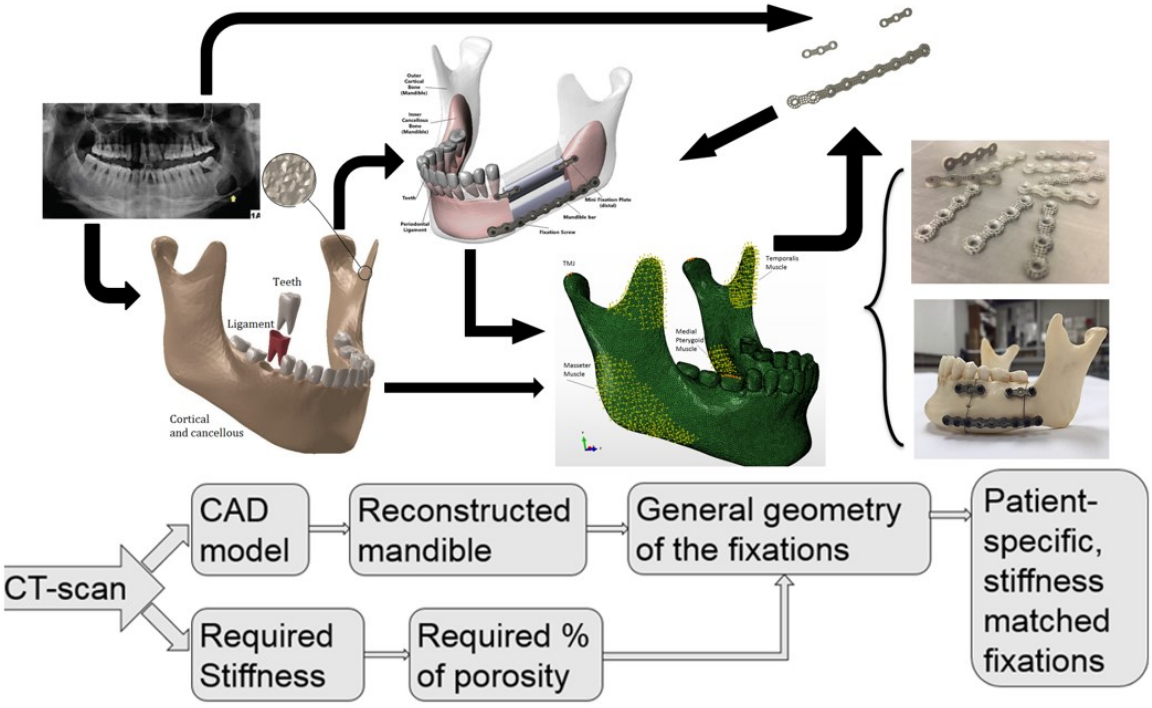

Figure 3-3 Summarized design methodology to create the patient specific skeletal fixation plates starting from CT scan

3.1.6 Design of the standard skeletal fixation plates available in a trauma kit

Although the ultimate goal is to fabricate custom-made (i.e. patient-specific) skeletal fixation plates based on the anatomy of the patients, the profile of the standard skeletal fixation plates was also used for comparison purposes and for conducting standard mechanical evaluations. Straight four-hole reconstruction skeletal fixation plates were designed in SolidWorks software based on standard plates available in trauma kit by KLS Martin. The selected skeletal fixation plate has a 3 mm thickness and is 30 mm long. Different levels of porosity were imposed on this structure for comparison purposes as well as the mechanical evaluations. The porosity was added similar to the method explained before. Other than the straight form, as a representative of the curved skeletal fixation plates, an angled skeletal fixation plate was selected and reproduced. However, for all the mechanical evaluations the straight skeletal fixation plates were used.

3.1.7 Cubic samples for characterization

In addition to the actual testing of the skeletal fixation plates, porous cubic samples were designed for a better evaluation of the porous structure as well as the corrosion assessments. To this end, the same level and type of porosities similar to the bone fixation plates were also imposed to 9 mm cubic samples. These cubic samples have a larger area in comparison with the skeletal fixation plates and could be a better candidate for evaluating the type and level of porosity. The goal for the corrosion samples was to evaluate the effect of adding porosity on the corrosion resistance of the NiTi parts. In addition to porous samples, a bulk sample was also used for the comparison. For the electrochemical samples, a 10 mm handle was also added to the top

surface of the cubic samples. This added handle works as a gripper during the test and provide a better connection.

3.2 Modeling and simulation:

Finite Element (FE) modeling was used in different stages for this project. The first and a great portion of the simulations were used to model the reconstruction surgery and to obtain the stress distribution in different cases. We have modeled a healthy mandible as well as a reconstructed mandible before and after healing. The reconstructed cases were modeled with the use of conventional Ti-6Al-4V plates as well as the NiTi patient-specific skeletal fixation plates. Stress distribution on the healthy model was used as the reference for the reconstructed cases. The pure tension of the standard skeletal fixation plates with different levels of porosity was modeled via FE.

3.2.1 Preparing the parts for finite element simulations

After the modeling step, all parts need to be meshed. Hypermesh (Hypermesh, Troy, MI, USA) was used to mesh the models with 4-node tetrahedral elements (C3D4). The convergence study was performed for different components and based on that the optimized number of elements is reported in Table 3.2.

Table 3.2 Mesh type and number of elements for different components

Model Component	Element	
	Type of element	Number of elements
Resected mandible	3D, Solid, Tetrahedral, Deformable	218,328
Teeth (13 Total)	3D, Solid, Tetrahedral, Deformable	65,179
Ligaments (13 Total)	3D, Solid, Tetrahedral, Deformable	21,053
Top Graft	3D, Solid, Tetrahedral, Deformable	42,065
Lower Graft	3D, Solid, Tetrahedral, Deformable	45,037
Fixation hardware(s)	3D, Solid, Tetrahedral, Deformable	58,327
Screws (10 Total)	3D, Solid, Tetrahedral, Deformable	67,027

Followed by meshing the components of the mandible, all the parts were assembled to model the reconstruction surgery. In order to simulate the locking skeletal fixation plates in which screws are locked into the skeletal fixation plates, the constraints between screws and skeletal fixation plate as well as the screws -host bone and screws-bone graft were defined as tie. The constraints between teeth-ligaments and ligaments-cortical bone were defined as tie too. In order to simulate before and after healing periods, different friction factors were defined between the host mandible and bone graft. The friction factor of 0 was chosen for immediately after the surgery when the bones have not still healed, and the friction factor of 1 was chosen for simulating the after the healing period.

All the components and materials except the NiTi parts were modeled as linear elastic. Table 3.3 summarizes the material properties of different bone tissues, teeth, ligament and the Ti64 hardware [227-229]. Cortical and cancellous bone were modeled

as anisotropic materials, while other components were modeled as isotropic. For all the reconstructed models, Ti64 screws were considered.

Table 3.3 material properties of different components

Material	E_x (MPa)	E_y (MPa)	E_z (MPa)	υ_{xy}	υ_{yz}	υ_{xz}
Cortical Bone- Symphysis region	23,000	15,000	10,000	0.3	0.3	0.3
Cortical Bone- Angle region	20,000	12,000	11,000	0.3	0.3	0.3
Cortical Bone- Rest of mandible	17,000	8,200	6,900	0.32	0.325	0.31
Cancellous Bone	960	390	320	0.3	0.3	0.3
Cortical- fibular graft	26,800	26,800	26,800	0.3	0.3	0.3
Cancellous- fibular graft	1,650	1,650	1,650	0.3	0.3	0.3
Teeth	17,600	17,600	17,600	0.25	0.25	0.25
Periodontal Ligament	2.7	2.7	2.7	0.45	0.45	0.45
Ti-6Al-4V	112,000	112,000	112,000	0.3	0.3	0.3

For modeling the thermomechanical properties of NiTi skeletal fixation plates in Abaqus, a user-defined subroutine (UMAT) developed by Dr. Kadkhodaei's group was used [229-231]. This UMAT is capable of modeling the superelastic and shape memory behavior of NiTi and is developed based on microplane theory. As the first step in simulations, the UMAT is calibrated and verified to make sure it is possible to model mechanical response of the NiTi components. The input parameters for this UMAT are the transformation temperatures, austenite and martensite Young's modulus, Ca and Cm, critical stresses and the Poisson's ratio. All these parameters can be obtained via DSC and mechanical testing of standard coupons at different temperatures. More information about the UMAT can be found elsewhere [227-229].

3.2.2 Boundary conditions and loading scenarios

The human mandible is always under a multiaxial loading scenario [157]due to different masticatory muscles and the bite forces. Even when the mandible is at rest and there is no bite force, still the muscles are active, and mandible is under a multiaxial loading. In order to simulate a realistic critical case of loading on the reconstructed and healthy mandible models, we have simulated a case of maximum bite force applied on the first right molar tooth. For the modeling purpose, the location of the bite force (i.e. first right molar tooth) is considered as fixed (i.e. displacement was set to zero) and all the reaction forces proper to that bite force were applied to the model at the location of the muscles.

The level of muscle forces depends on different factors, such as occlusion state (maximal chewing or soft food chewing), and the bite condition (i.e. balanced or unbalanced loading, bilateral or unilateral loading, grinding, or clenching) [225]. In this study as the main input, the muscle forces related to a maximum bite force of 526 N on the first right molar were used based on a work by Korioth *et al.* [232]. However, this maximum bite force was considered for a healthy mandible where there is no reconstruction done in any region. Based on the literature, the reconstruction surgery reduces the chewing power of patients by up to 40% [129]. Because of this fact, we have used 60% of the maximum bite force, and therefore muscle forces measured by Korioth *et al.* [233] as the critical loading condition for the reconstructed mandibles.

In general, we have considered two types of models, a) one model of the healthy mandible, and b) three model of the reconstructed mandibles. Although the resection case, as well as the skeletal fixation plates arrangements, were similar in all the

reconstructed mandibles, different types of skeletal fixation plates were used. The healthy mandible model was simulated with the 60% of maximum bite force and was used as the reference. The first reconstructed mandible was simulated with the same level of loads (i.e. 60% of maximum bite force) and by considering conventional skeletal fixation plates (i.e. Ti64 skeletal fixation plates) as the fixations. The second reconstructed mandible was modeled again with the same muscle forces and by considering NiTi stiffness-matched skeletal fixation plates. Eventually, the third reconstructed mandible model was simulated with the same muscle forces beside a pre-tension applied to the NiTi skeletal fixation plates. In reality, the pretension can be applied via stretching the skeletal fixation plates prior to the installation. Each of the three reconstructed mandible models was simulated in two conditions, before and after the healing stage.

3.3 Fabrication and post-processing

Selective laser melting (SLM) technique, as it is discussed in chapter 2, is used for fabrication of NiTi coupons and skeletal fixation plates. In addition to the skeletal fixation plates with standard profile and different levels of porosity, a set of patient-specific skeletal fixation plates and compression samples were fabricated in this project. Compression samples were used to extract the required material parameters for and calibration of the UMAT. The procedures for measuring these parameters was explained in the simulation section. The fabrication process for the standard compression samples follows the same parameters as the bone fixation plates. After calibrating the UMAT with mechanical compression data, we are able to simulate NiTi components in all other models, such as the reconstructed mandibles.

In order to use selective laser melting, first, the CAD or STL file of the parts must be created. STL files are then placed on a virtual substrate similar to the one in the main fabrication machine. The parts may be placed in different directions on the substrate which may lead to different material properties for the parts. Therefore, we have reported the build direction for each fabrication. After placing the parts over the substrate, required support structures are added to the build and eventually the parts and supports are sliced into thin layers based on the desired layer thickness.

Phenix PXM SLM machine from 3D systems was used for the fabrication of NiTi parts and samples. The PXM machine is equipped with a 300 W Ytterbium fiber laser, with a Gaussian profile (TEM00) and the quality of $m^2<1.2$. The laser diameter at its current setup is approximately 80 μm. The machine uses a scraper and a roller mechanism to spread the powder and create a powder layer. The fabrication chamber of the machine can be divided into two sections, a feeding area, and the build substrate. Before starting the fabrication process, Argon gas is purged into the chamber to reduce the level of oxygen and prevent oxidation. Followed by purging Argon, an internal heater pre-heats the chamber to 100C. After preparing the initial build conditions, the fabrication process starts by upward movement of the feeding piston and providing the required powder for the first layer. The metal scraper moves and collects the powder from the feeding piston, and the roller deposits the collected powder on the build plate. By preparing the powder bed, the laser activates and selectively scans and melts the powder bed based on the geometrical data of the first layer. The melted areas solidify and create a dense region surrounded by loose powder which is the first layer on the parts and supports. The building piston moves down as the thickness of a single layer and the

whole process repeats until the final part is fabricated. At the end of the process, the loose powder and supports are removed, and the fabricated part is ready. Figure 3-4 shows a schematic of the internal sections of the Phenix PXM machine.

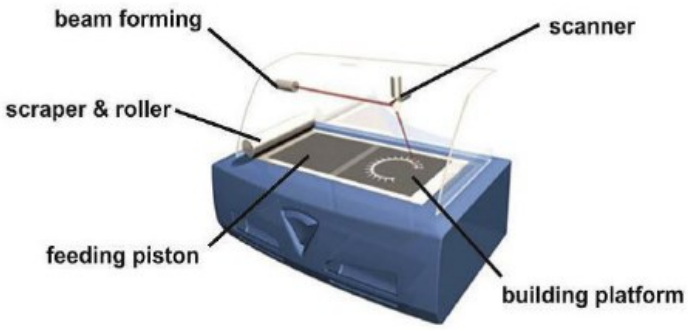

Figure 3-4 Schematic of the Phenix machine

3.3.1 Powder selection

The powder used for the SLM process significantly affects the part quality and thermomechanical properties of the fabricated AM parts. Powder composition, impurity, particle size and shape, and flowability are some the main properties of the powder that must be chosen and carefully monitored. Electrode Inert Gas Atomization (EIGA) method is used to atomize the NiTi ingot and prepare the powder. Spherical powder particles created by EIGA method provide a high powder bed density and show a good flowability. The flowability and powder bed density are two important features that could improve the SLM process by reducing the porosity in the parts. Although a fine particle size increases the resolution of the fabricated parts and allows using thinner layers, the flowability decreases for as the particle size decreases. Therefore, an optimized powder particle size must be selected for the SLM technique. Based on a study conducted by Haberland *et al.* [9], medium-size powder particles of 25-75um provide a good balance between the flowability and the resolution of the fabricated parts. Two types of powder

one Ni50.09-Ti (at. %) and Ni50.8-Ti (at. %) were used in this project. To distinguish these two powder types, the first one is recognized by Ti-rich and the second on by Ni-rich in this project. Ni-rich and Ti-rich NiTi ingots were provided from Nitinol Devices & Components, Inc (Fremont, CA). The EIGA process was done by TLS technique GmbH (Bitterfeld, Germany) to prepare spherical powder particles of 25-75 μm.

3.3.2 Process parameters

In addition to the powder, there are several process parameters that must be tuned and optimized for a successful SLM process. The layer thickness is the first parameter that must be set based on the powder particle size. The selective melting process is done by the laser and therefore the laser properties, such as the laser power, beam diameter, scanning speed, scanning strategy, and hatch spacing must be tuned and optimized based on the powder composition, particle size, and the layer thickness.

Two different energy input and process parameters have been used in this project. For the initial fabrication the energy input of 55.5 (J/mm^3) and for the second set of fabrications the energy input of 83.4 (J/mm^3) was used. The reason was that the second set of process parameters showed better functional properties in a parallel study in our group [234]. Table 3.4 shows the summarized process parameters used for the SLM process.

Table 3.4 Process parameters used for the fabrication

Effective Laser power (W)	**Layer thickness (μm)**	**Scanning velocity (m/s)**	**Hatch distance (μm)**	**Energy density (J/mm^3)**
250	30	1.25	120	55.56
250	30	1.25	80	83.34

3.3.3 Re-melting or selective laser re-melting (SLRM)

In addition to the conventional selective laser melting procedure used for fabricating the parts in this study, a selective laser re-melting (SLRM) approach was investigated to improve the density and to improve the surface condition. This procedure is manly similar to the conventional selective laser melting, but in each layer after selective melting the powder layer, and prior to the deposition of the new powder for the next layer, laser is utilized aging (re-melting) to perform another melting on the already-melted region. This re-melting procedure could hypothetically reduce the internal voids/pores and lead to a denser part (i.e. parts with a higher relative density). In addition, the re-melting could also improve the surface condition of the part. This approach has been studied as potential method to improve the SLM fabricated parts.

3.4 Characterization and Mechanical evaluation

3.4.1 Transformation temperature measurements

A Perklyn-Elmer DSC Pyris 1 was used for differential scanning calorimetry (DSC) and determine the transformation temperatures. Temperature range for the NiTi samples was at least from -100℃ to 150℃ and the heating and cooling rate is 5℃. 25 to 40 mg of NiTi samples were used as DSC samples. Samples were polished prior to the DSC to establish good thermal contact. Samples are thermally cycled and the heat flow versus temperature is recorded. On the calorimetric graph, phase transformation temperatures can be measured by drawing two tangent lines at the beginning and the end of each peak as it is shown in Figure 3-5.

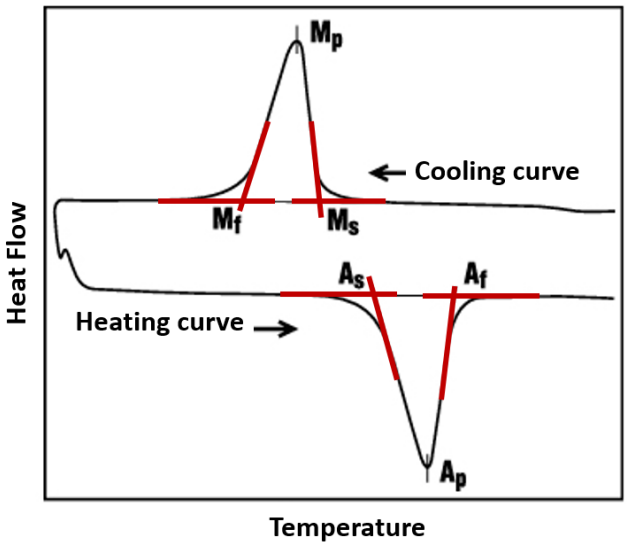

Figure 3-5 A typical DSC plot for a NiTi sample

3.4.2 Tensile test of the standard skeletal fixation plates

Bose ElectroForce 3300 with environmental chamber was used for tensile testing of the samples. Porous straight skeletal fixation plates designed based on standard plates available in trauma kits were used for the tensile test. For testing these skeletal fixation plates two type of grippers were designed and used. The first type as it is shown in Figure 3-6 was designed to grip the skeletal fixation plates using a screw. The main problems with this type of gripper was the significant effect of screws on the overall displacement of the skeletal fixation plates, existence of an unwanted bending moment on the skeletal fixation plates, and the early failure of the screws in comparison with the skeletal fixation plates.

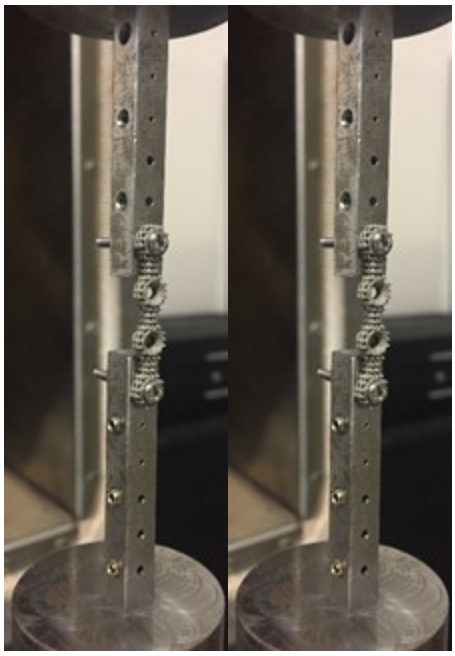

Figure 3-6 First gripper type designed for the tensile mechanical test

In order to study the mechanical properties of the skeletal fixation plates not affected and limited by the screws, the second type of grippers as shown in Figure 3-7.b were used. In these grippers, similar to the standard tensile grippers for flat samples, the skeletal fixation plates were gripped at the top and bottom portion. For evaluating and measuring the displacement, a video extensometer and a DIC (Digital image correlation) system were used. The DIC system enables full-field measurement of the strain all over the visible surface of the sample. An IR camera (Micro-Epsilon Compact high-speed by thermoIMAGER) was used to verify and monitor the temperature of the samples inside the environmental chamber (Figure 3-7).

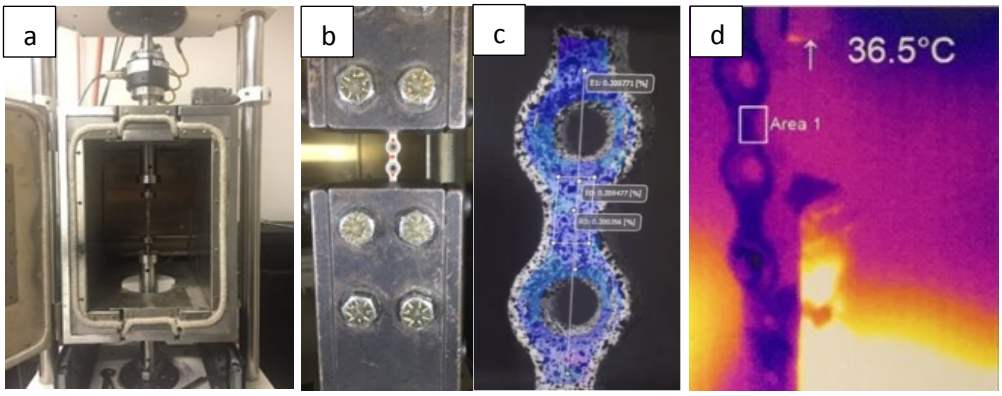

Figure 3-7 Experimental setup for testing the skeletal fixation plates (a) environmental chamber, (b) Test grippers, (3) a full filed strain measurement used as virtual extensometer, (d) View of the IR camera for measuring and verifying the testing temperature

In addition to the above setup, a 25 kN TestResources 910 Series Servo hydraulic fatigue test machine (TestResources, Shakopee, USA) was used for testing the standard tensile and compression samples in this study. All samples were loaded with a strain rate of 10^{-4} (s^{-1}) to make sure of isothermal condition. For the tests that were not at room temperatures (e.g., body temperature or A_f+15℃) a mica band and a controller box by Omega was used to control the temperature. A 2D digital image correlation (DIC) system (correlated solutions, Irmo, USA) by Correlated Solutions, which uses a 5-megapixel camera, a Tonika 100 mm lens, and VIC_2D software was employed to measure the strain. The samples were painted with black and white speckle pattern for DIC measurement.

3.4.3 Chemical analysis, chemical polishing, and SEM analysis

The chemical analyses were performed on the SLM bone fixation plates according to ASTM 2063 standards (Table 3.5). Two different etching solutions (Table 3.6) and three different exposing times (2, 4, and 6 min) were utilized to chemically polish the superelastic porous bone fixation plates [235-237]. To evaluate the polishing

procedure a FEI Quanta 3D FEG scanning electron microscopy (SEM, Thermo Scientific, Waltham, USA) was used.

Table 3.5 ASTM 2063 test method description.

Test method	Description
ASTM E1409-13	Inert gas fusion for oxygen and nitrogen
ASTM R146-83	Vacuum hot extraction for hydrogen
ASRM E1941-16	Combustion infrared detection for carbon
ASTM E1097-12	Direct current plasma emission spectroscopy for all other elements

Table 3.6 The chemical composition of two etching solutions used for chemical polishing.

Etching Solution	Chemical Composition	Ratio ($HF–HNO_3–H_2O$)
Solution 1	HF (10%), HNO_3 (40%), H_2O (50%)	1:4:5
Solution 2	HF (5%), HNO_3 (50%), H_2O (45%)	1:10:9

3.4.4 Surface roughness measurements

A Zygo NV5000 3D optical profiler and a Keyence VHX-600 Digital Microscope were used for surface roughness measurements of the samples. Arithmetical mean height indicates the average of the absolute value along the sampling length. Ra is referred to as the arithmetic mean roughness (Figure 3-8). Sa is the extension of Ra (arithmetical mean height of a line) to a surface. It expresses, as an absolute value, the difference in height of each point compared to the arithmetical mean of the surface (Figure 3-9). These parameters are used generally to evaluate surface roughness.

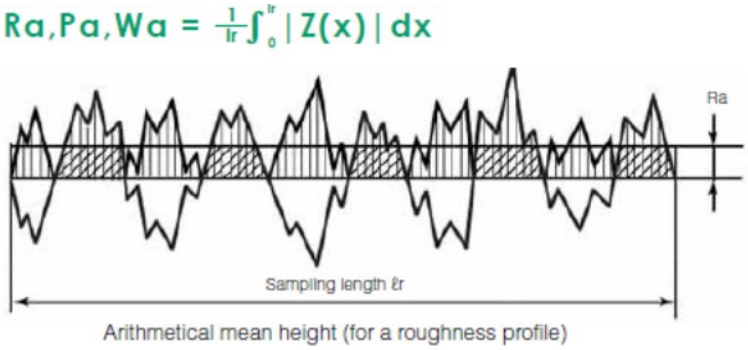

Figure 3-8 Shematic of demonstration of Ra for surface measurement. Ra is the arithmetical mean height indicates the average of the absolute value along the sampling length.

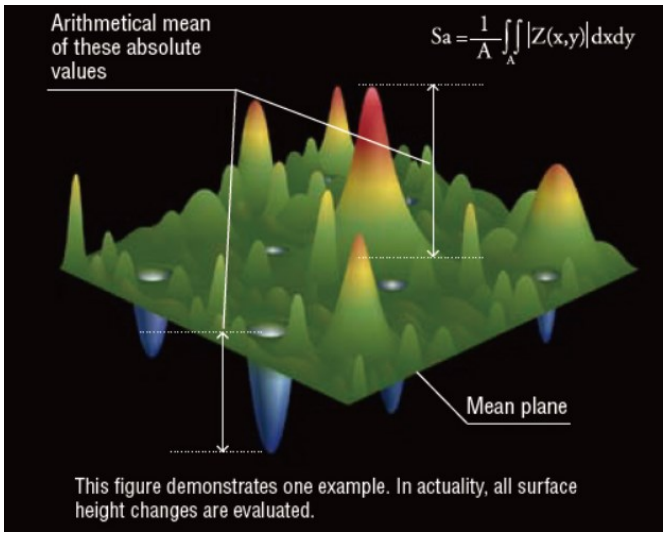

Figure 3-9 shematic of demonstration of Sa for surface measurement. Sa expresses as an absolute value, the difference in height of each point compared to the arithmetical mean of the surface.

3.4.5 Heat treatment procedure

Standard compression samples were used for optimizing the solution annealing. Lindberg/blue M BF514541 Box furnace used for heat treating the specimens (Figure 3-10). The furnace can reach to 1200 C and provides a tube chamber than can be merged with an inert gas to prevent oxidation. In order to minimize the oxidations, samples were

separated and placed on ceramics, and pure titanium shadings were used beside the main samples.

Figure 3-10 a) Fabricated sample to study the solution annealing, b) heat treatment setup including the tube furnace box and pure argon container.

3.5 Corrosion assessment of the porous NiTi parts

In order to evaluate the biocompatibility and the corrosion resistance of the additively manufactured NiTi parts, two different tests were considered; immersion test and electrochemical test. A conventionally fabricated sample cut from the original NiTi ingot was used as the reference sample. Bulk and porous 9 mm cubic samples with the same level of porosity as used for the skeletal fixation plates were designed for the immersion test. Samples for the electrochemical corrosion characterization were fabricated with the same dimensions with an additional hook connected at the top surface of the cubes for better electrical connectivity during the test. The fabricated samples were then separated from the base using an EDM machine. Figure 3-11 shows the CAD file and fabricated samples for immersion and electrochemical test. Samples were polished using a sandblaster and the samples electrochemical corrosion test were further polished

using SiC papers from 180 to 1500 grit. Prior to each test, samples were cleaned by water and ultrasonically by ethanol.

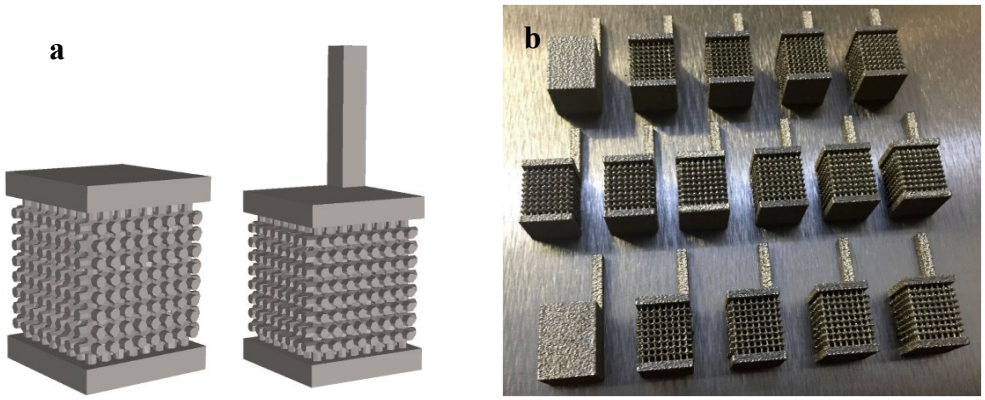

Figure 3-11 (a) CAD file of the porous samples used for corrosion study, (b) Fabricated samples for the corrosion assessment. [9]

3.5.1 Immersion test (Ni Ion Release)

In order to evaluate the corrosion resistance and Ni-ion release of the samples, NiTi parts with the same apparent surface area were submerged in a simulated body fluid (SBF). SBF mimics the internal environment of the human body and the evaluation of the parts in this media represents the corrosion resistance inside the human body. 20 mL SBF solution at pH 7.4 and at 37 C was used for each sample [238]. The ionic concentrations (mmol/L) of the SBF used in the present study were determined by Hansen *et al.* [15] and were as follows: 142.0 Na+, 5.0 K+, 1.5 Mg2+, 2.5 Ca2+, 147.8 Cl−, 4.2 HCO3 −, 1.0 HPO4 2− and 0.5 SO4 2−.

The temperature of the samples was maintained at 37ºC by placing the tubes in a rotary incubator throughout the period of the test. Continuous rotation of the tubes at 20 rpm was used to accelerate the corrosion process. After 3 days the amount of Ni-ion release in ppb was measured using Inductively Coupled Plasma Atomic Emission Spectroscopy (ICP-AES). For each sample 1 mL of the SBF medium after 3 days was

diluted with deionized water at a ratio of 1:10 to produce an adequate sample size and ion concentrations for spectrometry. The samples were analyzed using the X-series 2 from Thermo Scientific.

3.5.2 Electrochemical test

For the electrochemical corrosion test, the surface area of the samples exposed to the medium was limited by molding the samples into epoxy resin. For the additively manufactured and the conventionally fabricated samples, the same exposed area of 0.5 cm2 was chosen for a better comparison. For all the samples the side surfaces were exposed and the top and bottom surfaces were covered with epoxy as can be seen in Figure 3-12.

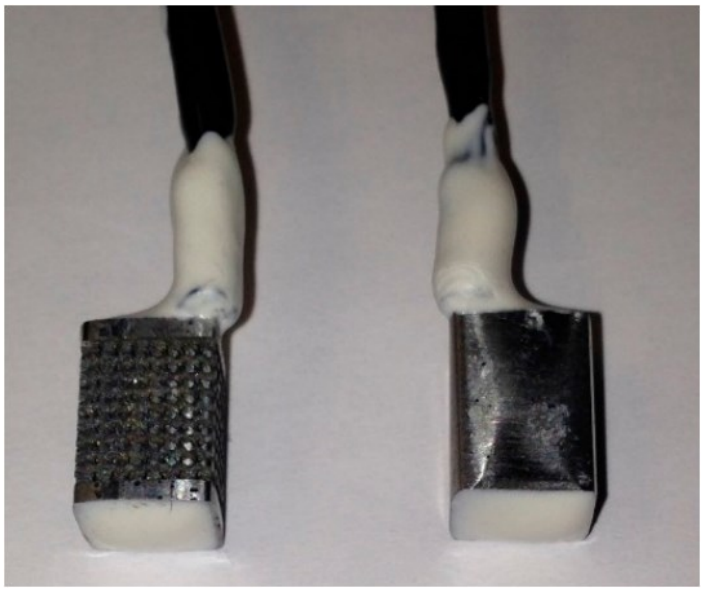

Figure 3-12 Samples prepared for the electrochemical corrosion test [15]

A Gamry Potentiostat (Gamry, Centennial, CO, USA) was used to perform the potentiodynamic polarization (PDP) test in the same SBF solution at pH 7.4, and at 37ºC. A constant scan rate of 1 mV/s from -250 to +1000 mV with respect to the open circuit potential (OCP) value was used. A standard three-electrode system with silver chloride

(Ag/AgCl) as the reference electrode, a graphite rod as the counter electrode, and the sample as the working electrode were used. The potential values obtained from the silver chloride reference electrode were converted to the standard calomel electrode (SCE) potentials. OCP of the samples was measured for the duration of 60 min to reach a stable state prior to the experiment. Eventually, Graphical Tafel analysis was used for measuring the corrosion characteristics such as current densities and corrosion potentials.

3.5.3 Surface Morphology

Surface morphology of the NiTi samples before and after corrosion test was evaluated via scanning electron microscopy (SEM). A Hitachi (Tokyo, Japan) s-4800 scanning electron microscope equipped with energy dispersive spectroscopy (EDS) analysis was used for the surface morphology. EDS analysis was used for surface assessment of the corrosion products.

Chapter 4

4. Results

In this chapter the results are presented and discussed in the following order. In the first section (4.1) computer simulation of the stiffness-matched skeletal fixation plates under realistic loading as well as calibration of the Abaqus UMAT, validation of the models, and simulation of the mechanical experiments are presented. The second section (4.2) is on the results of the fabrication. Mechanical evaluation of the fabricated samples is presented in the section three (4.3). Eventually, section 4 discusses the corrosion assessment of the additively manufactured skeletal fixation plates.

4.1 Modeling and simulation

In this section computer simulation of different models and components are presented. As it was mentioned earlier, an Abaqus UMAT is used for simulation of the NiTi components in this project. First this UMAT is calibrated and verified for modeling the NiTi components. After validating the NiTi UMAT, the healthy and reconstructed mandible models are simulated. Simulations of the reconstructed models are for two different stages; before and after healing. Since straight skeletal fixation plates were used for mechanical evaluations, these skeletal fixation plates were also used for modeling.

The goal is to predict and simulate the mechanical response of the stiffness matched skeletal fixation plates before any mechanical evaluation.

4.1.1 Calibration and validation of the Abaqus UMAT

As the first step to calibrate the UMAT, thermomechanical properties of the NiTi samples must be measured. Standard cubic samples were fabricated for thermomechanical characterization of the NiTi parts. DSC results, as shown in Figure 4-1, is used for obtaining the transformation temperatures. Mechanical compression test at body temperatures (37ºC) is used for measuring the modulus of elasticity in austenite and martensite phase. Since the material is in Austenitic phase before the plateau region (at the test temperature), Young's modulus for this region is attributed to the austenite phase, and Young's modulus right after the unloading is attributed to the martensitic phase (Figure 4-2). The summary of the calculated properties used for the calibration of the UMAT is shown in Table 4.1. A deflectometer is used to measure the displacement of the bottom grip. Strain is calculated via dividing the displacement over the initial length of the sample. We have only showed the stabilized stress-strain of the sample (i.e. After 10 cycle of loading and unloading).

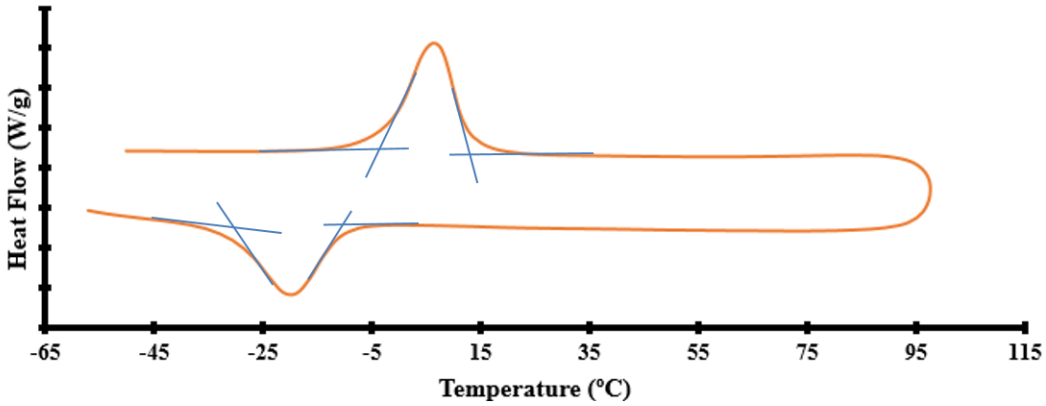

Figure 4-1 DSC result of the fabricated sample

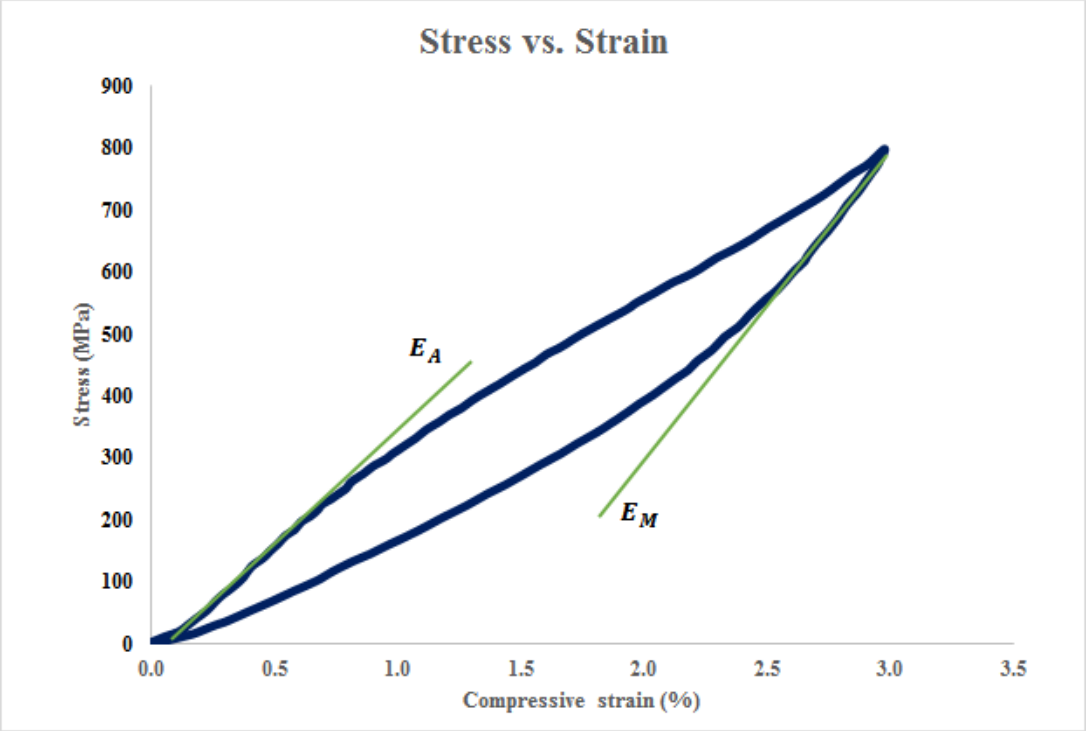

Figure 4-2 Stabilized stress-strain response of the fabricated coupon under compression

Table 4.1 Material properties of the fabricated sample used for calibration of the UMAT

Parameter	$E_A(GPa)$	$E_M(GPa)$	ν	$M_s(K)$	$M_f(K)$	$A_s(K)$	$A_f(K)$
Value	37	42	0.33	230	253	270	280

After obtaining the thermomechanical parameters, UMAT was used to simulate the compression test on the calibration sample. Figure 4-3 shows the experimental and simulation results of the compression tests of the calibration sample ($r > 0.99$, $p < 0.005$, root-mean-square error (RMSE) = 12.6 MPa and $r > 0.98$, $p < 0.005$, RMSE = 38.3 MPa for the simulation of loading and unloading responses, respectively).

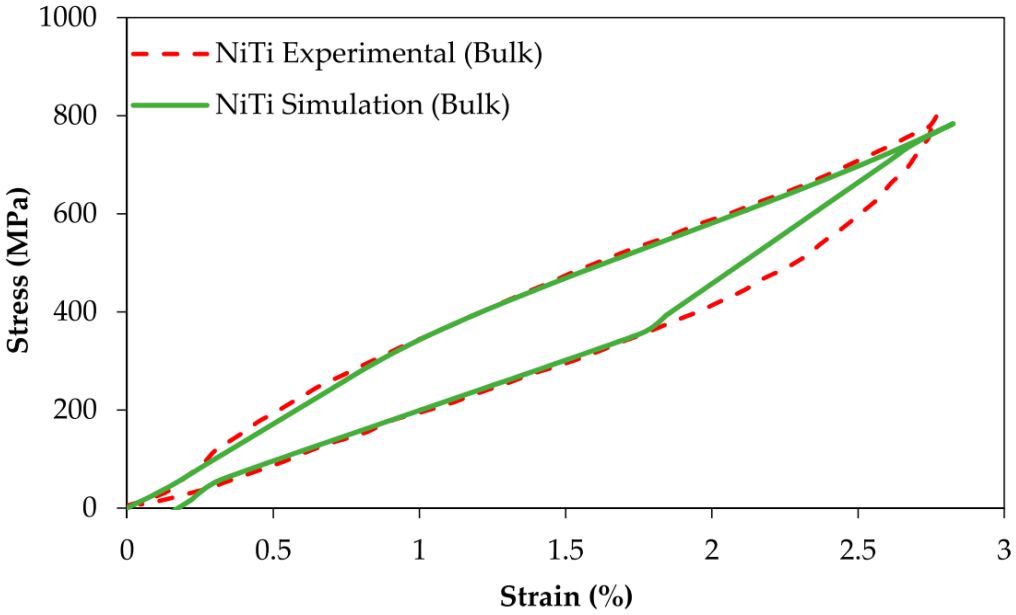

Figure 4-3 Simulation vs mechanical testing of the NiTi calibration coupon [15]

Using the procedure explained in the previous chapter, compression cubic samples with different levels of porosity were designed and modeled using the calibrated Abaqus UMAT. The unit cell for imposing the porosity is shown in Figure 4-4. The unit cell dimension was 1 mm and by changing the thickness of the lattice wires (d) the level of porosity was modulated. Equivalent stress for the porous compression samples was calculated by dividing the applied force by the overall cross-section of the compression cubes. Equivalent strain for the cubic porous samples was calculated by dividing the maximum displacement by the initial length of the cubic samples before the compression.

Figure 4-5 shows the equivalent stress vs. equivalent strain for the porous samples simulated by the calibrated UMAT.

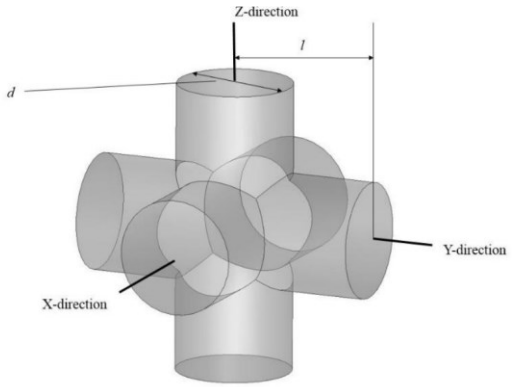

Figure 4-4 Unit cell of the pores [15]

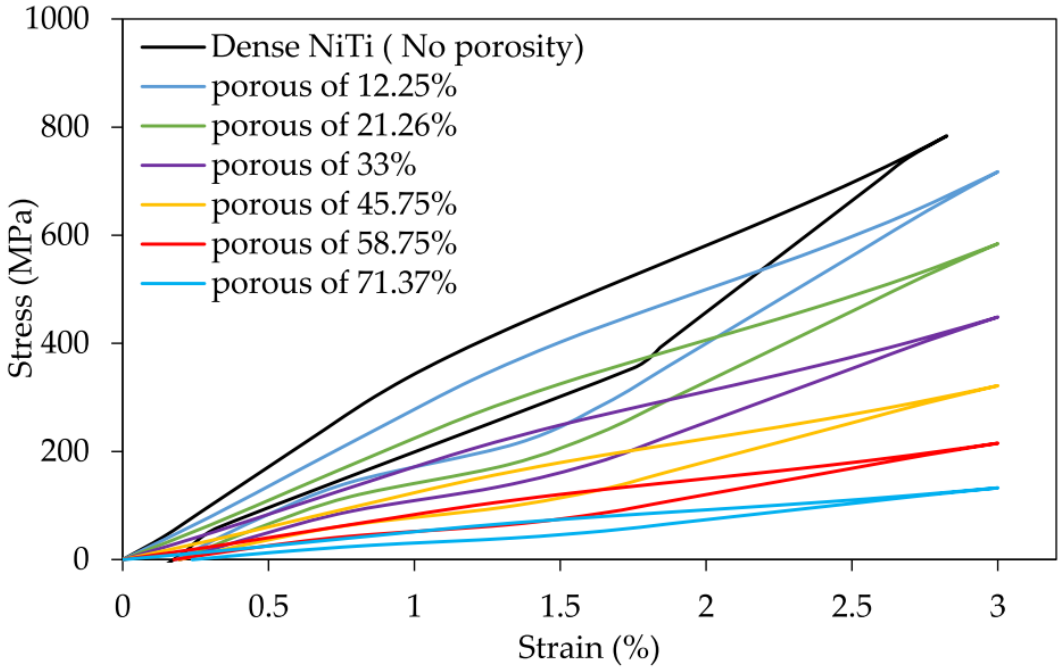

Figure 4-5 Equivalent stress vs. equivalent strain for the porous samples simulated by the calibrated UMAT [15]

The equivalent Young's modulus (here called as Young's modulus) can be calculated as the slope of the austenite region and is demonstrated in Figure 4-6. As it can be seen in this figure, by imposing 10 to 50 % porosity the equivalent stiffness of NiTi parts can be modulated to the levels of cortical and even cancellous bone (the gray

region). However, in order to reduce the equivalent stiffness of the Ti-6Al-4V parts more than 50 % and up to 90 % porosity is required. Higher levels of porosity lead to higher levels of local stress concentration cause early failure of the material. In addition, the superelastic property of NiTi prevents failure of the porous structures, for local strains up to 6 % under compression [239].

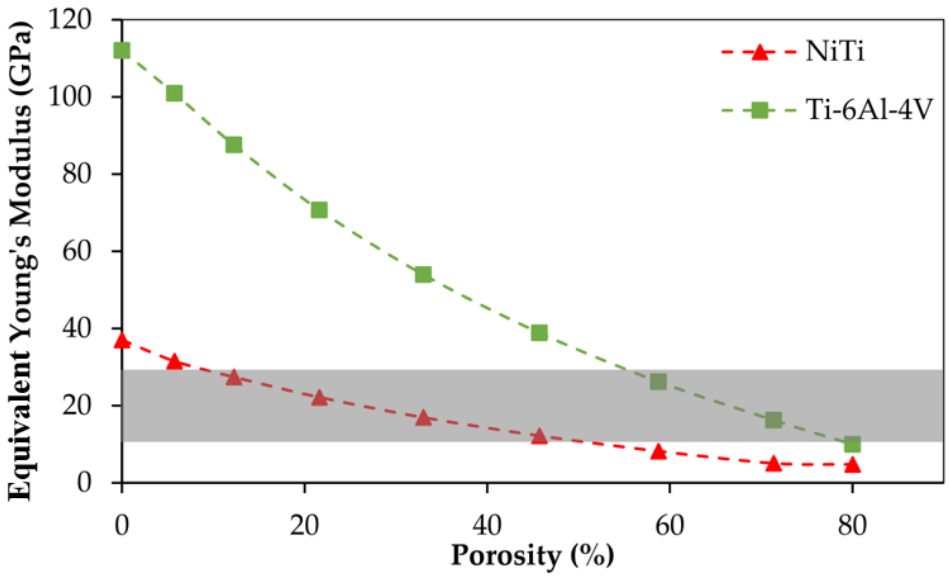

Figure 4-6 Equivalent Young's modulus of the porous samples [15]

4.1.2 Validation of the mandible model

Before modeling the healthy and reconstructed mandibles, the created mandible model must be validated. To this end, an experimental study by Ichim *et al.* [15] is used as the reference. They have used a dried cadaveric mandible and applied a specific loading while measuring the buccal and lingual strains on the cortical bone using strain gauges. We applied the same loading condition in our mandible model and calculated the strain values at the same locations as the reference work. Figure 4-7 shows the experimental measurements by Ichim *et al.* as well as simulated strain levels using our finite element model. As it can be seen in this figure, our FE model can be verified by

this experimental study ($r > 0.99$, $p < 0.0005$, RMSE = 2.8×10^{-6} (%) and $r > 0.99$, $p < 0.0005$, RMSE < 6.42×10^{-6} (%) for the Buccal and Lingual sides of mandible cortical bone in the molar region, respectively).

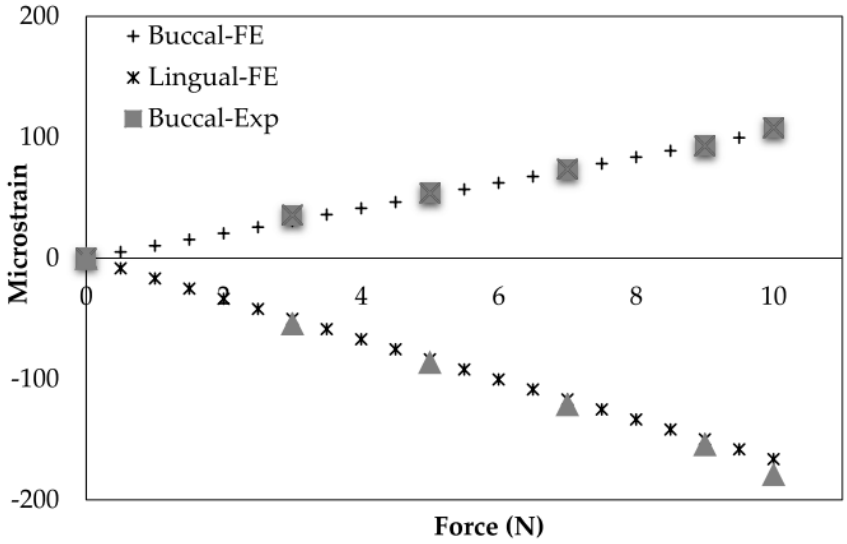

Figure 4-7 Model validation: a comparison between experimentally obtained data (EXP) with FEA-predicted model data on the buccally and lingually placed strain gauges. [15]

4.1.3 Required level of porosity

Based on the material properties of the mandible model obtained from the CT scan data, Young's modulus of the surrounding cortical bone on our mandible model was measured as 12 GPa. Using the plot shown in Figure 4-6, the required level of porosity for adjusting the level of stiffness for the NiTi skeletal fixation plates was calculated as 45.7 %. This level of porosity and equivalent Young's modulus were considered for the design of the stiffness matched skeletal fixation plates in our case. Figure 4-8 shows the simulated equivalent stress-strain response of a NiTi sample with 45.7 % porosity similar to what we considered for the skeletal fixation plates. The figure also demonstrates the stress-strain response of a cortical bone and a standard Ti-6Al-4V from the literature for

the comparison purposes. As it can be seen in this plot, while the stiffness matched NiTi component closely mimics the mechanical response of the bone tissue, there is a significant difference in the level of stiffness between the Ti64 and the bone tissue.

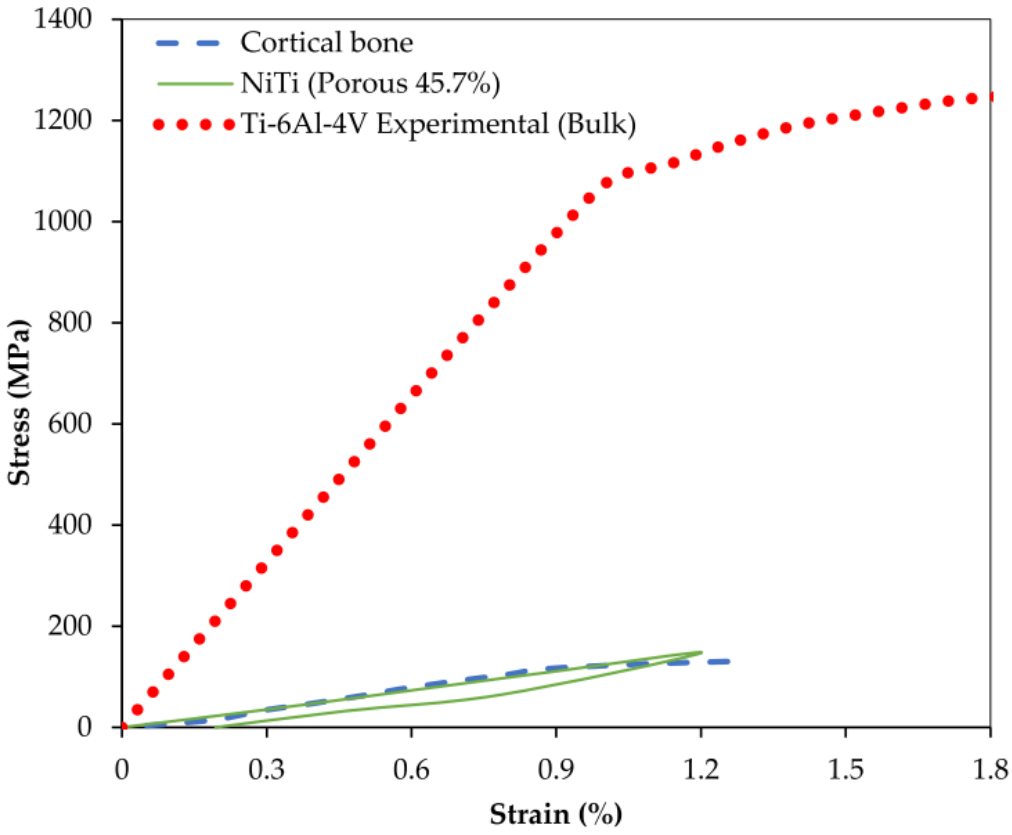

Figure 4-8 The equivalent stress-strain plot under compression for NiTi cubic samples with 45.7% porosity, cubes of dense Ti-6Al-4V and samples of mandibular cortical bone [15]

4.1.4 Simulation of the healthy and reconstructed mandible

By calibrating and verifying the Abaqus UMAT for modeling the NiTi components and modulating the level of porosity for the bone fixation plates, we are able to model the case of reconstruction surgery with conventional skeletal fixation plates as well as the NiTi stiffness matched options. We have modeled the reconstructed mandibles before and after the bone healing period. Immediately after the surgery, when

the bone graft and the host mandible are not still healed, the major portion of the loads are carried out by the skeletal fixation plates. At this stage, it is important to provide enough immobilization between the skeletal fixation graft and the host mandible to facilitate and expedite the bone healing. On the other hand, when the bones heal, stress distribution on the cortical bone is of great interest. Therefore, we have simulated the reconstructed mandible before and after the healing.

4.1.5 Reconstructed mandibles before healing

Immediately after the surgery, when the bones still have not healed, the skeletal fixation plates tolerate the major portion of the loads and it is important to provide enough immobilization for the bone graft. Graft unvascularizarization is counted as one of the reasons for the early failure of the reconstructive surgery and is often caused by poor immobilization due to the decreased contact pressure between the graft and the host bone. Therefore, the contact pressure between the host bone and the bone graft could be a good representative of the immobilization level. We have simulated the case of reconstruction before the bone healing and measured the contact pressure between the bone pieces. It is also possible to apply some levels of pre-tension on the skeletal fixation plates to increase the contact pressure. We have considered a 100 N pre-tension force applied to both type of the skeletal fixation plates. Due to the muscle forces and the dynamic of the mandible, the bottom portion is naturally under compression. However, the stiffer Ti64 skeletal fixation plates reduce the natural contact pressure at the bottom portion, while the low stiff NiTi plates have the minimum effect. The contact pressure has been calculated for the two different loading scenarios, a) when the mandible is at rest and the pre-tension is the major load, and b) when the maximum bite force is applied

to the mandible. Figure 4-9 shows the average contact pressure for the two different cases.

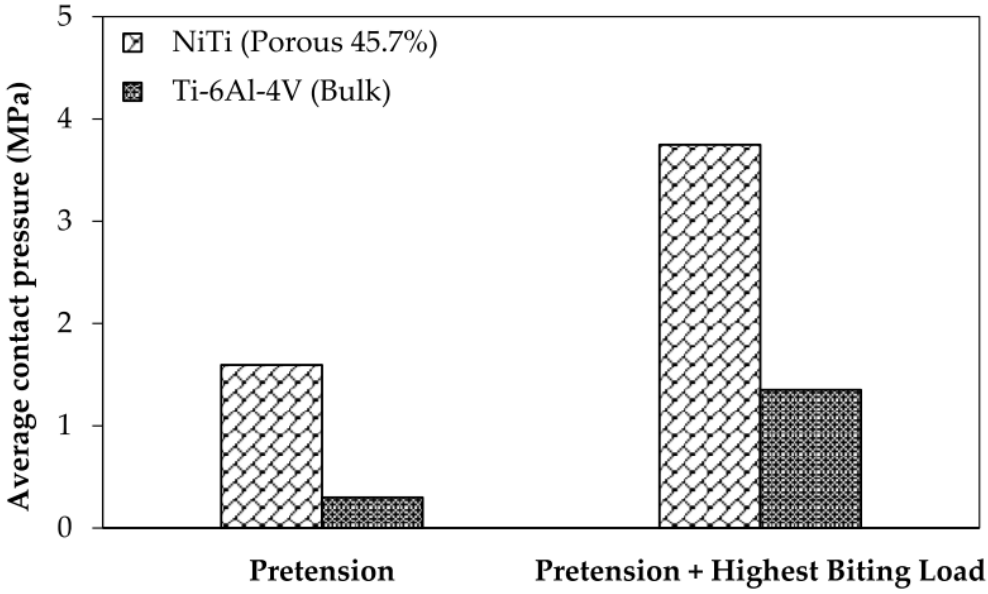

Figure 4-9 The effect of using NiTi and Ti-6Al-4V fixation plates on the average contact pressure at the interface between the graft and host bone (i.e., fibular bone graft and host mandible) during the healing period (i.e., in the immediate postoperative period [15]

4.1.6 Reconstructed mandibles after healing

As it was mentioned earlier, when the bones heal, stress shielding is one of the main reasons for bone resorption and failure of the reconstructed mandible. In order to study the stress shielding and stress concentration on the mandible and the hardware, the von Mises stress distribution is evaluated. The average values of the von Mises stress on the surrounding bone are used for the comparison of different cases and the maximum von Mises stress is reported for the safety assessment.

A healthy mandible (with no reconstruction) is modeled and used as the reference. For the reconstructed mandibles, three different loading scenarios were considered. Case 1: when the mandible is under maximum bite force, case 2: when the mandible is at rest

and pre-tension force is the major loading applied to the mandible, and case 3: when the mandible is under maximum bite force and still there is pre-tension in the skeletal fixation plates. Each case was simulated using the conventional and stiffness-matched skeletal fixation plates.

Figure 4-10 shows the average von Mises stress for both types of skeletal fixation plates under different loading conditions. In comparison with the traditional skeletal fixation plates, the results showed higher average von Mises stresses on the cortical bone of the bone grafts in the case of stiffness matched NiTi skeletal fixation plates in all loading scenarios. In addition, the average stress on the on the bone graft in the case of stiffness matched skeletal fixation plates was closer to the healthy mandible (showed by the dashed line). The healthy mandible was simulated under maximum bite force.

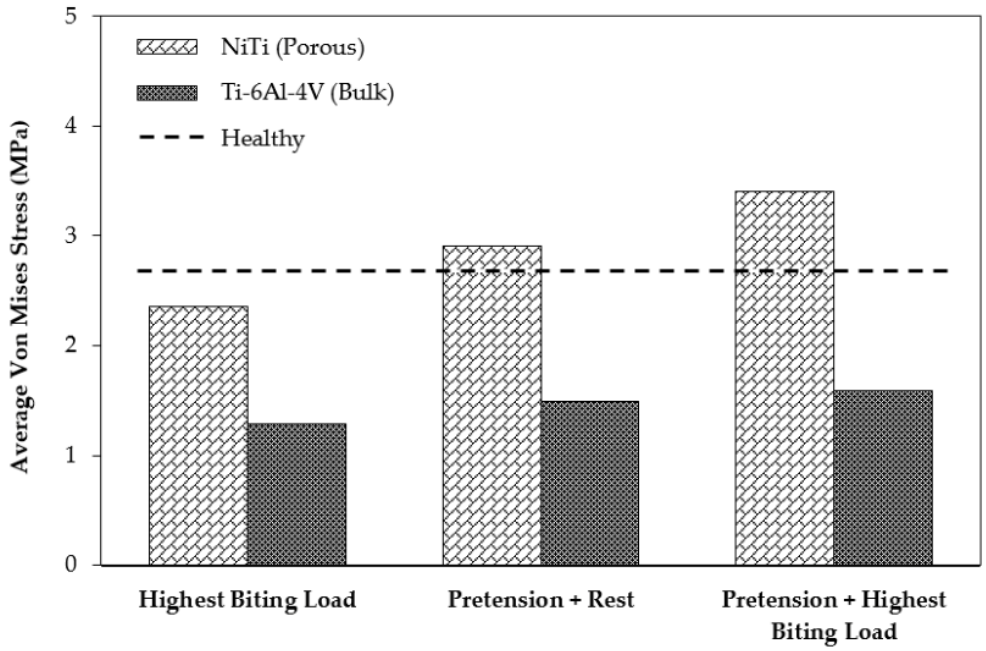

Figure 4-10 The average Von Mises stress on the surrounding bone in two cases of using Ti-6Al-4V and porous NiTi fixation plates, with and without applying the pretension to the fixation plates. [15]

Figure 4-11 shows the maximum von Mises stress on the surrounding cortical bone for the same three different loading conditions. Similar to the results of the average stress distribution, the maximum stress for the case of stiffness matched skeletal fixation plates is higher than the conventional skeletal fixation plates (Ti-6Al-4V). More importantly, all the stress levels are in the safe zone for cortical bone (<100 MPa). Based on these simulations, one may conclude stiffness matched porous superelastic NiTi skeletal fixation plates increase the von Mises stress on the bone graft and therefore reduce the stress shielding effect and the risk of the implant failure.

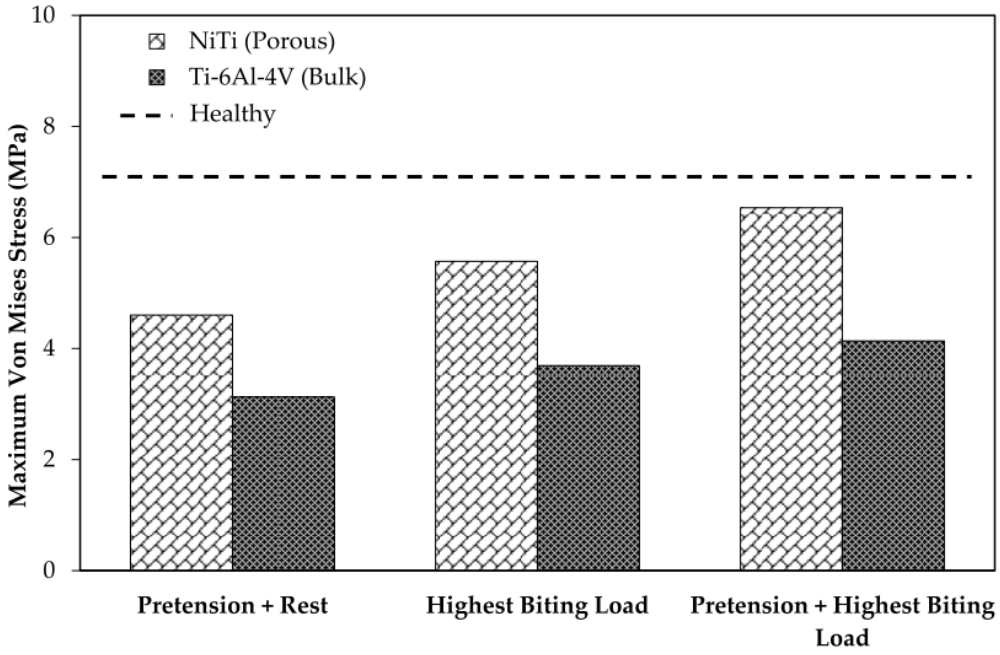

Figure 4-11 The maximum von Mises stress on the surrounding bone in two cases of using Ti-6Al-4V and porous NiTi fixation plates [9]

4.1.7 Simulation of the plate with actual porosity

Standard-shape skeletal fixation plates were used for mechanical evaluation of the stiffness matched skeletal fixation plates. Due to the limitation of the available SLM machine (Phenix PXM) which was not able to print feature sizes finer than 450 microns, we had to modify the porous skeletal fixation plates in a way that can be fabricated via our machine. As it was mentioned earlier, the unit pore cell geometry was made of three perpendicular struts in x, y, and z directions. In order to prevent stress shielding at the corners, some fillets and more details were added to each pore cells as is can be seen in Figure 4-12.a. The volume created by this pore cell can be seen in Figure 4-12.b.

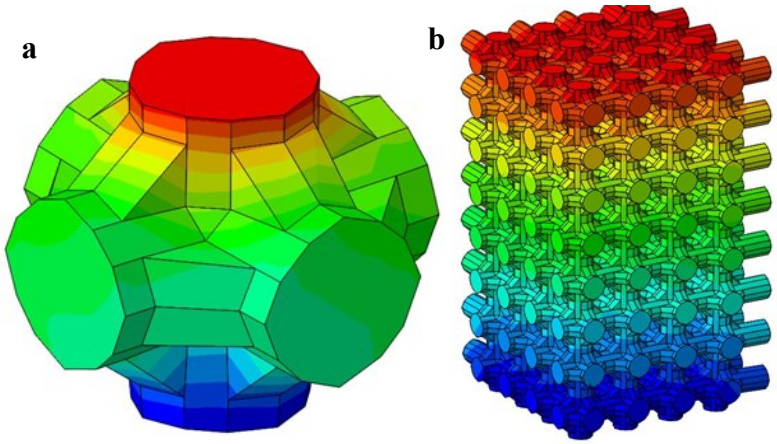

Figure 4-12 Modified pore shape used for the skeletal fixation plates, (a) a single pore cell, (b) a block made by the reference pore cell

This pore geometry was assigned to the standard skeletal fixation plate shown in Figure 4-13. The selected skeletal fixation plate was 30 mm long, 3 mm thick and with other geometrical details as can be seen in Figure 4-13. In addition to imposing the porosity to the skeletal fixation plate geometry, a thin surface was added to the top and side sections of the porous skeletal fixation plate. This thin surface works as a support for the screws and provides additional strength to the skeletal fixation plate. The thinnest possible shell that could be fabricated was 450 μm. Figure 4-14 shows top and bottom views of one of the porous skeletal fixation plates before and after adding the thin cover to that.

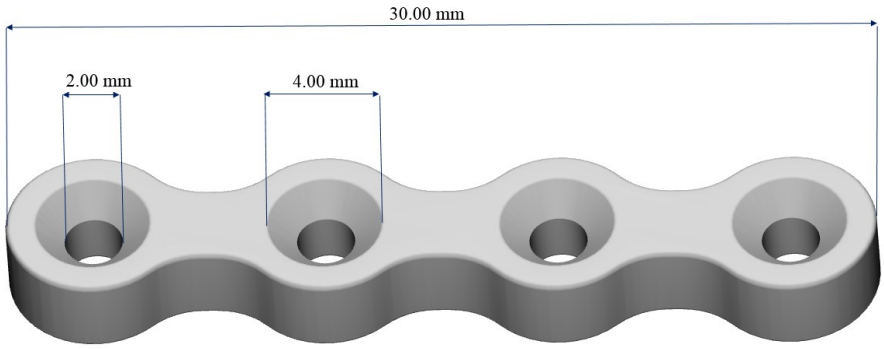

Figure 4-13 Shape and dimension of the standard skeletal fixation plate used for mechanical testing

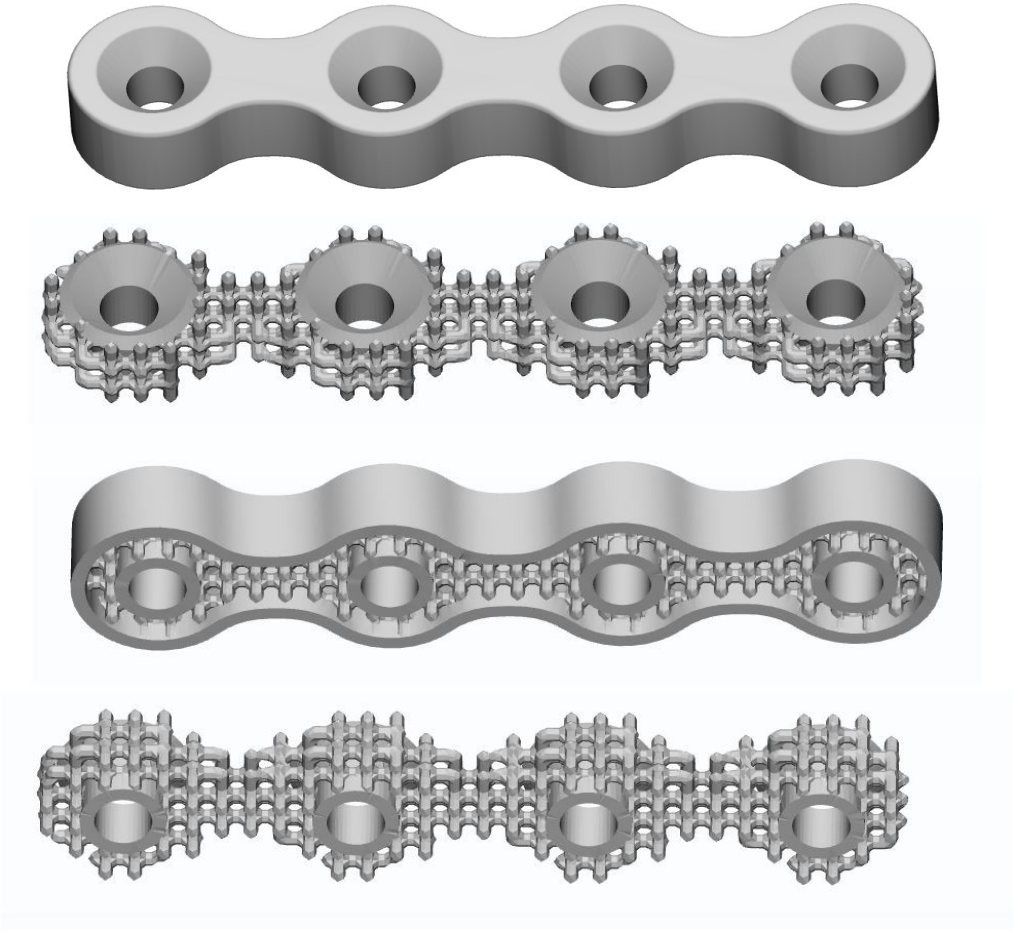

Figure 4-14 Top and bottom views of a sample porous skeletal fixation plates before and after adding a thin cover

In order to verify the stiffness matching feature, the tensile test of these skeletal fixation plates was simulated using the calibrated UMAT. The goal was to show the

possibility of designing the stiffness matched skeletal fixation plates using additive manufacturing. Material properties for the available powder were measured as discussed in the previous section and eventually, load displacement for the skeletal fixation plates was plotted (Figure 4-16). Figure 4-15 is a representative of the simulated skeletal fixation plated while Figure y shows the load versus displacement.

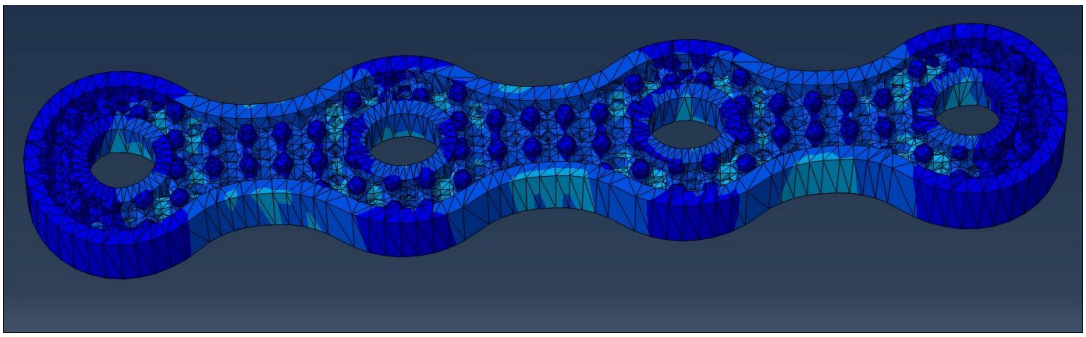

Figure 4-15 A representative of the simulated skeletal fixation plates

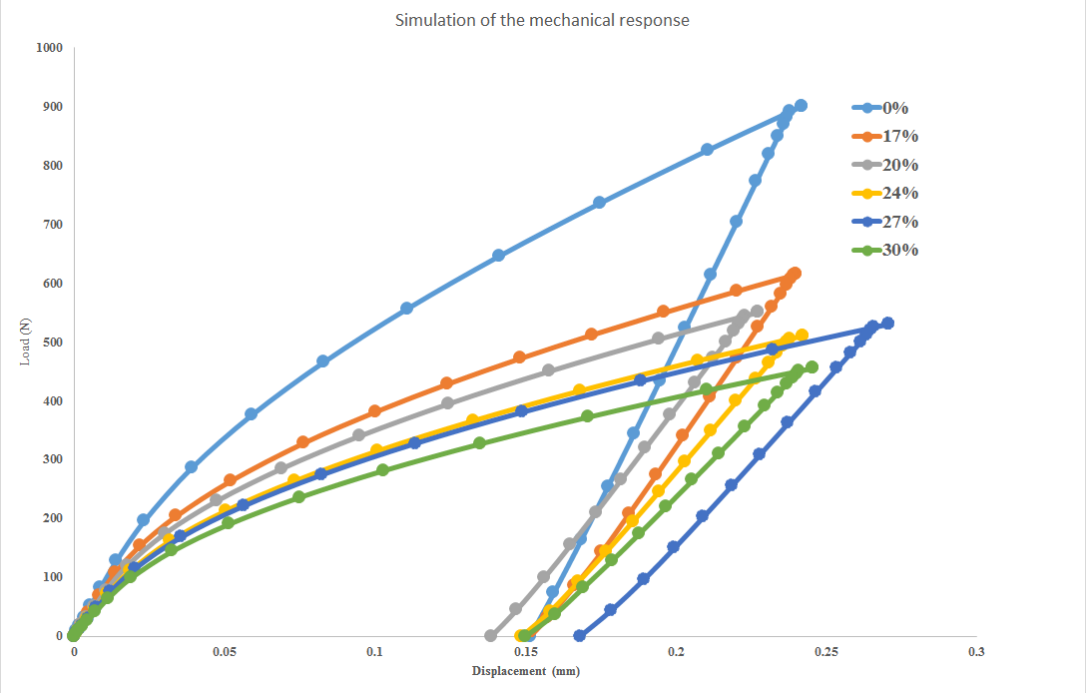

Figure 4-16 Simulated load-displacement plot for the designed skeletal fixation plates

As it can be seen in Figure 4-16, the stiffness of the porous skeletal fixation plates can be modulated and reduced up to 50 % (~15 GPa) in this case. The main limitation in

the design of the porous stiffness matched skeletal fixation plate was the resolution of the AM machine. As the next step in verifying the whole design procedure, these skeletal fixation plates were fabricated and mechanically tested.

4.2 Fabrication of the standard skeletal fixation plates with different levels of porosity

After successful design and simulation of the stiffness matched skeletal fixation plates, different samples and skeletal fixation plates were chosen for the SLM fabrication. The fabrication had several goals and based on that different parts were fabricated. The first set of components which were fabricated were the patient-specific skeletal fixation plates designed based on the CT scan data of our reference dried mandible. These skeletal fixation plates followed the outer geometry of the mandible bone and could be installed on the dried mandible with no further post-deformation. Figure 4-17 shows the stiffness matched skeletal fixation plates attached on the referenced dried mandible.

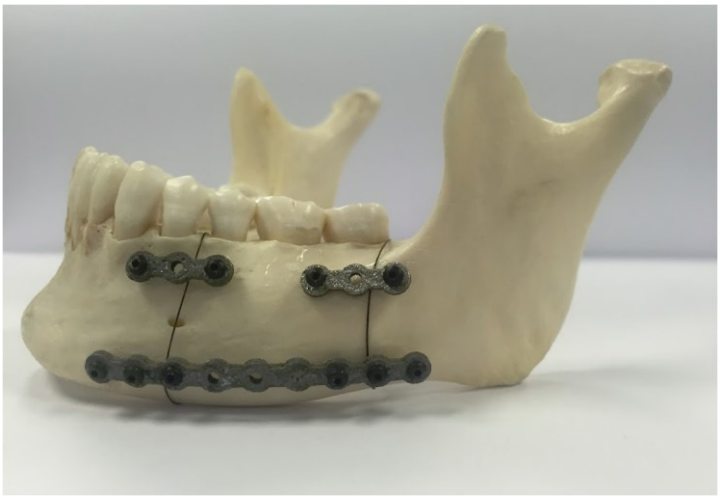

Figure 4-17 Stiffness matched skeletal fixation plates attached to the referenced dried mandible [9]

In order to evaluate the mechanical response of the stiffness matched skeletal fixation plates, porous standard-shaped NiTi skeletal fixation plates were fabricated. Due to the complex geometry of the porous skeletal fixation plates, these samples were directly built on the substrate and then were removed via EDM. In order to evaluate the internal pore quality of the porous skeletal fixation plates, besides each skeletal fixation plate its internal lattice structure was also fabricated. Figure 4-18 shows some of these porous skeletal fixation plates and their internal lattice structure. Due to the proper selection of the minimum printable feature all these skeletal fixation plates were successfully fabricated. These skeletal fixation plates were then used for mechanical evaluations and verifying the finite element simulations.

Figure 4-18 Fabricated porous skeletal fixation plates for the mechanical evaluation

The next set of samples were fabricated for corrosion assessments which is a major step toward biocompatibility of the additively manufactured skeletal fixation plates. Although the ideal case is to use the original skeletal fixation plates for the corrosion assessment, due to the complex geometry of the skeletal fixation plates, having no control over the surface area, and more importantly limitation of the testing equipment, standard samples were needed for this study. Therefore, 9 mm cubic samples with the same level and type of porosity as the porous skeletal fixation plates were fabricated for immersion and electrochemical corrosion assessment. Similar to the skeletal fixation plates, EDM was used for removing the corrosion samples from the build plate. Fabricates samples are shown in Figure 4-19.

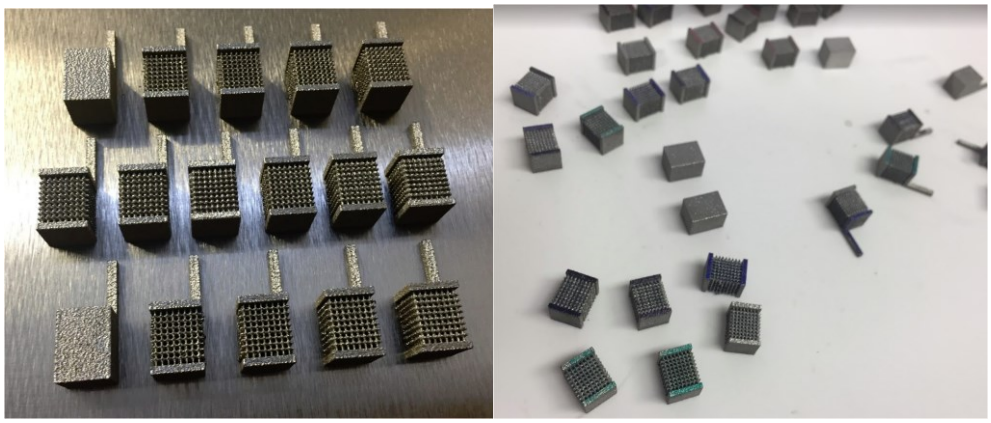

Figure 4-19 Fabricated samples for immersion and electrochemical test

4.3 Mechanical evaluation of the fabricated skeletal fixation plates

In order to eliminate the effect of screws in evaluating the skeletal fixation plates, the grippers shown in Figure 4-20 were used. The samples were tested as fabricated with no heat treatment or any other post-treatment. For the tensile test, the samples were loaded in the displacement control mode with the equivalent strain rate of 10e-4 mm/mm. Samples were stretched to 0.35 mm based the Electroforce Bose machine. After loading, samples were unloaded using the load control mode up to 0 N. A video extensometer was used for recording the displacement on the samples. For each sample, three red dots were added as can be seen in Figure 4-20 to be tracked by the camera. The load-displacement response with respect to the displacement reported by the mechanical testing machine and the extensometer is shown in Figure 4-21 for the dense skeletal fixation plate. The red dots were marked at the exact same location for each skeletal fixation plate and the relative displacement between the upper and lower red dot was reported for all the skeletal fixation plates (The yellow plot in Figure 4-21).

Figure 4-20 Mechanical setup used for the tensile test (Gripper, video extensometer, and a failed sample)

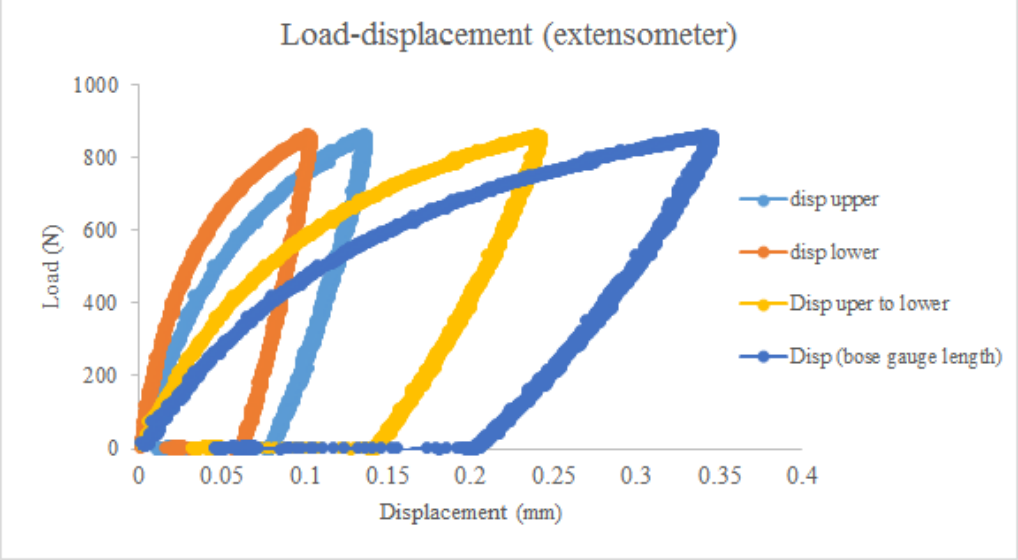

Figure 4-21 Load-displacement of the samples obtained from the testing machine and the video extensometer

Figure 4-22 shows the load-displacement plot for the fabricated skeletal fixation plates using the displacement measured by the extensometer. As it can be seen, similar to what was predicted using the finite element simulation, the stiffness of the fabricated skeletal fixation plates is reduced up to 50 % for the one with 27 and 30 % porosity. The results of the simulated skeletal fixation plates were then compared with the skeletal fixation plates as shown in Figure 4-23 to Figure 4-28.

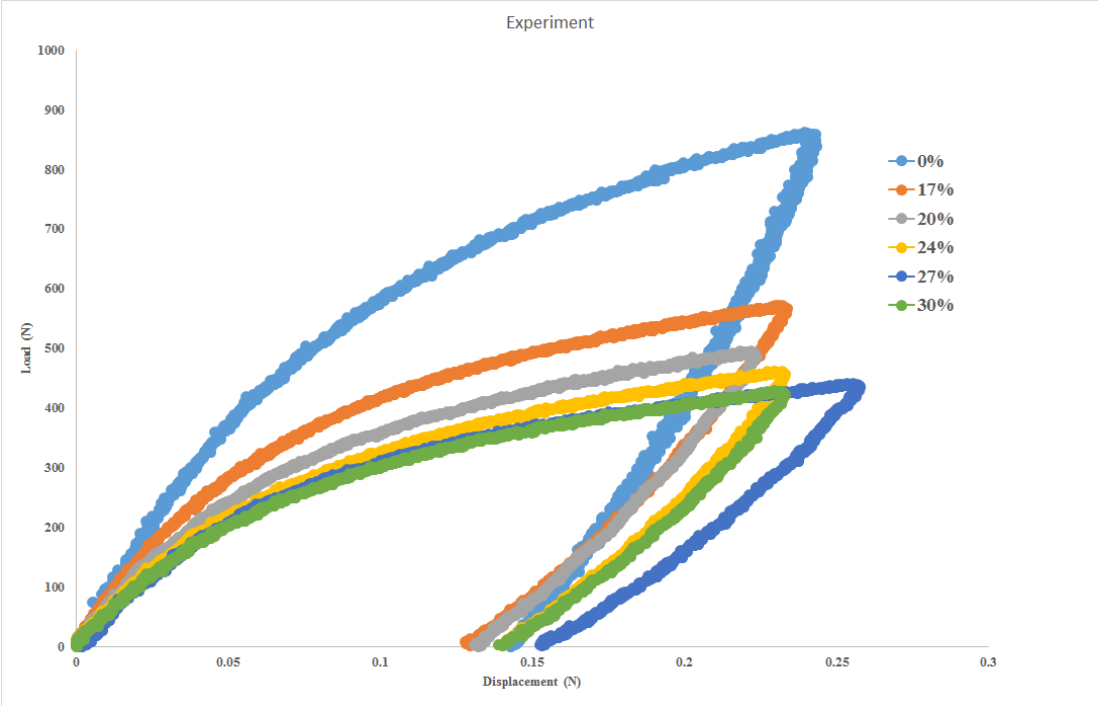

Figure 4-22 Load displacement plot for the fabricated skeletal fixation plates using the displacement measured by the extensometer

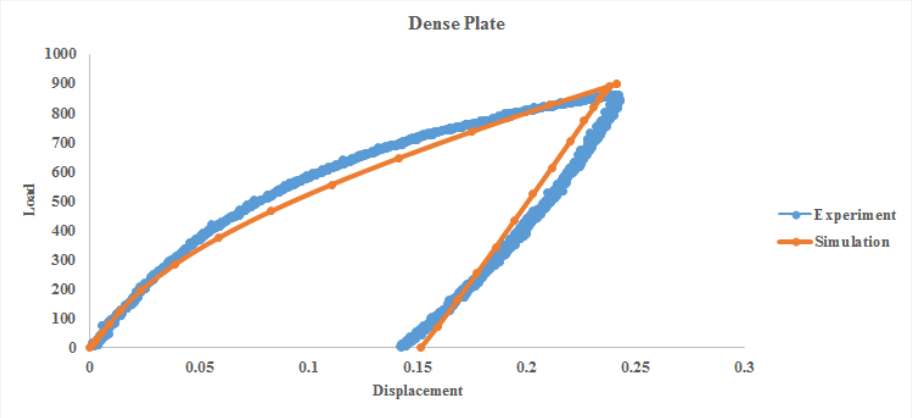

Figure 4-23 Comparison of the simulation and mechanical testing for the dense skeletal fixation plate

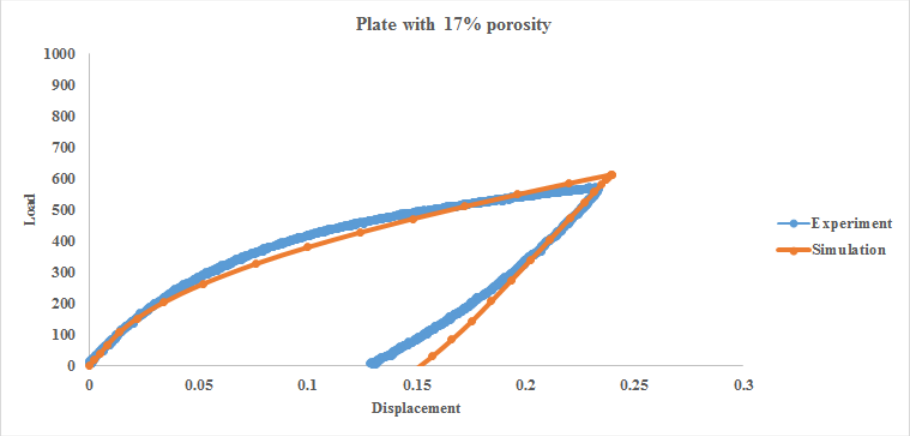

Figure 4-24 Comparison of the simulation and mechanical testing for the porous skeletal fixation plates with 17% porosity

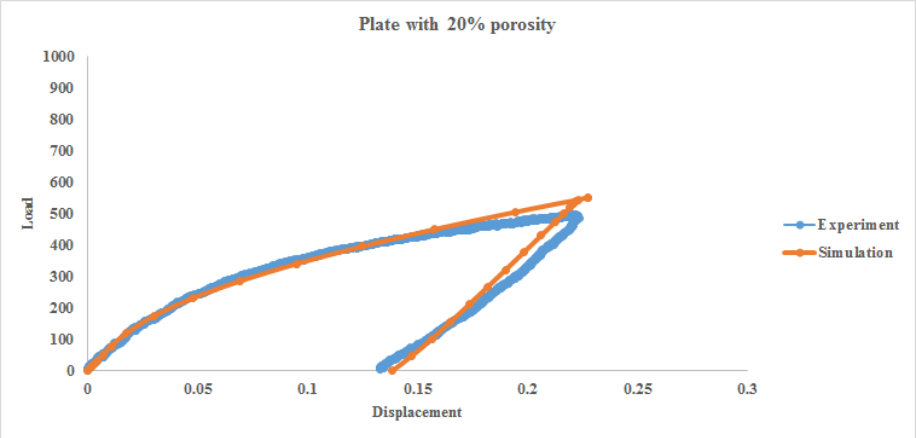

Figure 4-25 Comparison of the simulation and mechanical testing for the porous skeletal fixation plates with 20% porosity

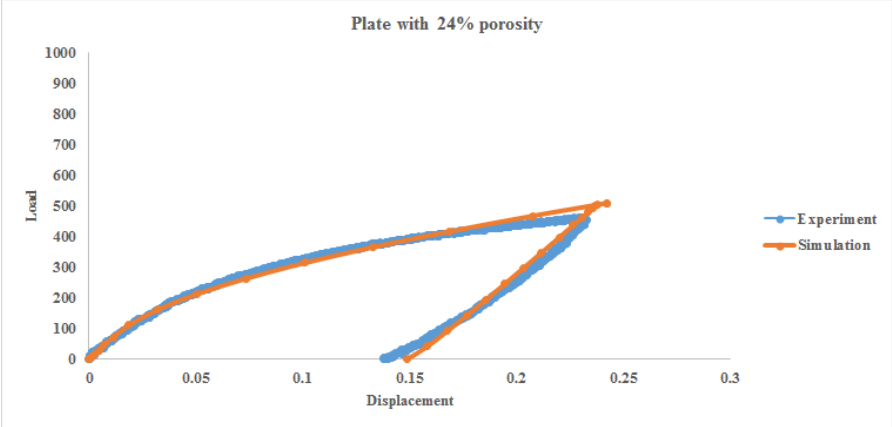

Figure 4-26 Comparison of the simulation and mechanical testing for the porous skeletal fixation plates with 24% porosity

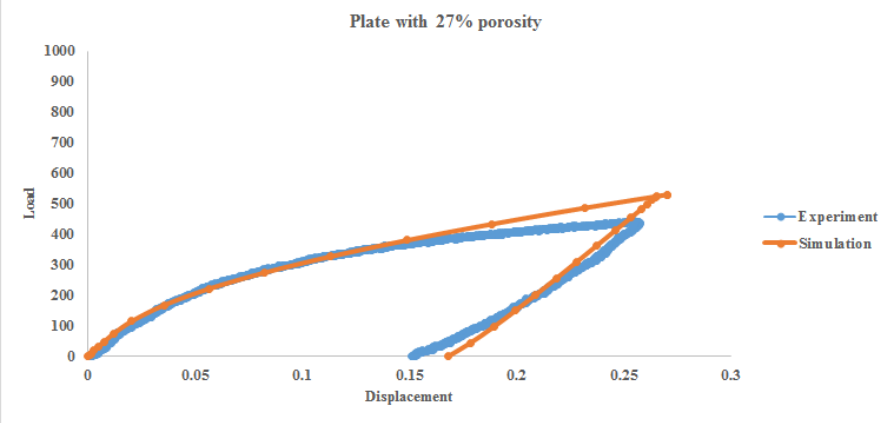

Figure 4-27 Comparison of the simulation and mechanical testing for the porous skeletal fixation plates with 27% porosity

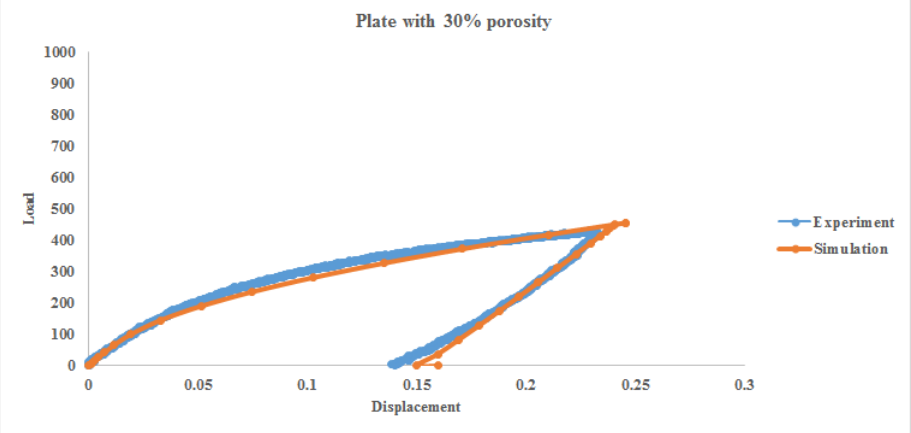

Figure 4-28 Comparison of the simulation and mechanical testing for the porous skeletal fixation plates with 30% porosity

4.4 Corrosion assessment

4.4.1 Electrochemical corrosion test

As the first step to evaluate the biocompatibility and corrosion resistance of the additively manufactured NiTi in human body electrochemical test was performed on the porous and bulk AM NiTi. The results were also compared with a bulk conventionally fabricated sample. Figure 4-29 shows the Tafel curves of the conventionally fabricated NiTi sample and the additively manufactured NiTi. Based on this result summarized in Table 4.2, the additively manufactured NiTi sample showed corrosion characteristics comparable to those for the conventionally fabricated samples. Similar corrosion characteristics of the additively manufactured and conventionally fabricated NiTi samples imply homogenization in the microstructure and the absence of apparent defects for the AM NiTi parts that could deteriorate the corrosion properties. Although the Tafel curves show a slightly higher corrosion current density for the AM NiTi sample, such a small difference is within the acceptable range and indicates that the additive manufacturing process does significantly change the corrosion characteristics of NiTi.

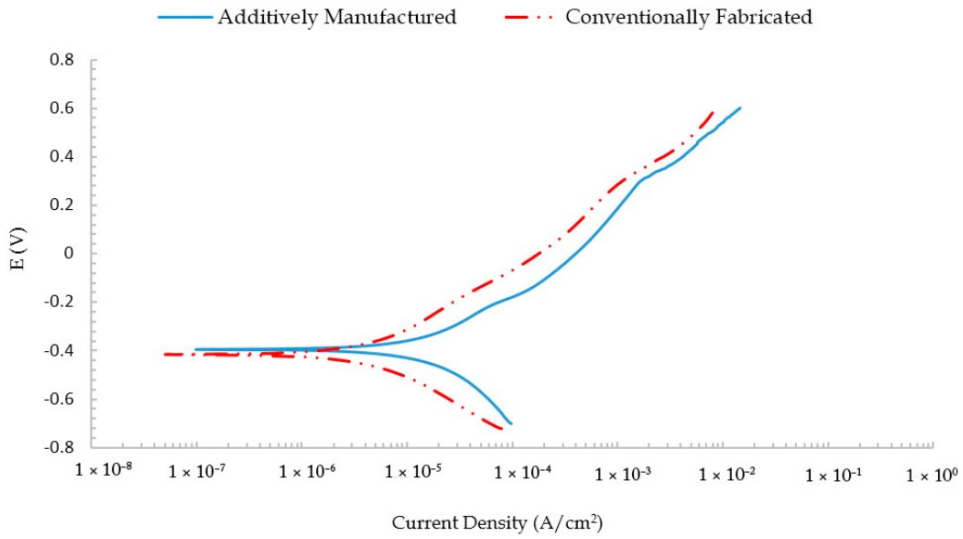

Figure 4-29 The potentiodynamic polarization curves of the conventionally fabricated and additively manufactured NiTi alloy samples [9]

Table 4.2 Electrochemical corrosio carachtaristics for AM and conventionally fabricated NiTi

Sample	Current density ($\mu A/cm^2$)	Corrosion potential (V)
AM NiTi	20 ± 2.1	−0.394 ± 0.01 V
Conventionally fab. NiTi	12 ± 3.8	−0.4155 ± 0.008

Figure 4-30 shows the Tafel curves of two structures with the same volume produced by additive manufacturing: bulk structure and porous structure (35% porosity level). As expected, the higher surface area and the presence of many edges in the case of the porous structures resulted in a higher corrosion current. For instance, the corrosion current increased from about 200 nA for a bulk structure to be 950 nA for a 35% porous structure. This increase in the corrosion currents is expected to result in more corrosion byproducts and a higher amount of Ni ion released *in vivo*.

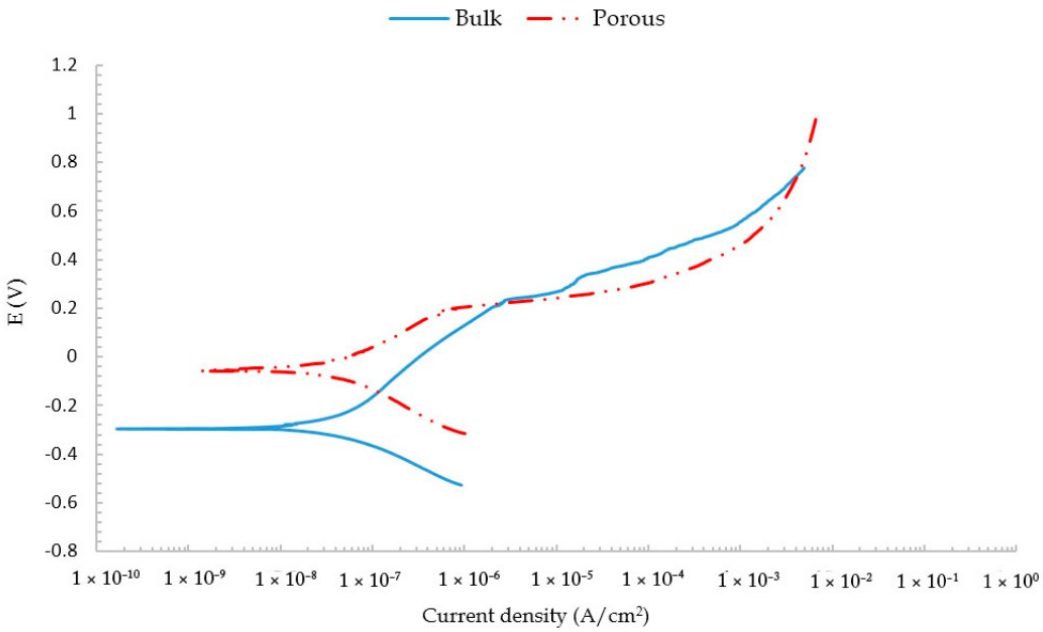

Figure 4-30 The potentiodynamic polarization curves of the AM NiTi alloys with two different structures; bulk and 30% porous structure [9]

4.4.2 Surface Morphology

SEM and EDS analysis were used for assessment of the surfaces of the AM NiTi samples after the in-vitro potentiodynamic polarization test. As it can be seen in Figure 4-31, the surface of the parts showed several pits with corrosion products agglomerations on it. This observation assures the occurrence of pitting corrosion for the parts. These pits were circular, with a diameter between 50 to 250 μm. Based on the EDS elemental analysis of the corrosion products on the surface of the samples (point 1) (concentrated inside and around the pits), sodium, phosphorus and sulfur-based compounds alongside oxygen, Ti, and Ni are the main components. The elemental analysis of the regions away from from the pits (point 2) showed no traces of sodium, phosphorus, or sulfur. The presence of oxygen on the surface implies the existence of oxide layers after the corrosion test.

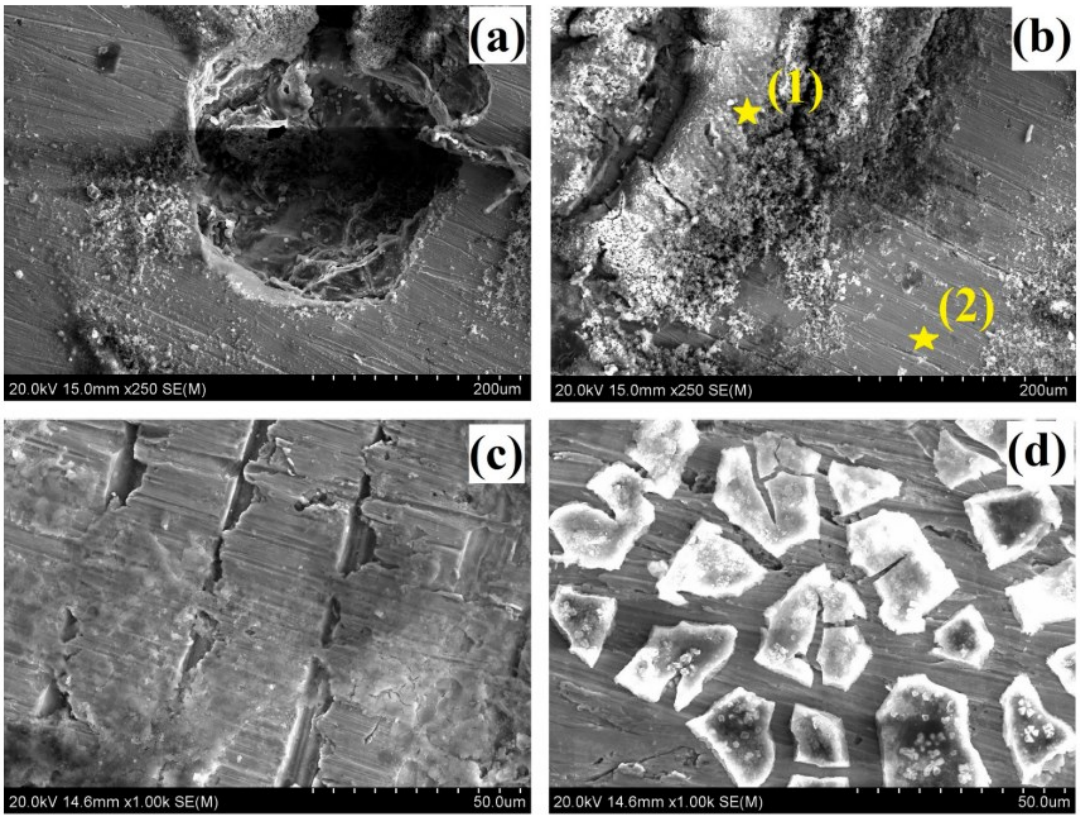

Point	Element Wt.%								
	O	Na	P	S	Cl	K	Ca	Ti	Ni
1	30.4	4.96	1.65	10.39	7.85	1.53	1.53	32.0	8.69
2	10.25	0.0	0.0	0.0	0.0	0.0	0.0	41.56	48.19

Figure 4-31 SEM investigation and EDS point spectrum analysis of the corroded surface after the potentiodynamic polarization test in SBF at 7.4 pH and 37 ◦C, (a,b) show the pits with corrosion product agglomerations at 250× magnification; (c,d) show the corroded surface at 1000× magnification [9]

4.4.3 Ni Ion release by immersion test

The results of the Ni ion release after the immersion test in particles per billion can be seen in Figure 4-32. The results verify that the amount of Ni ion released of the AM NiTi samples is similar to that of conventionally fabricated NiTi. However, the

porous AM NiTi samples due to the higher surface area showed higher amounts of Ni ion release which also confirms the electrochemical corrosion test results. For instance, imposing 25 % porosity to the samples increased the surface area exposed to the SBF solution from 594 mm^2 to 1997.5 mm^2 which led to an increase in the amount of Ni ion release from 64 ppb for bulk samples to 176.35 ppb (Table 4.3). These results indicate that the both AM NiTi and conventionally fabricated NiTi release a same level of Ni ions which is a function of the surface area. One could conclude that a limitation of using porous NiTi as an implant is the increased level of Ni ion release that must be carefully considered based on the actual surface area of the part. However, different surface treatments, such as passivation, coating or chemical treatment can be used to reduce the Ni ion release of the AM NiTi parts similar to the same methods used for the conventionally fabricated NiTi.

Table 4.3 The surface area and Ni ion release measurements for the conventionally fabricated and additively manufactured NiTi samples (bulk and porous) [9]

Sample Type	Surface Area (mm^2)	Ni Ions (ppb)
Conventionally-fabricated	590	59.45
AM (dense)	594	64
AM (15% porosity)	1620.3	127.94
AM (25% porosity)	1997.5	176.35
AM (35% porosity)	2106.6	194.3
AM (50% porosity)	2116.3	196.8

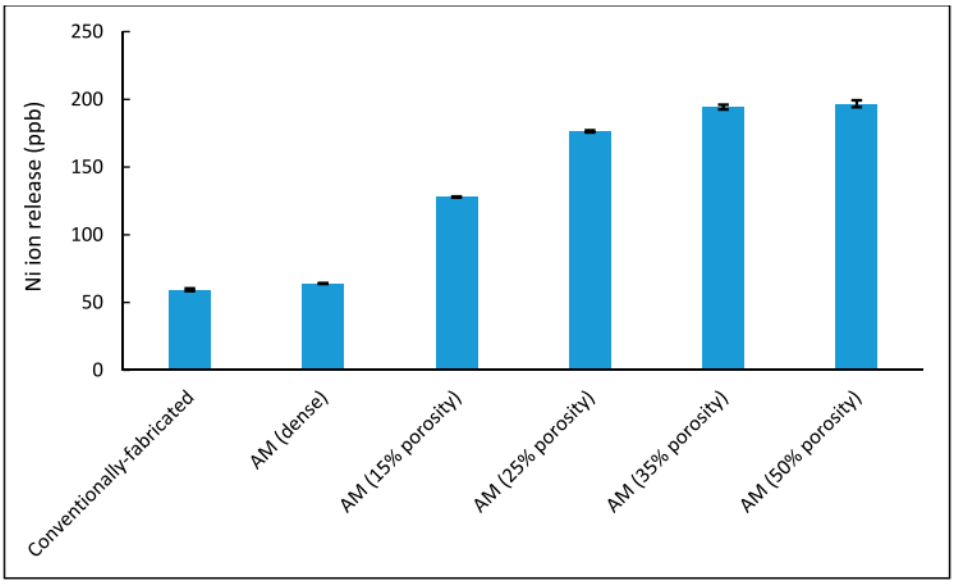

Figure 4-32 The Ni ion release of two different structures (dense and porous) of additively manufactured NiTi alloys in comparison to the conventionally fabricated NiTi alloy [9]

4.5 Superelastic Stiffness-Modulated Bone Fixation Plates[1]

In order to investigate the superelastic response of bone fixation plates, only bone fixation plates with the most complex geometry (minimum thickness = 1.5 mm) and an extreme level of porosity (i.e., 46%) was considered. To create a realistic geometry for the bone fixation plate, a 4-hole 1.5 mm thick bone fixation plate as shown in Figure 4-33.a was provided by Stryker (Kalamazoo, MI, USA). The plate was then scanned using a micro computed tomography (micro-CT), and its CAD model was created (Figure 4-33.b). Using the same methodology explained earlier, the porosity (0.6 mm pore cells) and a covering thin-wall structure (0.2 mm) added to the CAD model (Figure 4-33.c,d).

[1] Section 4.5 of this dissertation is part of a recently published journal paper by the author [10]

After creating the final CAD model for the porous plate, by following the previous procedure, an FE model for simulating the tensile behavior as well as an STL file for the SLM fabrications was created. In order to accurately characterize the tensile behavior of the Ni50.8Ti bone fixation plates, standard tensile samples were also designed and prepared for fabrication in addition to the bone fixation plates. Figure 4-34 shows the fabricated bone fixation plates immediately after fabrication and before the support removal procedure. Localized and overall thermomechanical behavior of the standard tensile coupon as well as the bone fixation plates, is discussed in the next section.

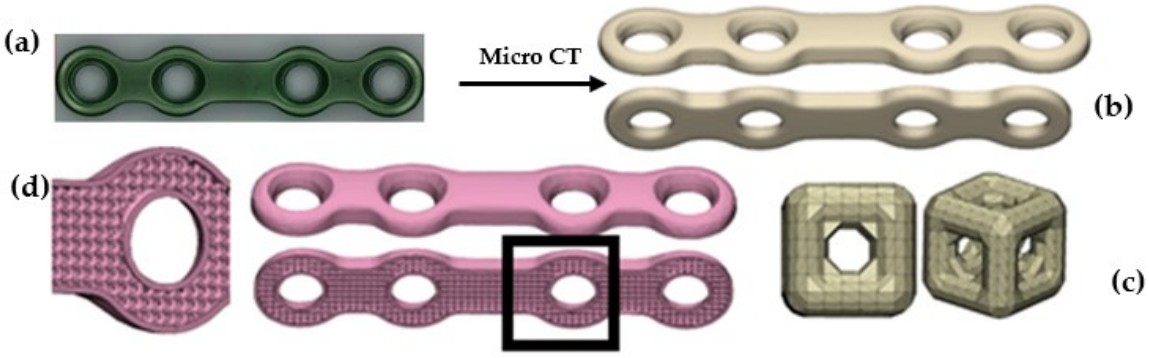

Figure 4-33 Preparation of a bone fixation plate with an extreme level of porosity and the realistic geometry. (**a**) Conventionally fabricated Ti64 bone fixation plate with standard geometry used as the reference, (**b**) reconstructed CAD through Micro CT, (**c**) porosity cell, and (**d**) porous bone fixation plate.

Figure 4-34 NiTi porous bone fixation plates and tensile samples fabricated via the SLM method.

4.5.1 Thermomechanical Behavior

DSC results, as well as the transformation temperatures of Ni-rich porous bone fixation plates, standard dog-bone samples, and powder particles, are shown and reported in Figure 4-35 and Table 4.4, respectively. For the porous plate, the DSC samples were cut from three different regions as shown in Figure 4-35. Based on the location that the DSC samples were cut from, different transformation temperatures were achieved. The transformation temperatures (TTs) variation can be explained by the nature of the SLM process and the complex shape of the porous plates that resulted in different thermal histories. The effect of different thermal histories during the SLM process can be compared to different heat treatment procedures, which are performed on the final parts. As different heat treatment procedures lead to different TTs, for instance, different thermal histories also can lead to non-homogeneous microstructure [240] as a result, different TTs. This non-homogeneity and variation in TTs variation indicate the necessity of the heat treatment as a post-processing procedure for the as-fabricated samples for creating a homogeneous part. In this section, we did not optimize the heat treatment procedure for the bone fixation plates and that will be studied in the next sections.

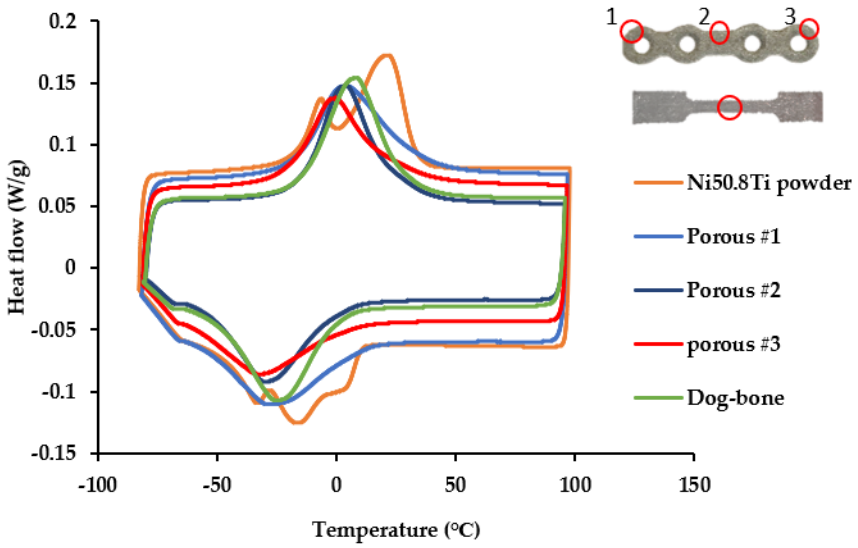

Figure 4-35 The differential scanning calorimetry (DSC) results of the as-fabricated porous bone fixation plate from three different locations, the dog bone sample, and Ni50.8Ti powder.

Table 4.4 The transformation temperatures (TTs) of powder, dog-bone, and the porous samples.

Sample	M_s (°C°C)	M_f (°C)	A_s (°C)	A_f (°C)
Powder	10.2	−46.6	−16.9	33.1
Porous #1	12.89	−57.08	−15.82	33.85
Porous #2	0.62	−56.09	−15.53	22.35
Porous #3	2.34	−54.36	−18.72	17.74
Dog-bone	2.14	−60.06	−15.10	26.96

To measure the material properties of the fabricated Ni-rich bone fixation plates and updating the FE model, two standard tensile samples were tested, and the results are shown in Figure 4-36. The first sample was loaded up to the failure with a low strain rate (0.0001 S−1) to maintain the isothermal condition. Based on the stress-strain plot of the first sample, a loading-unloading test on the second sample was designed. The second sample was loaded up to the end of the plateau region (3% strain) and then unloaded to zero loads. The transformation strain of 2.6% (81% of total strain) was achieved for the

as-fabricated part under tension. The material showed around 0.6% of irrecoverable strain that could be a result of permanent strain (slip) or the locked-in detwinned martensite and can be recovered by heating [241].

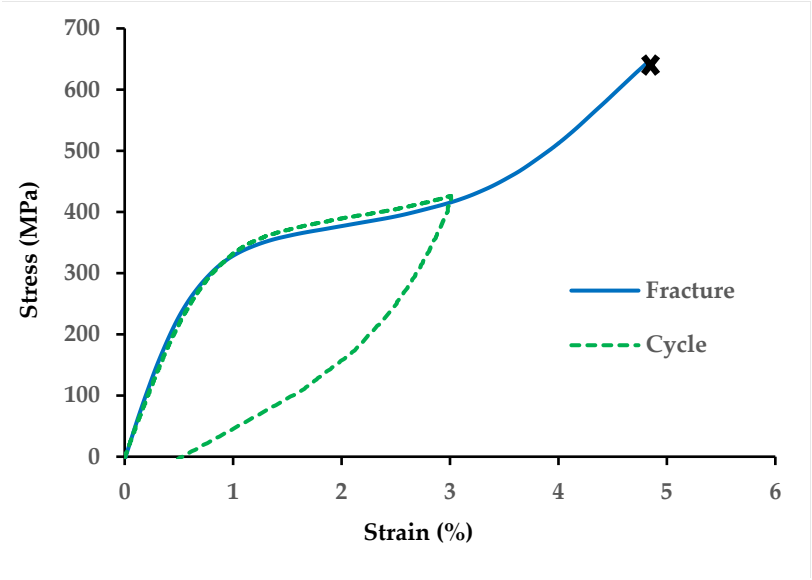

Figure 4-36 Stress–strain response of SLM dog-bone samples.

The mechanical properties of the as-fabricated material were reported in Table 4.5. The austenite (EA) and martensite (EM) modulus of elasticity were captured from loading and unloading plots, respectively. Followed by obtaining the material properties from the tensile samples, the Ni-rich bone fixation plate was simulated under tensile loading and unloading. The as-fabricated Ni-rich bone fixation plates were then mechanically tested under the same boundary conditions. Figure 4-37 shows the simulations as well as mechanical testing of the Ni-rich bone fixation plate.

After inspection of the fabricated Ni-rich bone fixation plates, we observed a relative geometrical difference between the fabricated part and the CAD model. The size had increased in comparison with the previous case (i.e., the first series of bone fixation plates with larger dimensions). As reported by others [242] , as-fabricated SLM

fabricated parts could exhibit a geometrical expansion that is related to the laser width, melt pool diameter, and the fact that the part is surrounded by loose powder. The geometrical expansion of SLM-fabricated parts has a more significant effect when the parts include fine details that are close to the laser width. In the case of fabricating Ni-rich bone fixation plates with the extreme geometrical features, the geometrical expansion led to a higher difference with the simulations and the expected behavior. In addition, because of the fine features of the Ni-rich bone fixation plates, a higher amount of un-melted powder was trapped in the pore cells that affect the mechanical response and could affect their biocompatibility. Therefore, we have investigated a chemical polishing method to remove the un-melted powder particles attached to the parts, while not disturbing the fine geometries. This procedure is discussed in the next section. Eventually, the polished bone fixation plate that showed 23% mass loss was mechanically tested, and the load–displacement response is shown in Figure 4-37.

Table 4.5 The mechanical properties of the standard tensile sample fabricated via SLM.

E_A (GPa)	E_M (GPa)	Critical Stress Start (MPa)	Critical Stress Finish (MPa)
54	36	350	430

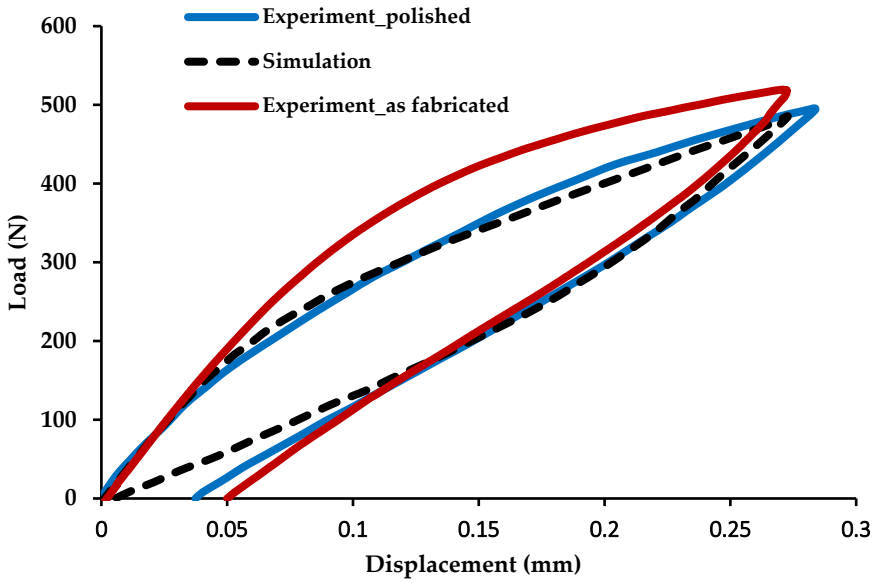

Figure 4-37 The load–displacement response of as-fabricated porous plate under tensile loading

4.5.2. Chemical Polishing

Using the selective laser melting process, the complex geometries required for the bone fixation plates can be accurately fabricated. However, the SLM process often results in un-melted powders and other undesirable features that remain fused to the fabricated product. In order to remove the un-melted powder and to add a smooth finish to the part to improve performance (e.g., mechanical, cleaning, and sterilization reliability), a finishing process is required. Due to the complex geometries and fine porous structure of Ni-rich implants, current mechanical finishing processes are not efficient. They may damage the components and cannot reach fine internal features. Therefore, a chemical etching process was opted for. The chemical etching and finishing processes of additively manufactured nickel–titanium components is not well researched. Therefore, a series of

tests were undertaken in order to better optimize the etching solution used for the bone fixation plates.

The tests consisted of two different etching solutions and three different times for submerging the components within those solutions. The samples were cleaned in water using an ultrasonic bath for 5 min both before and after the chemical finishing process. Both solutions were composed of hydrofluoric acid (HF), nitric acid (HNO_3), and purified distilled water (H_2O). It is known that the HF in the etching solution act as a dissolvent while the HNO_3 behaves as a passivator [243] . The distilled water is used to dilute the solution in order to prevent excessively rapid corrosion/material loss. The samples were submerged for 2 min, 4 min, and 6 min.

Figure 4-38 shows the results of the chemical etching process on the mass loss of the samples etched the two trialed solutions. Three bone-plate was etched within the etching solution 1 while three others were etched within the solution 2. The mass loss increased proportionally with the time for both solutions. The results show that the second solution with reduced HF and increased HNO_3, removed material at nearly twice the rate of solution 1.

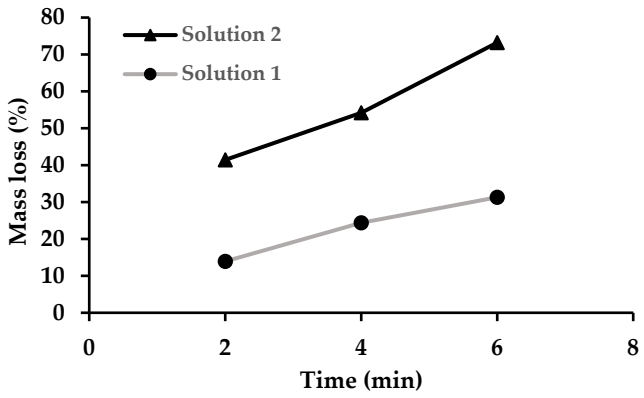

Figure 4-38 The percentage of mass loss versus time for two different etching solutions.

The effect of the etching procedure on the geometry, as well as the surface finish of the samples, is reflected in the SEM images in Figure 4-39. As it can be seen in the "As-built" sample, excessive un-melted powder is attached to the surface of the as-built sample and almost entirely covered the pores. S1-2, S1-4, and S1-6 show the SEM images of samples etched with solution 1 with the different durations of 2, 4, and 6 min. The un-melted powder was partially removed on S1-2. S1-4 and S1-6 that were submerged for a long time showed the best result of the chemical polishing. In order to make a more accurate comparison on the effect of chemical polishing, the distance between the pores was measured and compared with the original distance on the CAD file. Based on this comparison, the size and geometry of S1-2 had the most consistency with the original CAD model, and therefore it was reported as the optimized polishing procedure. The polishing by solution 2 for 2 min (S2-2) was almost good but still more than required. While the polishing with solution 2 for 4 and 6 min (S2-4 and S2-6) was too aggressive and caused excessive degradation of the pore structures.

4.5.3 Chemical composition analysis

Understanding the chemical composition of bone fixation plates is critical. Since this is a medical implant, strict controls are required to ensure biocompatibility (i.e., lack of toxicity). Analyzing and accounting for any precipitates or ion formation due to the additive manufacturing process is, therefore, a necessity. The results for our chemical analysis of these bone fixation plates is displayed in Table 4.6. The analyzed elements were carbon (C), hydrogen (H), oxygen (O), nitrogen (N), nickel (Ni), cobalt (Co), copper (Cu), chromium (Cr), iron (Fe), niobium (Nb), and titanium (Ti). The composition analysis is compared with the allowable values of nickel–titanium shape memory alloys for medical devices and surgical implants, as described in ASTM F 2063. The results show that the AM Nitinol compositions were within expected parameters with respect to total weight percentage. However, the nitrogen plus oxygen level was slightly above the acceptable ASTM requirement at this stage in our work. The cobalt, copper, chromium, nitrogen, carbon, hydrogen, and niobium were not present in a quantity sufficient to alter the predicted mechanical performance. Ratios of iron and oxygen were also low and do not present an obstacle to the performance and safety of these bone fixation plates.

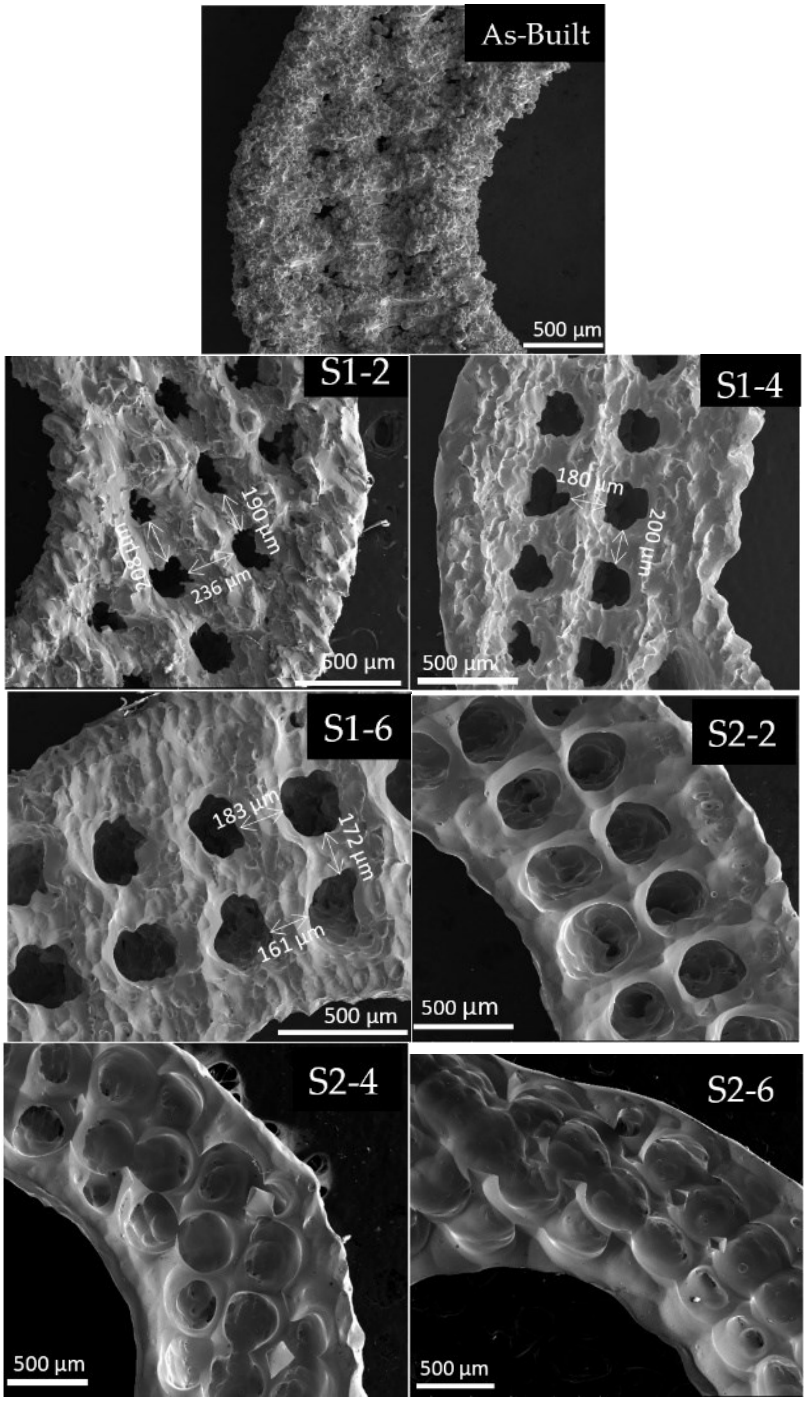

Figure 4-39 SEM result of chemically polished porous plates under six different etching conditions.

Table 4.6 The results of the chemical composition analysis.

Element.	Composition (wt. %)	ASTM F-2063 Composition Requirements (wt. %)
Nickel	56.0	54.5–57.0
Carbon	0.002	<0.050
Cobalt	<0.0005	<0.050
Copper	<0.0005	<0.010
Chromium	<0.0005	<0.010
Hydrogen	0.0004	<0.005
Iron	0.016	<0.050
Niobium	<0.002	<0.025
Oxygen	0.058	-
Nitrogen	<0.005	-
Nitrogen + Oxygen	<0.063	<0.050
Titanium	Balance	Balance

4.6 Surface quality improvements via re-melting

4.6.1 Parameter selection and design of experiments

The optimized process parameters as shown in Table 4.7 were used as the base parameters for the fabrication of re-melting samples. As it is discussed in the methods section, to implement the re-melting approach, during the SLM fabrication, after scanning each layer and prior to the powder deposition for the next layer, the laser conducts a second round of melting or Re-melting procedure with a reduced level of energy density and therefore modulated process parameters (i.e. the scanning velocity and the laser power). The process parameters for the re-melting procedure were selected in a way to cover a broad selection of laser scanning speed vs. the laser power, as it is shown in Figure 4-40 and reported in Table 4.8. As it can be seen in Table 4.8, the energy density of the process parameters for the re-melted layer was ranging from 20% to 78%

of the energy density of the based process parameters (Table 4.7). Cubic samples with the dimension of 4x4x10mm were elected for the remitting procedure.

Table 4.7 The based process parameters for the fabrication of re-melting samples.

Sample number	Power (W)	Scanning speed (mm/s)	Hatch spacing (mm)	Layer **thickness** (mm)	Energy density (J/ mm^3)
1	250	1250	0.08	0.03	83.34

Table 4.8 Process parameters for the re-melting procedure

Sample number	Power (W)	Scanning speed (mm/s)	Hatch spacing (mm)	Layer **thickness** (mm)	Energy density (J/ mm^3)	Energy ration (%)
2	50	800	0.08	0.03	26.04	31
3	87.5	1200	0.08	0.03	30.38	36
4	125	800	0.08	0.03	65.10	78
5	50	1200	0.08	0.03	17.36	21
6	87.5	1000	0.08	0.03	36.46	44
7	125	1200	0.08	0.03	43.40	52
8	87.5	800	0.08	0.033	41.43	50

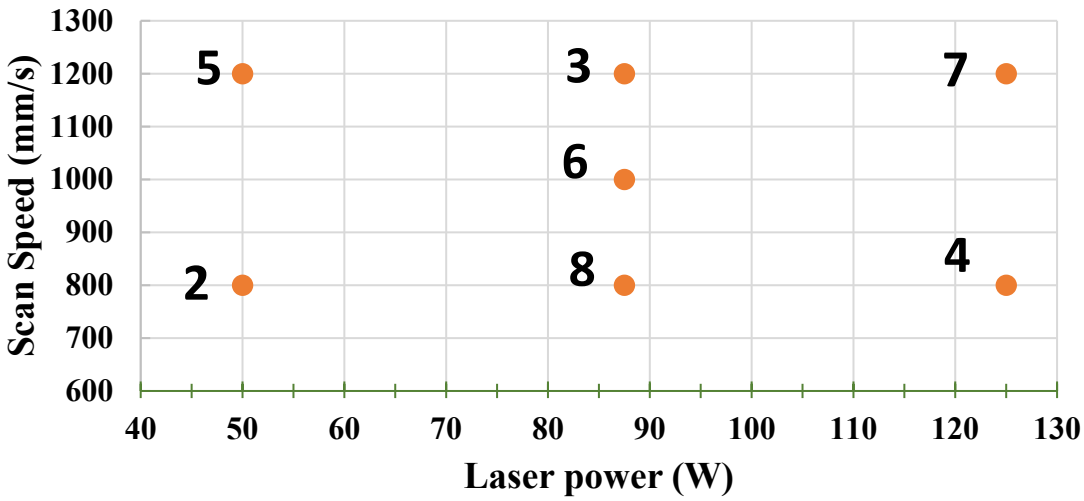

Figure 4-40 Parameters selection for evaluating the effect of re-melting

4.6.2 Density measurements

Followed by fabricating the re-melting samples, as the first step the densities of the parts were measured using Archimedes method and compared with the as-fabricated samples. Three measurements were done for each sample and the average value was reported as the final value. Table 4.9 shows the measured densities as well as percentage change in the density of the re-melted parts with respect to the as-build sample. As it can be seen in Table 4.9, density of the re-melted parts increased in all the cases from 0.23% to 1.04%. For a better demonstration, Figure 4-41 shows the percentage increase in the density of the re-melted samples on the scan speed vs. laser power diagram. As it can be seen, samples with higher laser scanning speed led to a higher increase in the density (i.e. sample 1 and sample 7). It can be concluded that proper re-melting procedure has the capacity to remove some part of the trapped gas. However, by increasing the energy density in general, probably due to higher level of powder spatters, additional trapped gas might be formed in the part that prevent the density increase. For a better understanding of this phenomena the use of micro CT scan and evaluation of the internal pores is suggested which is out of the scope of the current work. As an alternative, re-melted samples were analyzed using SEM method to be evaluated in terms of surface conditions.

Table 4.9 Measured density as well as percentage change in the density of the re-melted samples

Sample #	Power (W)	Scan speed (mm/s)	Energy input	Density (g/cm^3)	% change
1	0	0	--	6.299	0.00
2	50	800	26.04	6.3135	0.23
3	**87.5**	**1200**	**30.38**	**6.3645**	**1.04**
4	125	800	65.10	6.321	0.35
5	50	1200	17.36	6.3355	0.58
6	87.5	1000	36.46	6.338	0.62
7	**125**	**1200**	**43.40**	**6.345**	**0.73**
8	87.5	800	27.62	6.3385	0.63

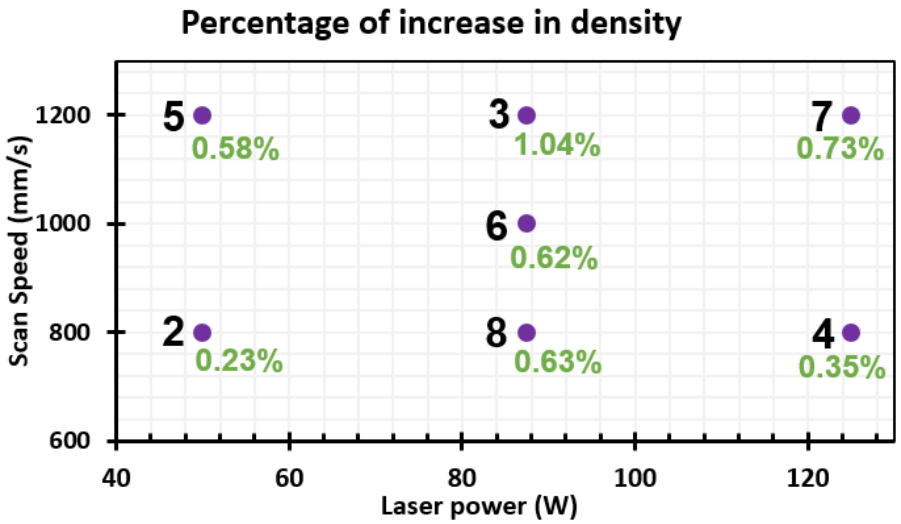

Figure 4-41 Percentage increase in the density of the re-melted parts in comparison to the as-fabricated samples

4.6.3 Surface roughness measurements

The surface roughness of the re-melted samples as well as the as-built sample were measured in two steps. Side surfaces and the top surface were measured separately. Based on the results the top surfaces showed a more significant improvement in the surface roughness. Figure 4-42 shows the side surface roughness of the samples. As it can be seen the surface roughness of the side surfaces was not significantly affected since still the loose powder in adjacent to the side surfaces fuse to these surfaces and increase the

surface roughness. However, as it can be seen in Figure 4-43, the surface roughness of the top surfaces is significantly affected by the remitting procedure. Although only the top surface is affected by the re-melting procedure, this surface plays an important role in improving the density and reducing the micro-voids in the parts. Re-melting in each layer creates a smoother surface after each melting procedure (and before deposition of the powder for the next layer) that improves the integrity of the powder for the next layer and reduces the voids or trapped-gas regions. However, too aggressive re-melting process parameters might lead to additional powder spattering that reduces the density and leads to void or micro-pores formation.

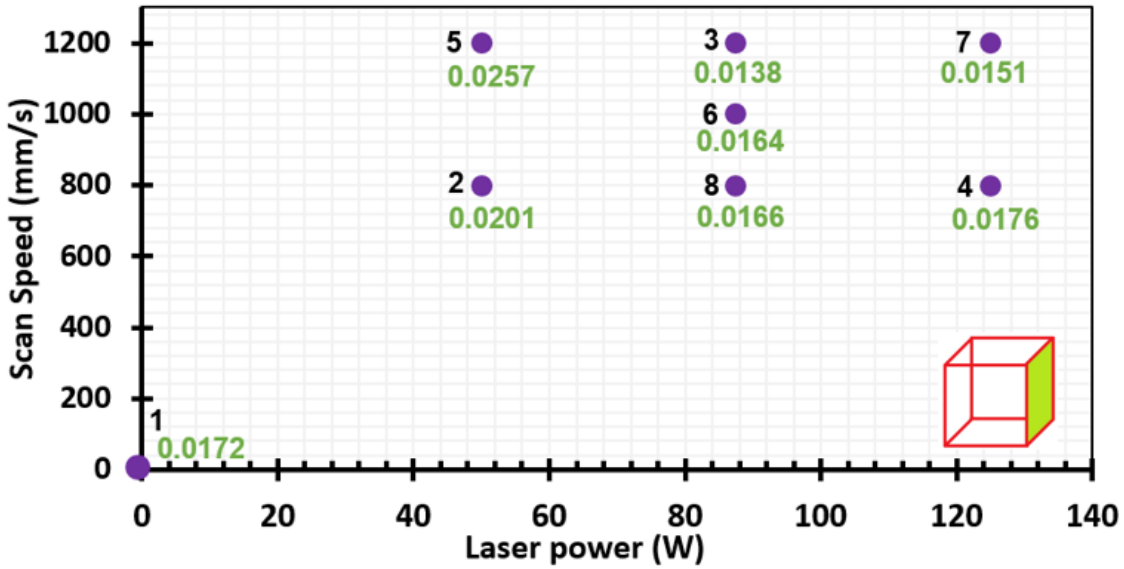

Figure 4-42 Side surface roughness of the re-melted samples expressed on the scanning speed vs. laser power of the re-melted layer

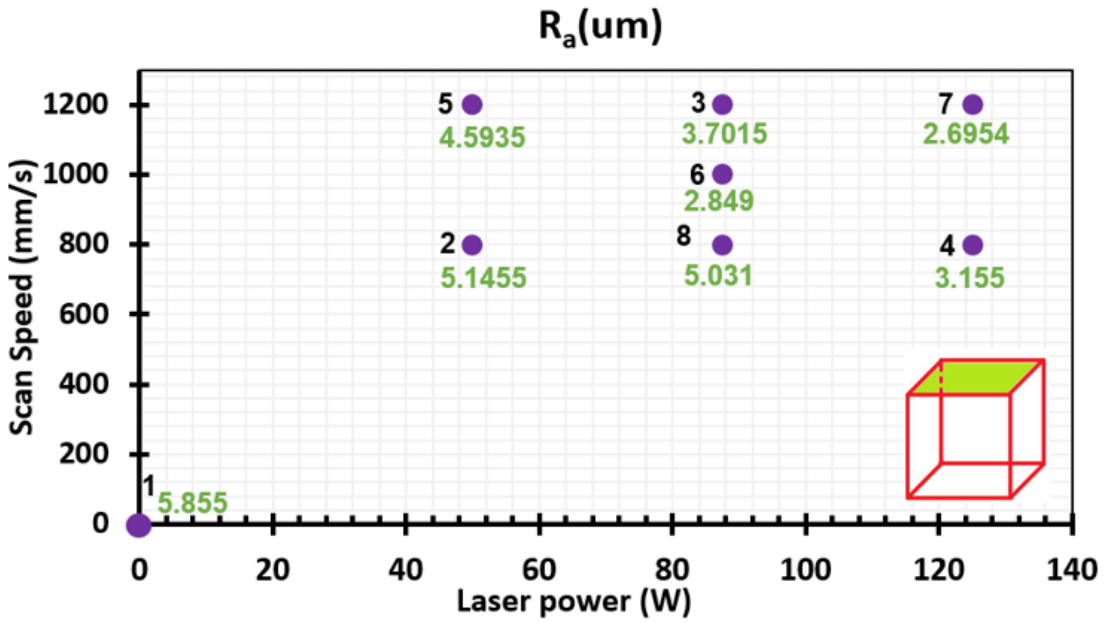

Figure 4-43 Surface roughness of the top surface of the re-melted and as-built samples demonstrated on the scanning speed vs. laser power of the re-melted layer

4.6.4 Surface analysis via SEM

In addition to the roughness measurements, the top surfaces of the re-melted as well as as-built samples were investigated via SEM. Figure 4-44 shows the top surface of the as-built sample. As it can be seen, the top surface of the as-built sample contains powder particles, voids, and a visible rough track of laser that significantly increases the surface roughness. On the other hand, as it can be seen in Figure 4-45, the re-melting procedure removed the un-melted powder particles and filled the voids in most of the cases. However, based on the width of the re-melted layer and the overlap between the layer the roughness and the quality of the top surface is affected. In addition, in order to fabricate a homogeneous part, it is preferable to utilize re-melting process parameter that lead to some levels of overlap between the melt pools during the re-melting. To clarify, as it can be seen in Figure 4-45.2, the width of the melt pool in sample 2 is not enough to cover the whole surface based on the hatch spacing parameter. The same condition can be

seen in samples 5 and 8. On the hand, in samples 3, 4, 6, and 7 the melt pool width of the re-melting process was high enough to cover the area and lead to a smoother and more integrated surface. The SEM observations also verified the roughness measurement of the top surfaces, and as it was reported in Figure 4-43, the samples with a complete coverage in the re-melting process also showed lower values of surface roughness.

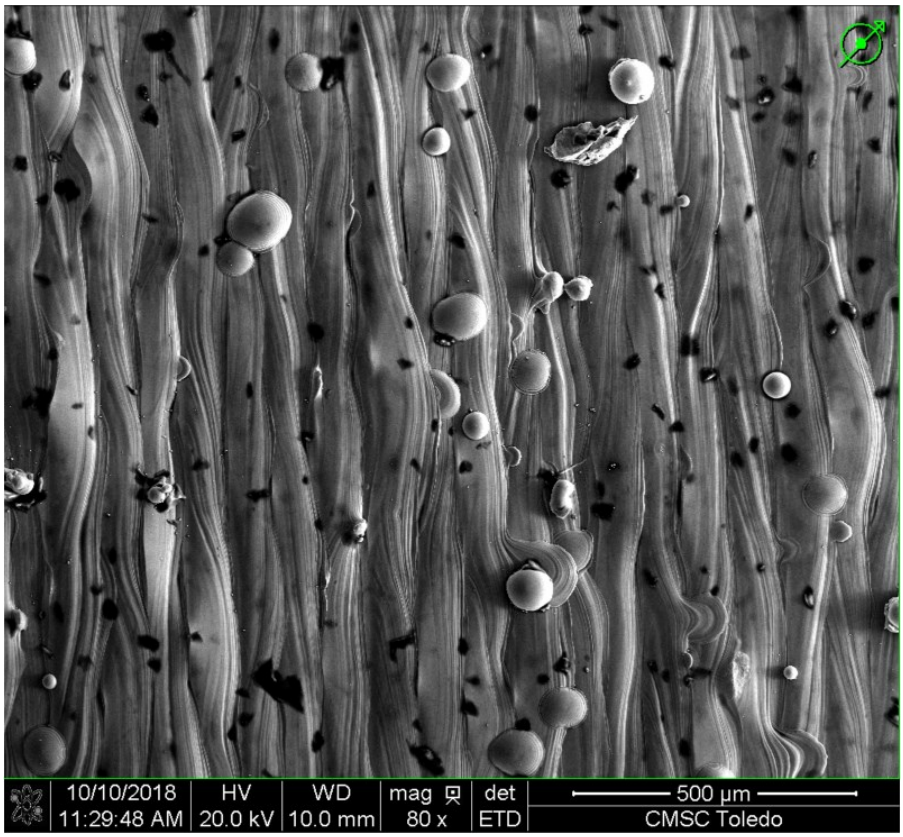

Figure 4-44 SEM image of the top surface of the as-built sample

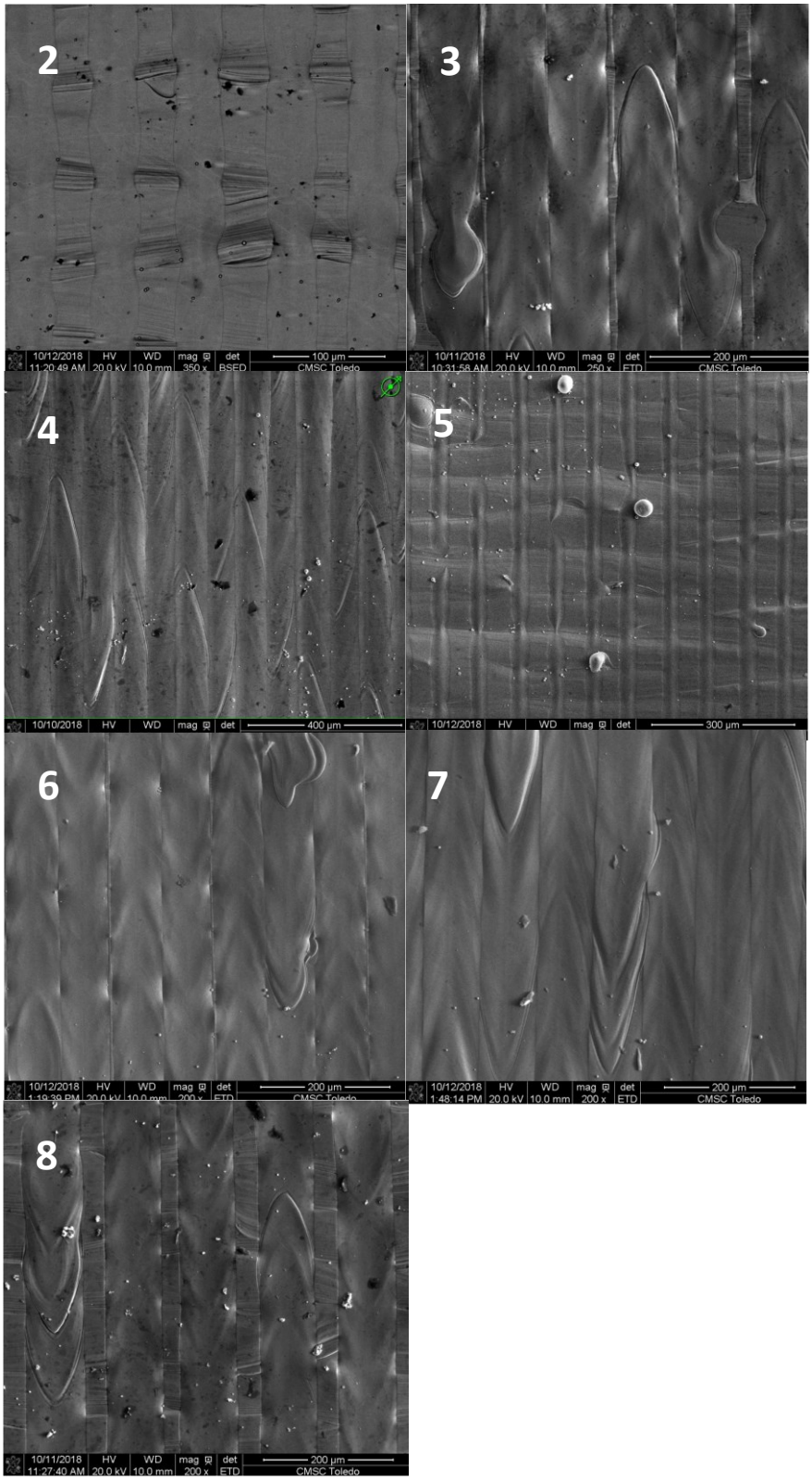

Figure 4-45 SEM images of the top surfaces of the re-melted samples

4.6.5 Additional measurements and conclusions for future studies

In order to quantitatively evaluate the melt pool widths and measure the laser width obtained by different re-melting process parameters, the laser width in different case were measured and reported based on the laser power and based on the laser scanning speed. A similar set of plots is recommended to be used for developing and optimizing the re-melting process parameter. Figure 4-46 shows the melt pool width verses the laser power. As It can be seen, increasing the laser power as well as reducing the scanning speed increase the melt poll width. Figure 4-47 shows the re-melting melt pool width verses laser scanning speed. Here again as it can be seen, increasing the laser scanning speed as well as reducing the laser power, reduce the melt pool width. These two plots can be used to stablish an explicit relationship based on the laser width and scanning speed to calculate the melt pool width.

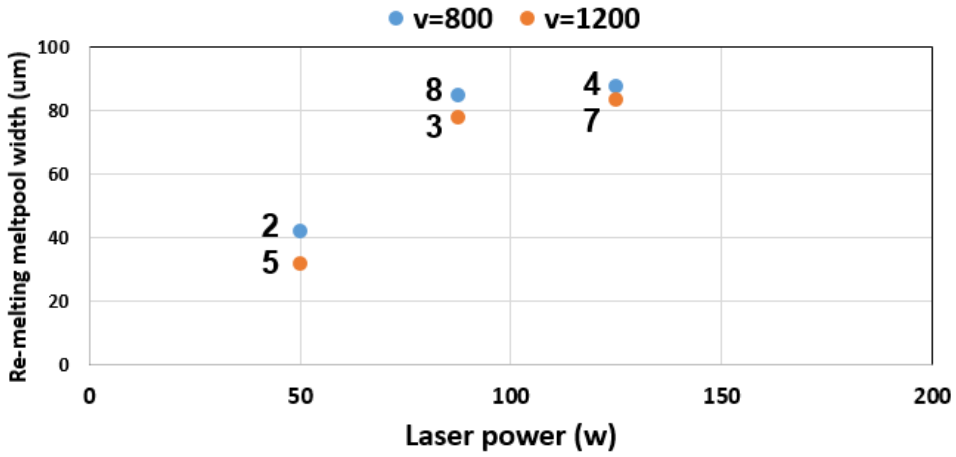

Figure 4-46 Melt pool width verses laser power for two different laser scanning speed

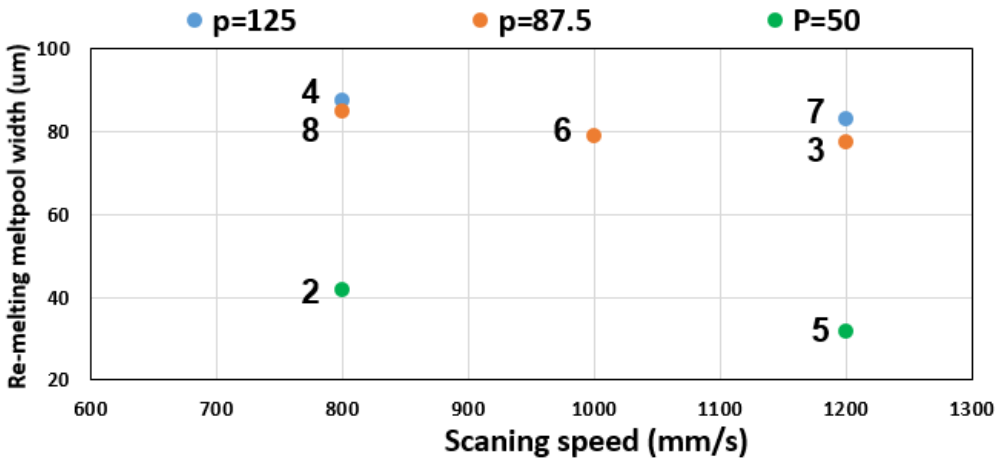

Figure 4-47 Re-melting melt pool width verses scanning speed for two different laser powers

As it is shown earlier, the re-melting procedure increases the density by reducing the trapped-gas regions in the part. In addition to measure the density of the parts, micro CT scan technique should also be used to analyze the internal voids and micro-pores. Due to the limited access to a micro CT scanner equipment, only two samples were analyzed via micro CT method and a reduction in internal pores/voids was observed in the re-melted sample. However, a more detailed CT-scan study should be performed with a higher resolution instrument to present a better assessment of the re-melting process.

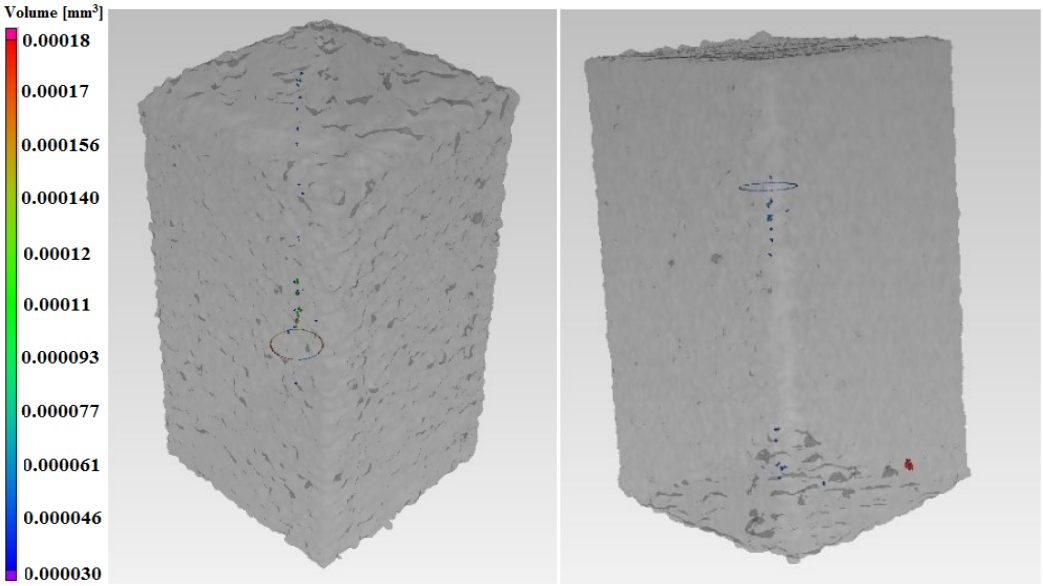

Figure 4-48 Micro CT scan of the a) as build, and b) re-melted (#4) samples

4.6.6 Transformation temperatures of the re-melted parts

After evaluating the density and surface roughness of the re-melted samples the thermomechanical properties of the re-melted specimens should be evaluated. To this end, first 5 different DSC samples from different heights were cut from the as-built sample as well as sample #2. For each category of the samples (as built and re-melted), DSC samples show similar transformation temperatures (<5°C difference in transformation temperatures). This observation indicated that the as-built as well as the re-melted specimens in this study were homogeneous in the height and the re-melting did not significantly affect the homogeneity of the parts in terms of transformation temperatures. However, for more complex geometries, similar to the porous skeletal fixation plates discussed earlier, DSC samples must be obtained from different regions to verify that the parts are homogenous. Preferably, a solution annealing process should be utilized to homogenize the AM fabricated parts with complex geometries. Here based on

these results, the as-built and re-melted samples with no solution annealing were compared.

Table 4.10 reports the transformation temperature of the as-built and re-melted samples. For an easier comparison of the transformation temperature, these values are graphically shown in Figure 4-49. As it can be seen, the transformation temperatures have not significantly changed followed by the re-melting procedure. The reason can be attributed to the fact that the melt pools created by the main melting process melt down 3 to 4 layers of the powder, and therefore have a significant effect on the microstructure and thermomechanical response of the part. In other word, re-melting in each layer may alter the microstructure, however, the main melting of the next layer neutralizes this effect. Although it is not in the scope of the current study, it should be noted that re-melting improves the density and reduces the pores that could significantly improve the fatigue life of the AM samples and must be studied in a separate study.

Table 4.10 Transformation temperature of the as-built and re-melted specimens

SPECIMEN	M_F (°C)	M_S (°C)	A_S (°C)	A_F (°C)
1	-26.2	12.7	-3.7	40.9
2	-31.5	10.6	-3.8	39.6
3	-32.4	8.5	-6.7	37.1
4	-25	18.2	0.6	45.7
5	-32.6	8.2	-5.8	34.7
6	-34.1	5.4	-7.1	33.5
7	-31	9.5	-7.3	35
8	-29.5	4	-6.3	27.1

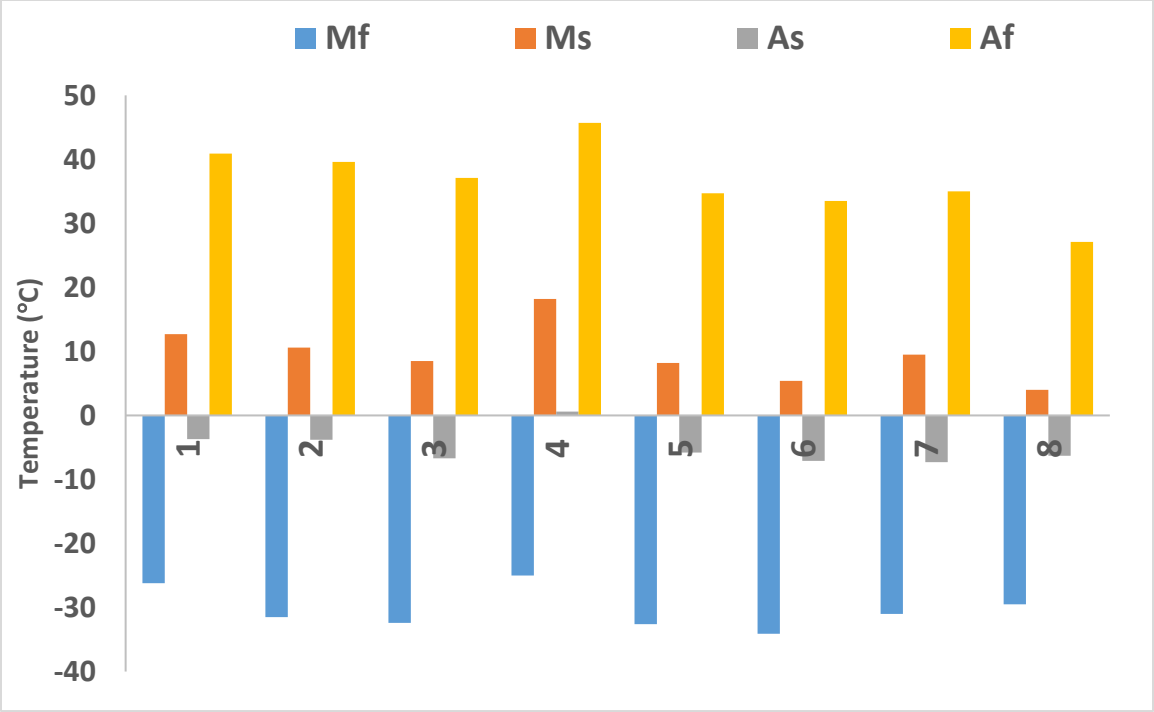

Figure 4-49 Graphical demonstration of the transformation temperature of re-melted as well as as-built specimens.

4.7 Optimizing the heat treatment to improve the superelasticity

4.7.1 Parameter selection and design of the study

As it was mentioned earlier in the literature review, heat treatment procedures in form of solution annealing and aging significantly alter the microstructure and perception mechanisms in NiTi alloys. Altering the microstructure and introducing or modifying or removing precipitates in the NiTi matrix directly influence the thermomechanical behavior of the NiTi alloy and change the transformation temperatures as well as superelasticity and shape memory response. Therefore, by utilizing a proper heat treatment procedure, that could be combination of solution annealing and or aging, one can improve the desired thermomechanical response of the NiTi alloys. In addition, in case of additive manufacturing, a non-homogeneity in microstructure has been observed in fabricated parts, especially where the parts have complex geometries. The reason is that different heat transfer mechanisms and cooling rates in different regions of the part lead to different microstructures. Solution annealing has the potential to homogenize the AM fabricated parts and unify the microstructure. In this part, we have investigated a series of solution annealing procedures obtained from the literature, in order to improve the superelasticity. A potential similar step can be defined to optimize the aging procedure followed by the solution annealing. Seven different sets of solution annealing parameters were selected based on the relevant literature for heat treating the AM fabricated NiTi parts. Table 4.11 shows the annealing parameters as well as the cooling

method. It has been shown that cooling method also plays an important role in altering the microstructure and must be carefully selected.

Table 4.11 Solution annealing parameters for heat treatment of the AM NiTi parts

Number	Temperature	Duration	Cooling method	Code name
A1	700	30 minutes	Furnace cooled	700C-30m-F
A2	700	30 minutes	Water quenched	700C-30m-W
A3	700	5.5 hours	Water quenched	700C-5.5h-W
A4	850	15 minutes	Water quenched	850C-15m-W
A5	950	30 minutes	Water quenched	950C-30m-W
A6	950	5.5 hours	Furnace cooled	950C-5.5h-F
A7	950	5.5 hours	Water quenched	950C-5.5h-W
A8	-	-	-	As-built

Table 4.12 Process parameters for fabricating the heat treatment samples

Effective laser power (W)	Layer thickness (µm)	Scanning velocity (m/s)	Hatch distance (µm)	Energy input (J/mm^3)
250	30	1.25	120	83.25

4.7.1 Effect of sample preparation

In order to evaluate the thermomechanical properties of the heat-treated specimens, the transformation temperatures and compression response were investigated. To prepare the DSC specimens a 20-50 mg section were cut from the main parts via a diamond-saw slow-cutter. To investigate the effect of sample preparation on the DSC measurements, for two heat treatment procedures DSC samples were cut both after and

before heat treatment. Figure 4-50 shows the DSC measurement and transformation temperatures of the sample heat treated at 850 °C for 15 minutes, when the DSC sample was prepared after and before the heat treatment. As it can be seen there is minor shift in transformation temperatures to the right (higher values) when the samples are prepared after the heat treatment.

shows the DSC measurement and transformation temperatures of the sample heat treated at 700 °C for 30 minutes, when the DSC sample was prepared after and before the heat treatment. The difference between the two samples in this case is more negligible that can be attribute to the fact that the temperature was lower. It can be concluded that although the effect of sample preparation on the DSC measurements is generally negligible, by reducing the oxidation during the heat treatment and utilizing a coolant during the DSC-sample cutting this effect can be minimized. It should be mentioned that for the biomedical industry and based on the specific application, a precise protocol for DSC measurements must be developed. Here for the remaining part of the study, the DSC samples were cut before the heat treatment and polished after the heat treatment.

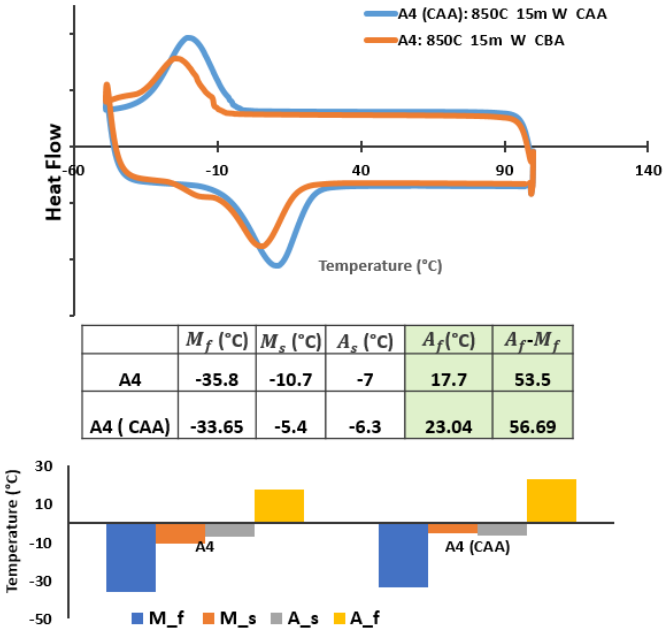

	M_f (°C)	M_s (°C)	A_s (°C)	A_f(°C)	A_f-M_f
A4	-35.8	-10.7	-7	17.7	53.5
A4 (CAA)	-33.65	-5.4	-6.3	23.04	56.69

Figure 4-50 Effect of sample preparation via cutting after and before heat treatment for the sample heat treated at 850 °C for 15 minutes

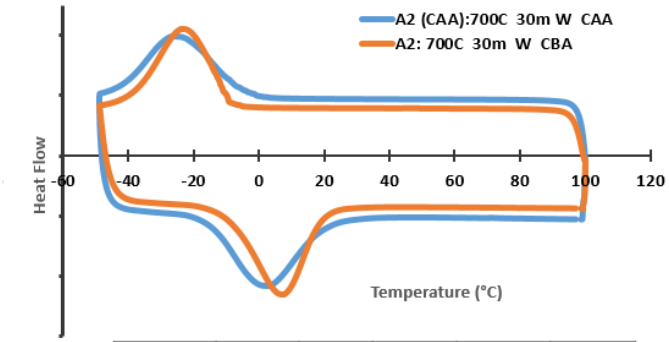

	M_f (°C)	M_s (°C)	A_s (°C)	A_f(°C)	A_f-M_f
A2	-36.8	-8.8	-8	19	55.8
A2 (CAA)	-40.4	-6.4	-15.21	19.1	59.5

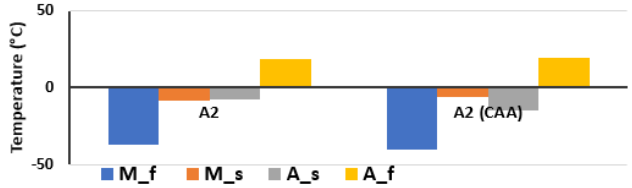

Figure 4-51 Effect of sample preparation via cutting after and before heat treatment for the sample heat treated at 700 °C for 30 minutes

4.7.3 Effect of annealing time

The other important parameter in the heat treatment procedure is the heat treatment duration. It is suggested to select relatively long heat treatment durations to ensure the part is fully exposed to the desired temperature. Figure 4-52 shows the transformation temperatures and mechanical properties of the samples heat treated at 950 °C and at 700 °C for two different durations. The mechanical test (i.e cyclic compression test) was performed at Af +15 °C for all the samples from so on to remove the effect of ambient temperature. As it can be seen, at 950 °C (higher temperature), transformation temperatures and the mechanical response are not significantly altered when the heat treatment duration is increased from 30 minutes to 5.5 hours. However, for the case of 700 °C mechanical properties were more affected due to the heat treatment time. It can be concluded that 700 °C the alloy is not fully stable and heat treatment duration has a more significant effect.

4.7.4 Effect of cooling method

Figure 4-53 shows the transformation temperatures and mechanical properties of the samples heat treated at 700 °C for 30 minutes and samples heat treated at 950°C for 5.5 hours with two different cooling mechanisms: water quenching, and furnace cooling. By comparing these two cases, it can be seen that in the case of heat treating at 700°C there is only a negligible difference between the thermomechanical response of the water quenched and furnace cooled samples. However, for the case of heat treatment at 950°C, there is a significant difference between the mechanical response of the water quenched and furnace cooled samples. It can be concluded that the heat treatment at 700°C for 30 minutes does not lead to a significant change in the microstructure (i.e. recrystallization)

of the parts. Therefore, changing the follow-on cooling mechanism does not lead to a different microstructure and the mechanical response remains the same. However, for the case of heat treatment at 950 ºC for 5.5 hours, water quenching led to a significant change in the mechanical response of the sample. It can be concluded that heat treatment at 950 ºC for 5.5 hours triggered the recrystallization mechanism and the water quenching led to a microstructure freeze in the sample. However, the furnace cooling caused relaxation in the material and the mechanical response in this case was closer to the as fabricated samples. The other conclusion is that, although the strain recovery at 600 MPa reduced in the case of water quenching for the samples heat treated at 950 ºC for 5.5 hours, the plateau level and the austenite Young's modulus have increased in this condition. It could be possible that in case of testing the samples at higher levels of load, the same recovery observed in the sample. However, in our experiments the level of load was fixed to 600 MPa and therefore, the plateau was not observed for the water quenched sample. One needs to consider all these effects and optimize the heat treatment procedure based on that.

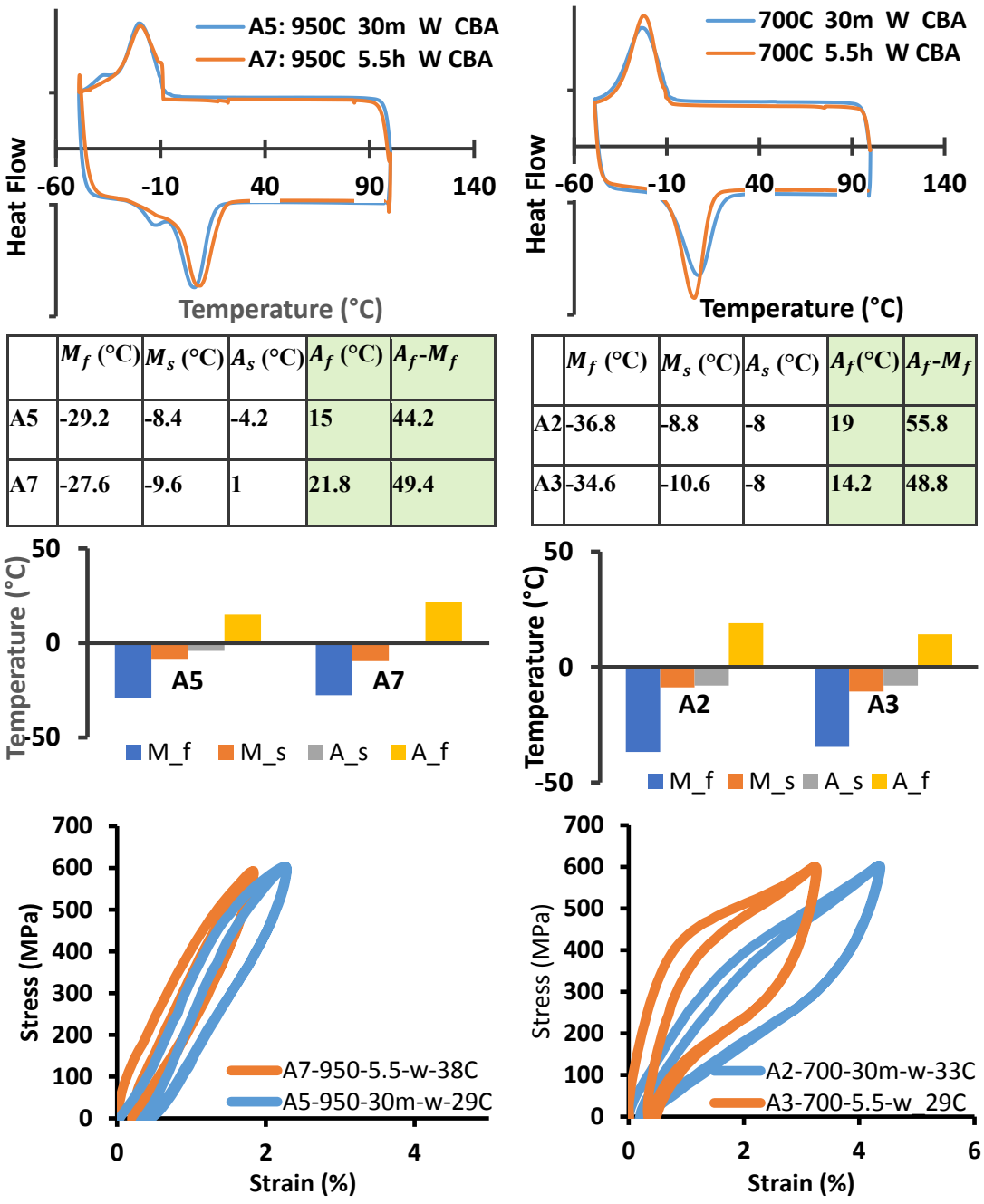

	M_f (°C)	M_s (°C)	A_s (°C)	A_f (°C)	A_f-M_f
A5	-29.2	-8.4	-4.2	15	44.2
A7	-27.6	-9.6	1	21.8	49.4

	M_f (°C)	M_s (°C)	A_s (°C)	A_f(°C)	A_f-M_f
A2	-36.8	-8.8	-8	19	55.8
A3	-34.6	-10.6	-8	14.2	48.8

Figure 4-52 Transformation temperatures and mechanical properties of samples heat treated at 950 C (a, b, c, and d) and at 700 C (e, f, g, and h) for different durations (the effect of annealing time)

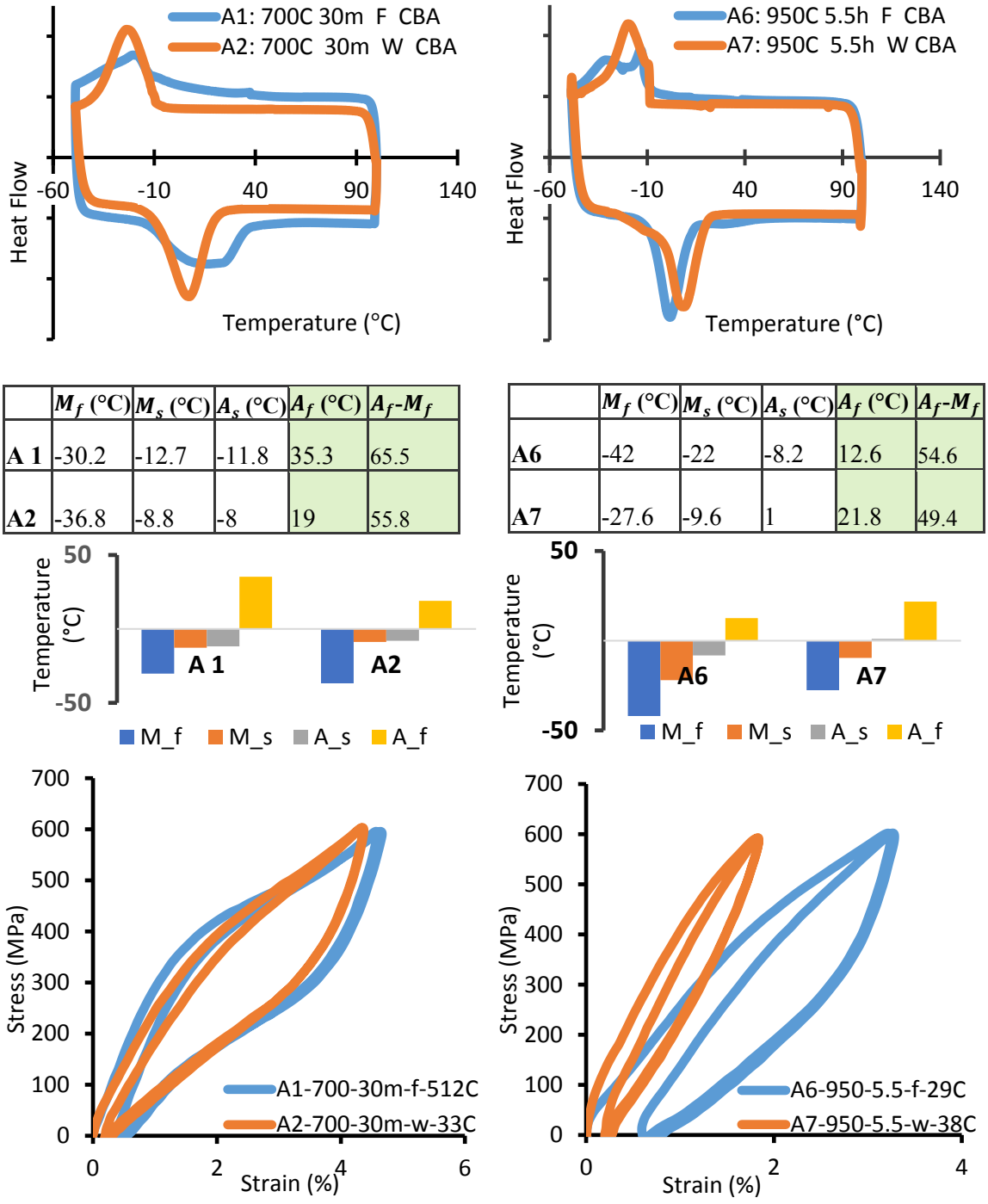

	M_f (°C)	M_s (°C)	A_s (°C)	A_f (°C)	A_f-M_f
A 1	-30.2	-12.7	-11.8	35.3	65.5
A2	-36.8	-8.8	-8	19	55.8

	M_f (°C)	M_s (°C)	A_s (°C)	A_f (°C)	A_f-M_f
A6	-42	-22	-8.2	12.6	54.6
A7	-27.6	-9.6	1	21.8	49.4

Figure 4-53 Transformation temperatures and mechanical properties of samples heat treated at 700 C for 30minutes (a, b, c, and d) and at 950 C for 5.5 hours (e, f, g, and h) with different cooling mechanisms (the effect of cooling mechanism, furnace cooled verses water-quenched)

4.7.5 Effect of annealing temperature

In this section the effect of temperature on the heat treatment is demonstrated via comparison of the thermomechanical response of the samples heat treated at 700 ºC and 950 ºC both for 5.5 hours and water quenched at the end. As it can be seen in Figure 4-54, while the transformation temperatures changed less than 10 ºC, heat treatment at 950 ºC increased the plateau level and had a more significant effect on the mechanical response. In addition, comparison of these two conditions with the as-fab sample revealed that heat treatment at 700 ºC for 5.5 hours had a minor effect on the microstructure and thermomechanical response. With regards to the observations discussed in this and previous sections it can be concluded that heat treatment at 950 ºC for 5.5 hours followed by water quenching significantly alter the microstructure of the as-fabricated parts. However, the as-fabricated parts showed a relatively good superelasticity at 600 MPa and based on the application can be used with no additional heat treatment. The other fact is that heat treatment also homogenizes the microstructure especially in the cases with complex geometries and therefore, even when the as-fab part's thermomechanical properties satisfies the requirement, it is suggested to utilize a heat treatment followed by the fabrication. The heat treatment can be divided in two parts, such as solution annealing and aging. One may utilize the solution annealing to homogenize the microstructure and then utilize the aging to introduce precipitates and manipulate the SE and SME effects. For the application of bone fixation plates, due to the complexity of the geometry we proposed utilizing a heat treatment at 700 ºC for 5.5 followed by water quenching.

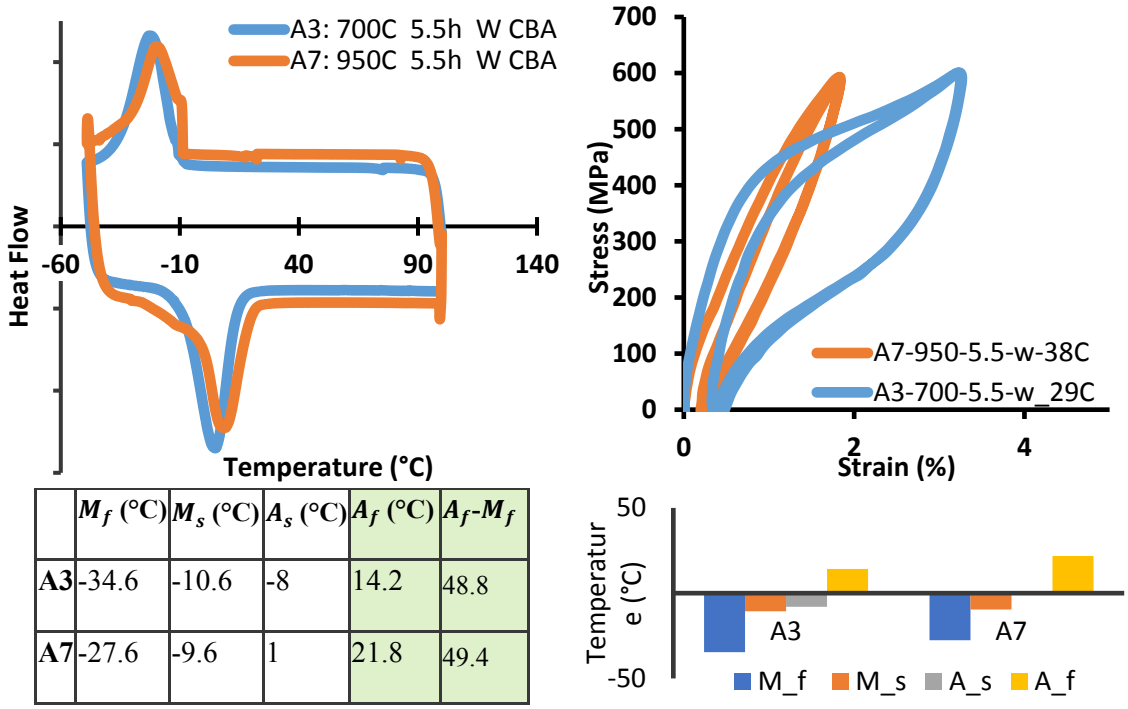

	M_f (°C)	M_s (°C)	A_s (°C)	A_f (°C)	A_f-M_f
A3	-34.6	-10.6	-8	14.2	48.8
A7	-27.6	-9.6	1	21.8	49.4

Figure 4-54 Transformation temperatures and mechanical properties of samples heat treated at 700 C and at 950 C for 5.5 hours (the effect annealing temperature)

4.7.6 Thermomechanical behavior of the heat-treated parts

In order to optimize the heat treatment procedure, after designing the experiments different properties including, all transformation temperatures, thermomechanical behavior at a constant temperature difference from the transformation temperatures (e.g. Af +15℃), Thermomechanical behavior at the desire temperature (e.g. the body temperature 38℃), maximum strain, irrecoverable strain, recovery ratio, plateau level and Young's modulus (e.g. Ea) should all be analyzed and investigated to optimize the heat treatment procedure. Having different variables defining the thermomechanical response of shape memory alloys is a main challenge in working with them. One should carefully understand the effect of each parameter and select the optimized heat treatment procedure based on that. In this section these thermomechanical properties are analyzed for our heat

treatment study to represent a sample analysis of the shape memory heat treatment optimization procedure. Figure 4-55 and Table 4.13 show the transformation temperatures of the heat treated as well as as-built samples. As it can be seen a variety of transformation temperatures were achieved through our heat treatment study. For instance, Af is ranging from 12 to 36 ℃. Therefore, for a superelastic application at the body temperature, it is suggested not to use A1 or A8, since they are too close to the body temperature. However, other heat treatment must be evaluated at the body temperature. Based on the SMAs phase diagram, the difference between the working temperature and the Af directly affects the plateau level, and it shown to affect the fatigue life as well [244]. Therefore, the final transformation temperatures of the SMA must be carefully selected.

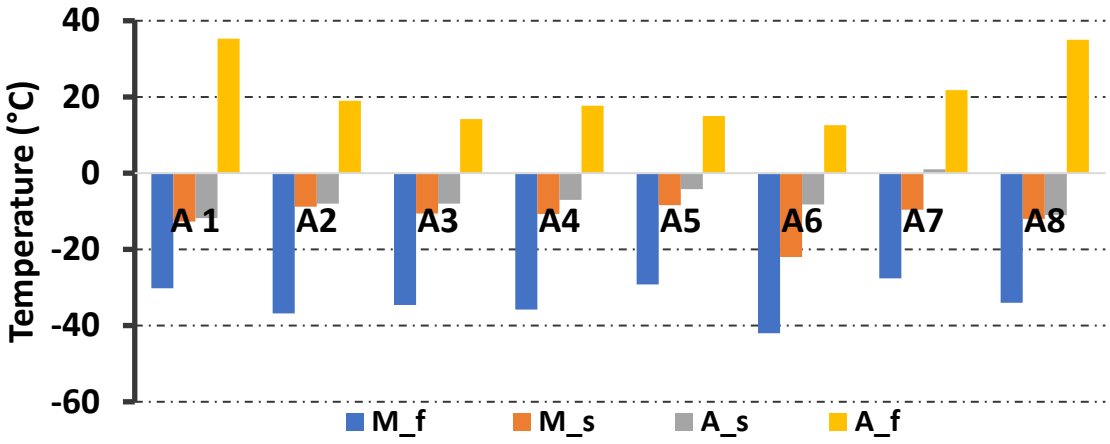

Figure 4-55 Transformation temperatures of the samples heat treated at different temperatures as well as the as built sample demonstrated on a bar chart.

Table 4.13 Transformation temperatures of the samples heat treated at different temperatures as well as the as built sample

Sample	Sample condition	M_f (°C)	M_s (°C)	A_s (°C)	A_f (°C)
A 1	700C-30m-F	-30.2	-12.7	-11.8	35.3
A2	700C-30m-W	-36.8	-8.8	-8	19
A3	700C-5.5h-W	-34.6	-10.6	-8	14.2
A4	850C-15m-W	-35.8	-10.7	-7	17.7
A5	950C-30m-W	-29.2	-8.4	-4.2	15
A6	950C-5.5h-F	-42	-22	-8.2	12.6
A7	950C-5.5h-W	-27.6	-9.6	1	21.8
A8	As built	-32.52	7.26	-5	35.3

Figure 4-56 shows the compression response of the heat-treated and as-built samples at Af+15. In order to remove the effect of working temperature on the thermomechanical response, all samples have been tested at 15°C above the austenite finish temperature. However, for a specific application, such as bone fixation plates, the mechanical properties must also be studied at body temperature. As it can be seen in Figure 4-56, by testing samples under 600MPa, different plateau levels, different strain recovery ratios, and even different values of Young's modulus were observed. These values are reported in Table 4.14 for each heat-treated sample as well as the as- built sample. In addition, since these values are strongly tied to the transformation temperatures, for a better demonstration, Figure 4-57, Figure 4-58, Figure 4-59, and Figure 4-60 graphically demonstrate the maximum strain, recovery ratio, plateau level, and Ea for each case, respectively. In order to select the optimized heat treatment procedure and understand its effects, all these characteristics must be considered.

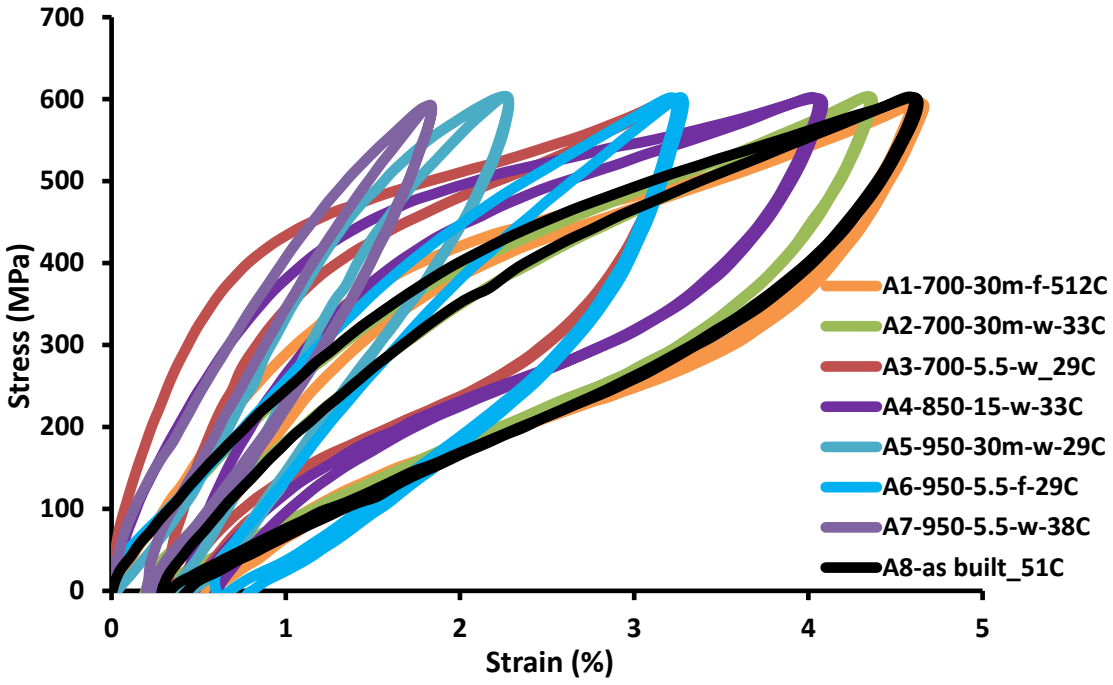

Figure 4-56 Compression response of the heat-treated and as-built samples at Af+15

Table 4.14 Thermomechanical behavior of the heat treated, and as-built samples tested at A_f+15, and under 600Mpa compression stress

sampl	M_f (°C)	M_s (°C)	A_s (°C)	A_f (°C)	A_f+15 (°C)	MAX strain	Irrecoverable strain	Recoverability Ratio	Plateau level (MPa)	Ea (GPa)
A 1	-30.2	-12.7	-11.8	35.3	50.3	4.66%	0.56%	87.98 %	385	31
A2	-36.8	-8.8	-8	19	34	4.35%	0.34%	92.18 %	345	24
A3	-34.6	-10.6	-8	14.2	29.2	3.25%	0.49%	84.92 %	410	50
A4	-35.8	-10.7	-7	17.7	32.7	4.08%	0.60%	85.29 %	450	41
A5	-29.2	-8.4	-4.2	15	30	2.28%	0.47%	79.39 %	480	40
A6	-42	-22	-8.2	12.6	27.6	3.28%	0.83%	74.70 %	385	24
A7	-27.6	-9.6	1	21.8	36.8	1.84 %	0.28%	84.78 %	480	36
A8	-32.52	7.26	-5	35.3	50	4.6%	0.44%	90.43 %	360	26

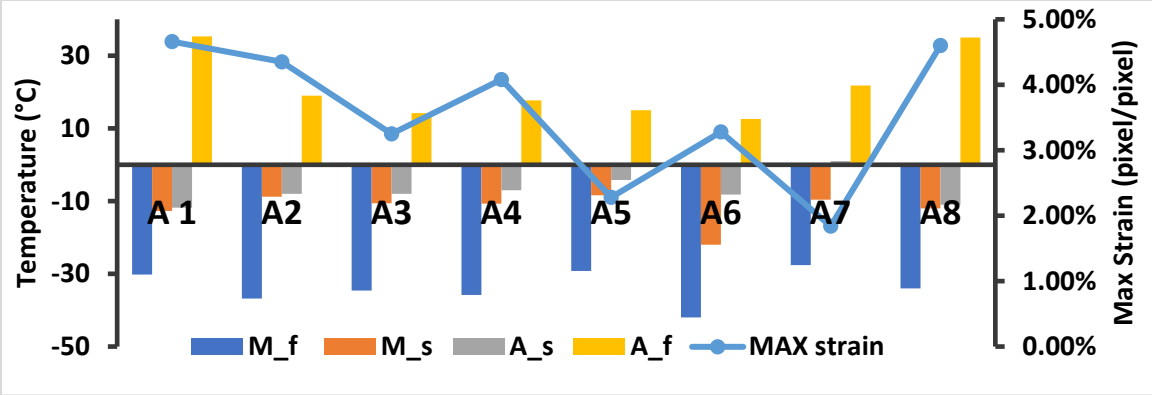

Figure 4-57 Maximum strain under 600 MPa compression stress for different cases of heat treatment as well as the as-built sample at A_f+15℃

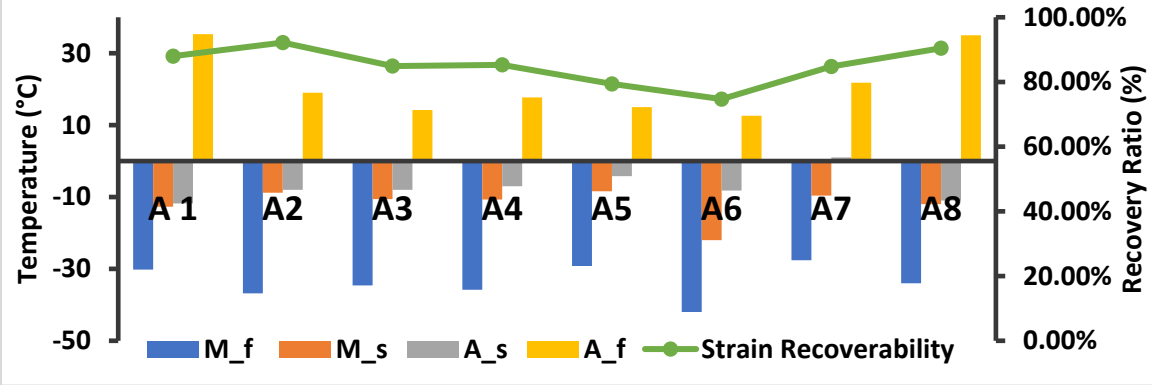

Figure 4-58 Recovery Ratio (%) under 600 MPa compression stress for different cases of heat treatment as well as the as-built sample at A_f+15℃ after stabilization

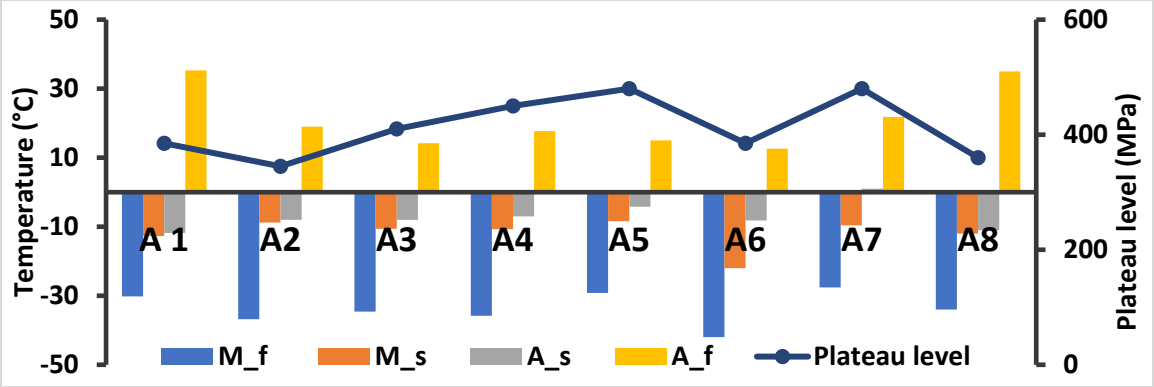

Figure 4-59 Plateau level (MPa) (initiation) under 600 MPa compression stress for different cases of heat treatment as well as the as-built sample at A_f+15°C

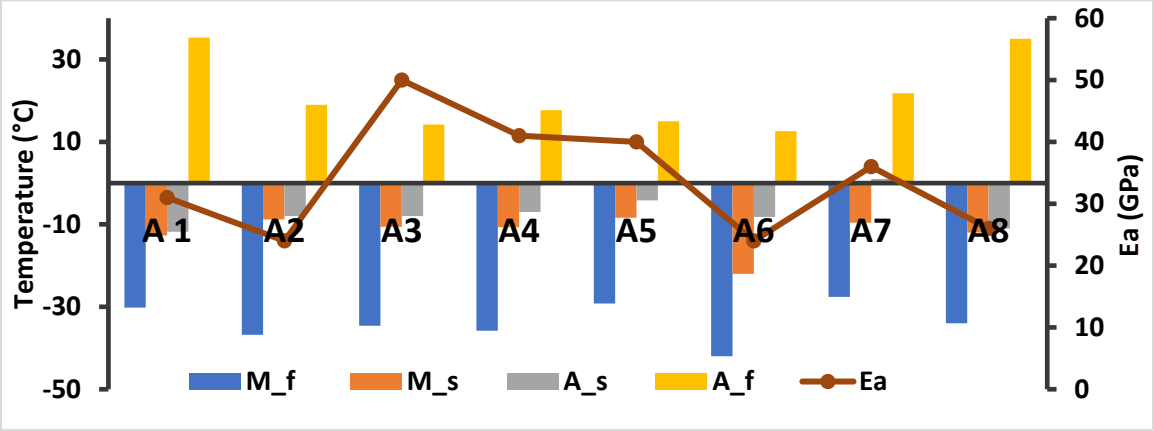

Figure 4-60 Austenite Young's modulus (E_a) under 600 MPa compression stress for different cases of heat treatment as well as the as-built sample at A_f+15°C

In order to fully understand the heat treatment mechanism and to verify its desired effects on the final part, metallurgical properties of the heat-treated samples should also be investigated. The reason is that most of the mechanical properties cannot be directly measured on the final part due to the complexities of the geometry and boundary conditions. One possible approach is to simplify the boundary condition and utilize a FE simulation model. Another practical approach is to investigate the microstructure and metallurgical features of the heat-treated parts and compare that with the reference samples. To this end, the metallurgical features of the heat-treated samples we also investigated in the next section.

4.7.7 Metallurgical features of the heat-treated samples

In order to investigate the metallurgical features of the heat treated parts, DSC and X-ray powder diffraction (XRD) can be used as the first steps. To this end, first the as-built part is analyzed and then the variations due to the heat treatment can be understood. Figure 4-61 shows the DSC results and the compression response of the as-built sample. This information should be used as the reference for the follow on fabrication. XRD results of the as-built sample is shown in Figure 4-62. As it can be seen, B2 picks can be recognized in the as-built sample and no major precipitates exist in the matrix.

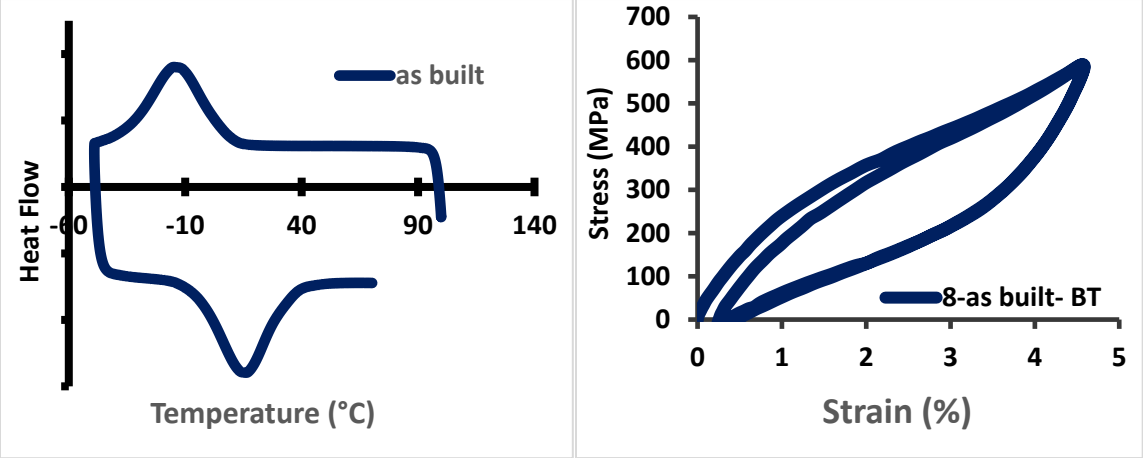

Figure 4-61 DSC and cyclic compression of the as-built sample under 600 MPa

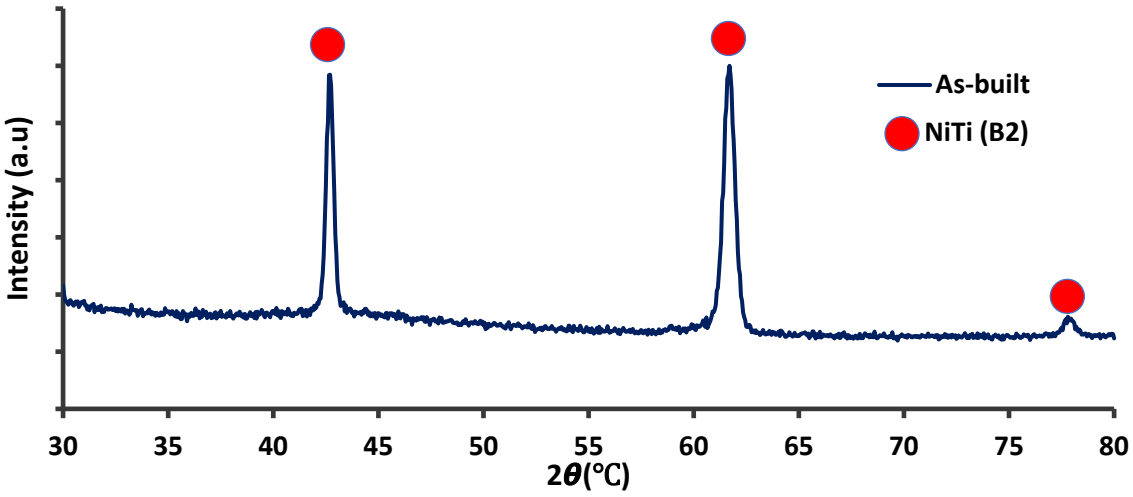

Figure 4-62 XRD results of the as-built sample

Figure 4-63 shows the XRD results of the heat-treated samples. As it can be seen, in addition to the B2 picks that were presented in as-built sample, several picks that can be associated to Ti2Ni can be distinguished in the results. These Ti-rich precipitates deplete the Ti from the alloy matrix and make the matrix more Ni-rich. This could be the reason associated with the decrease in the transformation temperatures of the heat-treated samples in comparison to the as built one. However, to verify the existence of the above-mentioned precipitated TEM analysis could be used as well, which is out of the scope of the current work. The main point is that the heat treatment process should be accompanied with proper microstructural analysis to verify the results. These microstructural analyses could include optical microscopy, SEM and TEM analysis, DSC, and XRD.

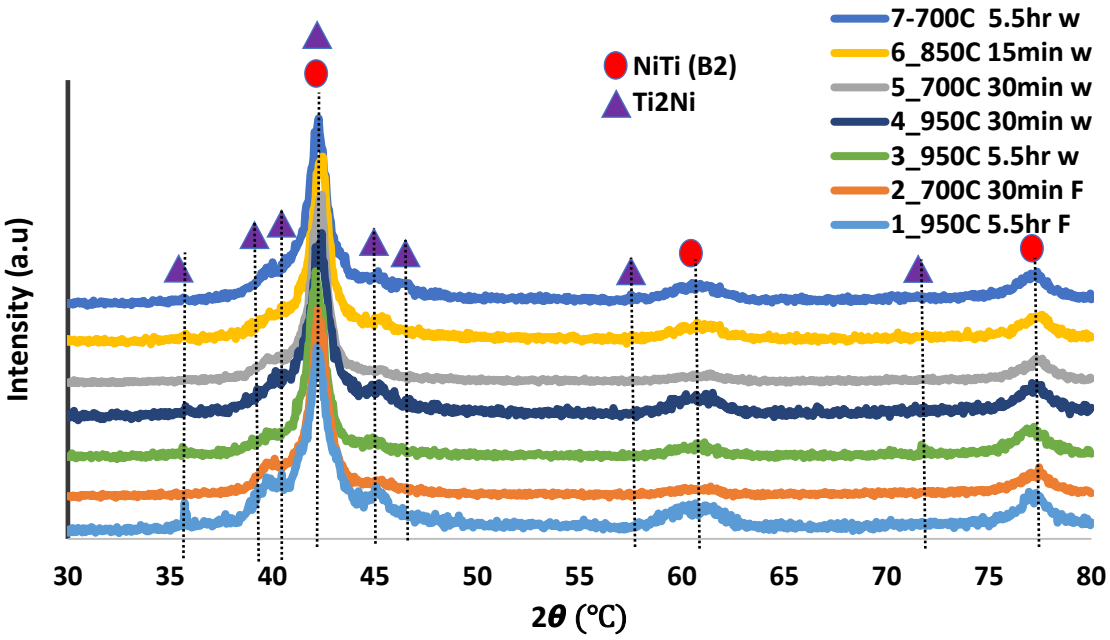

Figure 4-63 XRD analysis of the heat-treated samples

4.7.8 Mechanical response of the heat-treated parts at body temperature

Eventually since the parts are going to be used at body temperature, the mechanical properties at this temperature must be analyzed as well. Figure 4-64 shows the compression response of the heat-treated as well as the as-built sample at body temperature (i.e. 38℃). As it can be seen, in comparison with Figure 4-56, most of the parts, except the ones with A_f of about 20℃ (e.g. A2, A7, and A3) showed relatively different mechanical properties at body temperature. Therefore, it is critical to evaluate the mechanical properties at the working temperature (here the body temperature) as the most reliable source. However, if the tests cannot be conducted at the working temperature, by having access to C_a and C_m the mechanical response at other temperatures can be estimated using the phase diagram.

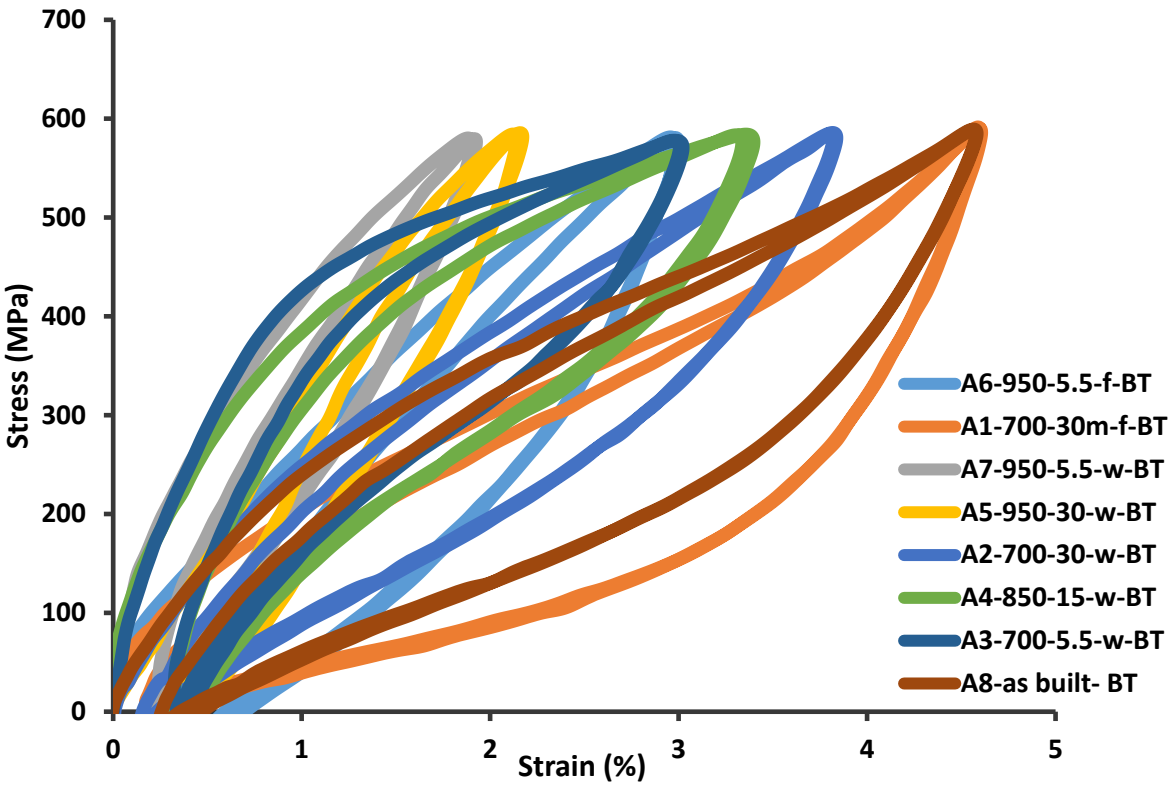

Figure 4-64 Mechanical response of the heat-treated samples under compression at 600MPa at body temperature

Chapter 5

5. Summary, conclusion, and future work

5.1 Summary

The standard of care for mandibular reconstruction surgery, uses titanium skeletal fixation plates and screws to stabilize the structure and facilitate the healing of engrafted bone. Although Titanium bone fixation plates provide high level of immobilization immediately after the surgery, they may cause stress shielding and lead to bone resorption after the bone healing. This is mainly due to the significant mismatch in their stiffness level with that of the bone tissue. After providing a comprehensive literature review on the mandibular reconstruction surgery, Nitinol, and additive manufacturing of Nitinol, we proposed stiffness modulated Nitinol bone fixation plates that can be fabricated via additive manufacturing as a solution to reduce the stress shielding effect and improve the mandibular reconstruction surgery.

Through finite element simulations, our group has previously shown that reducing the stiffness of the bone fixation plates to an engineered level, minimizes the stress shielding effect and the chance of failure in the mandibular reconstruction surgery. It was also shown that Nitinol exhibits specific mechanical properties that makes it a good

candidate for this application, and it can be fabricated via additive manufacturing. In this work, two realistic generations of stiffness-modulated bone fixation plates were designed fabricated and evaluated. Through the first generation, while having a simplified external and internal geometry (i.e. overall shape and the size of porosity) we showed the possibility of fabrication additive manufactured bone fixation plates with a modulated level of stiffness. The second generation of the stiffness modulated bone fixation plates were designed based on the conventional bone fixation plates with a realistic and extreme geometry created by micro CT scan of conventional skeletal fixation plate. The porosity size and features were also modified that can be used for the finer geometry. The second generation of the skeletal fixation plates were fabricated using a Ni-rich (i.e. Ni50.8Ti at. %) to improve the superelasticity. A chemical polishing methodology developed to remove the un-melted powder particles fused to the surfaces of the AM fabricated skeletal fixation plates. The polishing procedure is necessary to minimize the geometrical difference between the computer model and the fabricated parts and to improve the corrosion response and the biocompatibility. Thermomechanical properties of the as-built and polished skeletal fixation plates were then measured and verified the simulations.

Due to the nature of the selective laser melting procedure, fabricated parts may contain micro voids and pores that significantly affect the monotonic (especially tensile) and cyclic (e.g. fatigue life) properties. In addition, SLM fabricated parts usually have a rough surface due to the un-melted powder attached to the surfaces that also adversely affect the fatigue life. In an attempt to improve the density and surface condition, a relatively new approach called selective laser re-melting investigated on the AM parts.

The results show by proper selection of the re-melting parameters the relative density of the AM fabricated as well as the surface conditions improves.

Eventually, in order to improve the mechanical properties, superelastic response, homogenize the mechanical features, and to further modulate the mechanical properties, we performed a heat treatment study on the AM fabricated parts. Thermomechanical properties at A_f+15 as well as at body temperature were fully investigated and we showed that a wide range of mechanical properties can be achieved via heat treatment. Followed by measuring the thermomechanical response, microstructural features of the heat-treated samples were studied to further understand the heat treatment procedure and as an additional step to verify the desired outcome in cases were mechanical evaluation is not directly available.

5.2 Conclusion

In this dissertation, the concept of stiffness-modulated patient specific NiTi bone implants for mandibular reconstruction surgery that can be also used for other bone structures and in other metallic bone implants is fully investigated in a research stage. The goal was to investigate different aspects and challenges in this project and prepare the project for the commercialization stage. The project originally initiated back in 2013 by the two principal investigators, Dr. Mohammad Elahinia, Department chair and Professor at the Department of Mechanical, Industrial, and Manufacturing Engineering at The University of Toledo, and Dr. David Dean, Professor at the Department of Plastic & Reconstructive Surgery at The Ohio State University. Two master's theses [218, 245] were done on the initial stages to evaluate the feasibility and to provide the initial proof

of concept. This PhD dissertation aimed toward realistic NiTi 3D printed patient-specific, stiffness-modulated bone fixation plates.

Prior to this work, a comprehensive finite element model was prepared to simulate the maximum bite force on a healthy mandible and to calculate the stress and strain distribution in different regions. The same model was also further modified to simulate the case of reconstruction surgery, where a bone graft is resected from the mandible. In addition, required skeletal fixation plates and screws were also added to the model and the effect of skeletal fixation plate's stiffness via changing the Young's modulus was studied using finite element simulations. Eventually, the possibility of fabricating skeletal fixation plates using additive manufacturing (i.e. selective laser melting) was studied.

In this work, with a main focus on the manufacturing, the design procedure and simulations are reviewed and optimized for the additive manufacturing, the fabrication process is improved via change of the powder and modifying the process (e.g. use of re-melting), potential post processing techniques such as heat treatment and chemical polishing are investigated to improve the performance, and the final skeletal fixation plates are characterized in terms of thermomechanical properties and composition. With considering the final results, it can be concluded that the additive manufactured NiTi has the capacity to provide a safe, reliable, and functional solution for the bone implants. The use of NiTi beside additive manufacturing provide additional freedom and flexibility in reaching to a wide variety of thermomechanical properties. For instance, as suggested in the first stages of this project, introducing engineered porosity thanks to the additive manufacturing process enables one to provide implants with different levels of stiffness.

In addition to the flexibility provided by the additive manufacturing, due to the thermomechanical properties of NiTi, minor changes in the selective laser melting process (e.g. basic SLM process parameters such as laser power, scanning speed, hatch spacing, etc., raw material, or use of re-melting) as well as the post processing procedures (e.g. Heat treatment including, solution annealing and aging) lead to different thermomechanical properties. This additional flexibility enables engineers to design different thermomechanical properties using additive manufactured NiTi. However, at the same time additional complexities are added to the design and manufacturing procedures that require careful understanding of the whole procedure from the design to the post processing and finishing.

5.3 Future Work

We have shown that with the use of additive manufactured NiTi a new generation of bone fixation plates and other orthopedic implants can be developed and introduced to the biomedical industry. These implants may improve the surgeries mainly by reducing the stress shielding effect and by providing additional features such as shock absorption and superelasticity. However, there are some challenges, limitations, and optional improvements that should be addressed as the next steps of this project either as a research project or as a product development task.

The first series of limitation are related to the additive manufacturing and the fabrication procedure. It has been shown that with the current technology AM fabricated parts contain micro pores and voids that significantly affect the tensile properties and fatigue life of the components [246]. A potential project could be to evaluate the effect of these pores and voids on the AM fabricated parts and to optimize the fabrication

procedure to minimize these defects. Such optimizations could be achieved via modifying the scanning strategy, powder particles size, and other process parameters. In addition, some post processing techniques such as HIP (Hot Isostatic Pressing) may be utilized and investigated to improve the relative density and minimize the defects after the fabrications.

The other limitation related to the fabrication is the repeatability of the additive manufacturing technique. It is very common to recycle the powder used in a fabrication and re-use it for another set of fabrication. It has been shown that the reused powder may exhibit different process parameters that could be because of the impurity pickup or due to the temperature and other conditions in the build chamber. In this study we have neglected these variations and tried to minimize the difference by only using virgin powder (not reused) and by fabricating different samples in a single batch. However, the effect of these variations on the thermomechanical behavior of the fabricated parts as well as the required methods to minimize them must be carefully studied and understood. It should be mentioned this is not limited to Nitinol and is considered as a general limitation in AM. A practical solution is to come up with an acceptable interval for all the potential variables in the fabrication and make sure that the resultant features (e.g. thermomechanical properties, biocompatibilities, etc.) are safe and acceptable.

We have been able to reach to superelastic patient specific bone fixation plates with an engineered level of stiffness based on the patient's need. We have also studied two mechanisms to improve the thermomechanical properties: re-melting and heat treatment. However, the combination of these three processes including the SLM process, re-melting, and heat treatment method should be further studied and incorporated to

improve the thermomechanical properties and especially the fatigue life. It is expected to observe a fatigue life increase in the re-melted samples due to the increase in the relative density of the parts. There is also a lack of reliable fatigue data for the Am fabricated NiTi parts at body temperature. These items may be investigated in a product development stage or as a research work.

References

[1] M. Bahraminasab, and A. Jahan, “Material selection for femoral component of total knee replacement using comprehensive VIKOR,” *Materials Design,* vol. 32, no. 8-9, pp. 4471-4477, 2011.

[2] Y. Okazaki, E. Gotoh, T. Manabe, and K. Kobayashi, “Comparison of metal concentrations in rat tibia tissues with various metallic implants,” *Biomaterials,* vol. 25, no. 28, pp. 5913-5920, 2004.

[3] D. F. Williams, “On the mechanisms of biocompatibility,” *Biomaterials,* vol. 29, no. 20, pp. 2941-2953, 2008.

[4] M. H. Elahinia, M. Hashemi, M. Tabesh, and S. B. Bhaduri, “Manufacturing and processing of NiTi implants: A review,” *Progress in materials science,* vol. 57, no. 5, pp. 911-946, 2012.

[5] H. H. Bayraktar, E. F. Morgan, G. L. Niebur, G. E. Morris, E. K. Wong, and T. M. Keaveny, “Comparison of the elastic and yield properties of human femoral trabecular and cortical bone tissue,” *Journal of biomechanics,* vol. 37, no. 1, pp. 27-35, 2004.

[6] M. Bahraminasab, and B. B. Sahari, "NiTi shape memory alloys, promising materials in orthopedic applications," *Shape Memory Alloys-Processing, Characterization and Applications*: InTech, 2013.

[7] N. S. Moghaddam, R. Skoracki, M. Miller, M. Elahinia, and D. Dean, “Three dimensional printing of stiffness-tuned, nitinol skeletal fixation hardware with an example of mandibular segmental defect repair,” *Procedia CIRP,* vol. 49, pp. 45-50, 2016.

[8] A. Jahadakbar, N. Shayesteh Moghaddam, A. Amerinatanzi, D. Dean, H. E. Karaca, and M. Elahinia, “Finite element simulation and additive manufacturing of stiffness-matched niti fixation hardware for mandibular reconstruction surgery,” *Bioengineering,* vol. 3, no. 4, pp. 36, 2016.

[9] H. Ibrahim, A. Jahadakbar, A. Dehghan, N. S. Moghaddam, A. Amerinatanzi, and M. Elahinia, “In Vitro Corrosion Assessment of Additively Manufactured Porous NiTi Structures for Bone Fixation Applications,” *Metals,* vol. 8, no. 3, pp. 164, 2018.

[10] A. Jahadakbar, M. Nematollahi, K. Safaei, P. Bayati, G. Giri, H. Dabbaghi, D. Dean, and M. Elahinia, “Design, Modeling, Additive Manufacturing, and Polishing of Stiffness-Modulated Porous Nitinol Bone Fixation Plates Followed by Thermomechanical and Composition Analysis,” *Metals,* vol. 10, no. 1, pp. 151, 2020.

[11] A. Amerinatanzi, N. Shayesteh Moghaddam, A. Jahadakbar, D. Dean, and M. Elahinia, "On the effect of screw preload on the stress distribution of mandibles during segmental defect treatment using an additively manufactured hardware."

[12] N. S. Moghaddam, A. Jahadakbar, M. Elahinia, D. Dean, and M. Miller, "The effect of adding dental implants to the reconstructed mandible comparing the effect of using Ti-6Al-4V and NiTi hardware." pp. S398-S398.

[13] A. Jahadakbar, N. S. Moghaddam, A. Amerinatanzi, D. Dean, and M. Elahinia, "Mechanical evaluation of the SLM fabricated, stiffness-matched, mandibular bone fixation plates." p. 1059610.

[14] N. Shayesteh Moghaddam, A. Jahadakbar, A. Amerinatanzi, R. Skoracki, M. Miller, D. Dean, and M. Elahinia, "Fixation release and the bone bandaid: A new bone fixation device paradigm," *Bioengineering,* vol. 4, no. 1, pp. 5, 2017.

[15] A. Jahadakbar, N. Shayesteh Moghaddam, A. Amerinatanzi, D. Dean, H. E. Karaca, and M. Elahinia, "Finite element simulation and additive manufacturing of stiffness-matched niti fixation hardware for mandibular reconstruction surgery," *J Bioengineering,* vol. 3, no. 4, pp. 36, 2016.

[16] Z. L. Wang, and Z. C. Kang, "FUNCTIONAL AND SMART MATERIALS-Structural evolution and structure analysis," Academic press: Peking, China, 2002.

[17] G. P. Toker, M. Nematollahi, S. E. Saghaian, K. S. Baghbaderani, O. Benafan, M. Elahinia, and H. E. Karaca, "Shape memory behavior of NiTiHf alloys fabricated by selective laser melting," *Scripta Materialia,* vol. 178, pp. 361-365, 2020.

[18] D. C. Lagoudas, *Shape memory alloys: modeling and engineering applications*: Springer, 2008.

[19] M. Nematollahi, K. S. Baghbaderani, A. Amerinatanzi, H. Zamanian, and M. Elahinia, "Application of NiTi in assistive and rehabilitation devices: a review," *Bioengineering,* vol. 6, no. 2, pp. 37, 2019.

[20] E. Parsai, D. Elliott, P. Bayatimalayeri, and M. Elahinia, "Rectal Retractor, A Novel Device for Sparing Rectum in Radiotherapy Applications of Pelvic Tumors." pp. E199-E199.

[21] E. I. Parsai, A. Jahadakbar, H. Lavvafi, and M. Elahinia, "A novel and innovative device to retract rectum during radiation therapy of pelvic tumors," *Journal of applied clinical medical physics,* vol. 20, no. 1, pp. 194-199, 2019.

[22] P. B. Malayeri, A. Jahadakbar, D. Elliottt, M. Elahinia, and E. Parsai, "A Novel Device to Retract Rectum During Radiotherapy Applications of Pelvic Tumors." pp. E665-E665.

[23] A. Amerinatanzi, H. Zamanian, N. Shayesteh Moghaddam, A. Jahadakbar, and M. Elahinia, "Application of the superelastic NiTi spring in ankle foot orthosis (AFO) to create normal ankle joint behavior," *Bioengineering,* vol. 4, no. 4, pp. 95, 2017.

[24] K. Bhattacharya, *Microstructure of martensite: why it forms and how it gives rise to the shape-memory effect*: Oxford University Press, 2003.

[25] C. Mavroidis, C. Pfeiffer, and M. Mosley, "5.1 conventional actuators, shape memory alloys, and electrorheological fluids," *Automation, miniature robotics, sensors for nondestructive testing evaluation,* vol. 4, pp. 189, 2000.

[26] A. Ölander, "The crystal structure of AuCd," *Zeitschrift für Kristallographie-Crystalline Materials,* vol. 83, no. 1-6, pp. 145-148, 1932.

[27] A. Ölander, "An electrochemical investigation of solid cadmium-gold alloys," *Journal of the American Chemical Society,* vol. 54, no. 10, pp. 3819-3833, 1932.

[28] A. B. GRENINGER, and V. Mooradian, “Strain transformation in metastable beta copper-zinc and beta copper-Ti alloys,” *AIME TRANS,* vol. 128, pp. 337-369, 1938.

[29] G. Kurdyumov, and L. Khandros, "On the thermoelastic equilibrium on martensitic transformations." pp. 211-214.

[30] C. M. Wayman, and J. D. Harrison, “The origins of the shape memory effect,” *Jom,* vol. 41, no. 9, pp. 26-28, 1989.

[31] W. Buehler, and R. Wiley, *The properties of TiNi and associated phases*, NAVAL ORDNANCE LAB WHITE OAK MD, 1961.

[32] W. J. Buehler, and R. C. Wiley, "Nickel-base alloys," Google Patents, 1965.

[33] W. J. Buehler, and F. E. Wang, “A summary of recent research on the Nitinol alloys and their potential application in ocean engineering,” *Ocean Engineering,* vol. 1, no. 1, pp. 105-120, 1968.

[34] G. B. Kauffman, and I. Mayo, “The story of nitinol: the serendipitous discovery of the memory metal and its applications,” *The chemical educator,* vol. 2, no. 2, pp. 1-21, 1997.

[35] K. Otsuka, and K. Shimizu, “Memory effect and thermoelastic martensite transformation in Cu□ Al□ Ni alloy,” *Scripta metallurgica,* vol. 4, no. 6, pp. 469-472, 1970.

[36] T. Saburi, and S. Nenno, “The shape memory effect and related phenomena,” *Solid to solid phase transformations*, pp. 1455-1479, 1981.

[37] T. Saburi, C. Wayman, K. Takata, and S. Nenno, “The shape memory mechanism in 18R martensitic alloys,” *Acta Metallurgica,* vol. 28, no. 1, pp. 15-32, 1980.

[38] K. Otsuka, C. Wayman, K. Nakai, H. Sakamoto, and K. Shimizu, “Superelasticity effects and stress-induced martensitic transformations in Cu□ Al□ Ni alloys,” *Acta Metallurgica,* vol. 24, no. 3, pp. 207-226, 1976.

[39] K. Otsuka, H. Sakamoto, and K. Shimizu, “Successive stress-induced martensitic transformations and associated transformation pseudoelasticity in Cu-Al-Ni alloys,” *Acta Metallurgica,* vol. 27, no. 4, pp. 585-601, 1979.

[40] S. Miyazaki, and K. Otsuka, “Development of shape memory alloys,” *Isij International,* vol. 29, no. 5, pp. 353-377, 1989.

[41] T. Duerig, A. Pelton, and D. Stöckel, “An overview of nitinol medical applications,” *Materials Science Engineering: A,* vol. 273, pp. 149-160, 1999.

[42] T. Duerig, D. Tolomeo, and M. Wholey, “An overview of superelastic stent design,” *Minimally Invasive Therapy Allied Technologies,* vol. 9, no. 3-4, pp. 235-246, 2000.

[43] T. Duerig, “Present and future applications of shape memory and superelastic materials,” *MRS Online Proceedings Library Archive,* vol. 360, 1994.

[44] A. D. Johnson, V. Martynov, and V. Gupta, "Applications of shape memory alloys: advantages, disadvantages, and limitations." pp. 341-352.

[45] K. Otsuka, and T. Kakeshita, “Science and technology of shape-memory alloys: new developments,” *mrs bulletin,* vol. 27, no. 2, pp. 91-100, 2002.

[46] K. Otsuka, and X. Ren, “Physical metallurgy of Ti–Ni-based shape memory alloys,” *Progress in materials science,* vol. 50, no. 5, pp. 511-678, 2005.

[47] K. F. Hane, and T. Shield, “Microstructure in the cubic to monoclinic transition in titanium–nickel shape memory alloys,” *Acta materialia,* vol. 47, no. 9, pp. 2603-2617, 1999.

[48] H. C. Ling, and R. Kaplow, “Phase transitions and shape memory in NiTi,” *Metallurgical Materials Transactions A,* vol. 11, no. 1, pp. 77-83, 1980.

[49] K. Parlinski, and M. Parlinska-Wojtan, “Lattice dynamics of NiTi austenite, martensite, and R phase,” *Physical Review B,* vol. 66, no. 6, pp. 064307, 2002.

[50] X. Zhang, and H. Sehitoglu, “Crystallography of the B2→ R→ B19′ phase transformations in NiTi,” *Materials Science Engineering: A,* vol. 374, no. 1-2, pp. 292-302, 2004.

[51] S. Padula, S. Qiu, D. Gaydosh, R. Noebe, G. Bigelow, A. Garg, and R. Vaidyanathan, “Effect of upper-cycle temperature on the load-biased, strain-temperature response of NiTi,” *Metallurgical and Materials Transactions A,* vol. 43, no. 12, pp. 4610-4621, 2012.

[52] H. Meier, C. Haberland, J. Frenzel, and R. Zarnetta, "Selective Laser Melting of NiTi shape memory components," *Innovative Developments in Design and Manufacturing*, pp. 251-256: CRC Press, 2009.

[53] W. Tang, “Thermodynamic study of the low-temperature phase B19′ and the martensitic transformation in near-equiatomic Ti-Ni shape memory alloys,” *Metallurgical and materials transactions A,* vol. 28, no. 3, pp. 537-544, 1997.

[54] M. Nishida, C. M. Wayman, and T. Honma, “Precipitation processes in near-equiatomic TiNi shape memory alloys,” *Metallurgical Transactions A,* vol. 17, no. 9, pp. 1505-1515, 1986.

[55] K. Melton, and O. Mercier, “The mechanical properties of NiTi-based shape memory alloys,” *Acta Metallurgica,* vol. 29, no. 2, pp. 393-398, 1981.

[56] J. Ma, I. Karaman, and R. D. Noebe, “High temperature shape memory alloys,” *International Materials Reviews,* vol. 55, no. 5, pp. 257-315, 2010.

[57] G. Firstov, J. Van Humbeeck, and Y. N. Koval, “High-temperature shape memory alloys: some recent developments,” *Materials Science Engineering: A,* vol. 378, no. 1-2, pp. 2-10, 2004.

[58] H. Horikawa, K. Shiroyama, and K. Mitose, "Niti-type medical guide wire and method of producing the same," Google Patents, 2003.

[59] N. S. Moghaddam, S. Saedi, A. Amerinatanzi, E. Saghaian, A. Jahadakbar, H. Karaca, and M. Elahinia, "Selective laser melting of Ni-rich NiTi: selection of process parameters and the superelastic response." p. 105960W.

[60] J. Zhang, W. Cai, X. Ren, K. Otsuka, and M. Asai, “The nature of reversible change in Ms temperatures of Ti–Ni alloys with alternating aging,” *Materials Transactions, JIM,* vol. 40, no. 12, pp. 1367-1375, 1999.

[61] A. R. Pelton, J. Dicello, and S. Miyazaki, “Optimisation of processing and properties of medical grade Nitinol wire,” *Minimally Invasive Therapy Allied Technologies,* vol. 9, no. 2, pp. 107-118, 2000.

[62] H. Funakubo, and J. Kennedy, *Shape memory alloys*: Gordon and Breach, 1987.

[63] T. Yoneyama, and S. Miyazaki, *Shape memory alloys for biomedical applications*: Elsevier, 2008.

[64] G. Fan, W. Chen, S. Yang, J. Zhu, X. Ren, and K. Otsuka, "Origin of abnormal multi-stage martensitic transformation behavior in aged Ni-rich Ti–Ni shape memory alloys," *Acta Materialia,* vol. 52, no. 14, pp. 4351-4362, 2004.

[65] M. H. Elahinia, *Shape memory alloy actuators: design, fabrication, and experimental evaluation*: John Wiley & Sons, 2016.

[66] S. Lacy, K. Merritt, S. Brown, and A. Puryear, "Distribution of nickel and cobalt following dermal and systemic administration with in vitro and in vivo studies," *Journal of Biomedical Materials Research: An Official Journal of The Society for Biomaterials The Japanese Society for Biomaterials* vol. 32, no. 2, pp. 279-283, 1996.

[67] R. A. Goyer, and T. W. Clarkson, "Toxic effects of metals," *Casarett and Doull's Toxicology. The Basic Science of Poisons, Fifth Edition, Klaassen, CD . McGraw-Hill Health Professions Division,,* vol. 71054766, 1996.

[68] R. B. Hayes, "The carcinogenicity of metals in humans," *Cancer Causes Control,* vol. 8, no. 3, pp. 371-385, 1997.

[69] L. Peltonen, "Nickel sensitivity in the general population," *Contact Dermatitis,* vol. 5, no. 1, pp. 27-32, 1979.

[70] P. G. Laing, A. B. Ferguson Jr, and E. S. Hodge, "Tissue reaction in rabbit muscle exposed to metallic implants," *Journal of biomedical materials research,* vol. 1, no. 1, pp. 135-149, 1967.

[71] S. A. Brown, P. J. Hughes, and K. Merritt, "In vitro studies of fretting corrosion of orthopaedic materials," *Journal of orthopaedic research,* vol. 6, no. 4, pp. 572-579, 1988.

[72] K. M. Speck, and A. C. Fraker, "Anodic polarization behavior of Ti-Ni and Ti-6A 1-4 V in simulated physiological solutions," *Journal of Dental Research,* vol. 59, no. 10, pp. 1590-1595, 1980.

[73] R. Hultgren, P. D. Desai, D. T. Hawkins, M. Gleiser, and K. K. Kelley, *Selected values of the thermodynamic properties of binary alloys*, National Standard Reference Data System, 1973.

[74] C. Trepanier, M. Tabrizian, L. H. Yahia, L. Bilodeau, and D. L. Piron, "Effect of modification of oxide layer on NiTi stent corrosion resistance," *Journal of biomedical materials research,* vol. 43, no. 4, pp. 433-440, 1998.

[75] D. Wever, A. Veldhuizen, J. De Vries, H. Busscher, D. Uges, and J. Van Horn, "Electrochemical and surface characterization of a nickel–titanium alloy," *Biomaterials,* vol. 19, no. 7-9, pp. 761-769, 1998.

[76] D. E. Cutright, S. N. Bhaskar, B. Perez, R. M. Johnson, and G. S. Cowan, "Tissue reaction to nitinol wire alloy," *Oral Surgery, Oral Medicine, Oral Pathology and Oral Radiology,* vol. 35, no. 4, pp. 578-584, 1973.

[77] L. Castleman, S. Motzkin, F. Alicandri, V. Bonawit, and A. Johnson, "Biocompatibility of nitinol alloy as an implant material," *Journal of biomedical materials research,* vol. 10, no. 5, pp. 695-731, 1976.

[78] P. Filip, J. Lausmaa, J. Musialek, and K. Mazanec, "Structure and surface of TiNi human implants," *Biomaterials,* vol. 22, no. 15, pp. 2131-2138, 2001.

[79] M. Berger-Gorbet, B. Broxup, C. Rivard, and L. H. Yahia, "Biocompatibility testing of NiTi screws using immunohistochemistry on sections containing metallic implants," *Journal of Biomedical Materials Research: An Official*

Journal of The Society for Biomaterials and The Japanese Society for Biomaterials, vol. 32, no. 2, pp. 243-248, 1996.

[80] F. Takeshita, H. Takata, Y. Ayukawa, and T. Suetsugu, "Histomorphometric analysis of the response of rat tibiae to shape memory alloy (nitinol)," *Biomaterials,* vol. 18, no. 1, pp. 21-25, 1997.

[81] J. Ryhänen, M. Kallioinen, W. Serlo, P. Perämäki, J. Junila, P. Sandvik, E. Niemelä, and J. Tuukkanen, "Bone healing and mineralization, implant corrosion, and trace metals after nickel–titanium shape memory metal intramedullary fixation," *Journal of Biomedical Materials Research: An Official Journal of The Society for Biomaterials, The Japanese Society for Biomaterials, The Australian Society for Biomaterials and the Korean Society for Biomaterials,* vol. 47, no. 4, pp. 472-480, 1999.

[82] J. Ryhänen, M. Kallioinen, J. Tuukkanen, P. Lehenkari, J. Junila, E. Niemelä, P. Sandvik, and W. Serlo, "Bone modeling and cell–material interface responses induced by nickel–titanium shape memory alloy after periosteal implantation," *Biomaterials,* vol. 20, no. 14, pp. 1309-1317, 1999.

[83] R. Ayers, S. Simske, T. Bateman, A. Petkus, R. Sachdeva, and V. Gyunter, "Effect of nitinol implant porosity on cranial bone ingrowth and apposition after 6 weeks," *Journal of Biomedical Materials Research: An Official Journal of The Society for Biomaterials, The Japanese Society for Biomaterials, The Australian Society for Biomaterials,* vol. 45, no. 1, pp. 42-47, 1999.

[84] S. Simske, and R. Sachdeva, “Cranial bone apposition and ingrowth in a porous nickel–titanium implant,” *Journal of biomedical materials research,* vol. 29, no. 4, pp. 527-533, 1995.

[85] S. Rhalmi, M. Odin, M. Assad, M. Tabrizian, C. Rivard, and L. H. Yahia, “Hard, soft tissue and in vitro cell response to porous nickel-titanium: A biocompatibility evaluation,” *Bio-medical materials engineering,* vol. 9, no. 3, pp. 151-162, 1999.

[86] S.-B. Kang, K.-S. Yoon, and J.-S. Kim, "In vivo result of porous nitinol shape memory alloy: bone response and growth." p. 2000.

[87] M. Assad, P. Jarzem, M. A. Leroux, C. Coillard, A. V. Chernyshov, S. Charette, and C. H. Rivard, “Porous titanium-nickel for intervertebral fusion in a sheep model: Part 1. Histomorphometric and radiological analysis1,” *Journal of Biomedical Materials Research Part B: Applied Biomaterials: An Official Journal of The Society for Biomaterials, The Japanese Society for Biomaterials, The Australian Society for Biomaterials the Korean Society for Biomaterials,* vol. 64, no. 2, pp. 107-120, 2003.

[88] M. Assad, A. Chernyshov, P. Jarzem, M. Leroux, C. Coillard, S. Charette, and C. Rivard, “Porous titanium-nickel for intervertebral fusion in a sheep model: Part 2. Surface analysis and nickel release assessment,” *Journal of Biomedical Materials Research Part B: Applied Biomaterials: An Official Journal of The Society for Biomaterials, The Japanese Society for Biomaterials, The Australian Society for Biomaterials the Korean Society for Biomaterials,* vol. 64, no. 2, pp. 121-129, 2003.

[89] S. A. Shabalovskaya, "Surface, corrosion and biocompatibility aspects of Nitinol as an implant material," *Bio-medical materials and engineering,* vol. 12, no. 1, pp. 69-109, 2002.

[90] S. Kujala, J. Ryhänen, A. Danilov, and J. Tuukkanen, "Effect of porosity on the osteointegration and bone ingrowth of a weight-bearing nickel–titanium bone graft substitute," *Biomaterials,* vol. 24, no. 25, pp. 4691-4697, 2003.

[91] S. Wu, X. Liu, Y. Chan, J. Ho, C. Chung, P. K. Chu, C. Chu, K. Yeung, W. Lu, and K. Cheung, "Nickel release behavior, cytocompatibility, and superelasticity of oxidized porous single-phase NiTi," *Journal of Biomedical Materials Research Part A,* vol. 81, no. 4, pp. 948-955, 2007.

[92] A. Bansiddhi, T. Sargeant, S. Stupp, and D. Dunand, "Porous NiTi for bone implants: a review," *Acta biomaterialia,* vol. 4, no. 4, pp. 773-782, 2008.

[93] N. Munroe, C. Pulletikurthi, and W. Haider, "Enhanced biocompatibility of porous nitinol," *Journal of materials engineering performance,* vol. 18, no. 5-6, pp. 765-767, 2009.

[94] O. Prymak, D. Bogdanski, M. Köller, S. A. Esenwein, G. Muhr, F. Beckmann, T. Donath, M. Assad, and M. Epple, "Morphological characterization and in vitro biocompatibility of a porous nickel–titanium alloy," *Biomaterials,* vol. 26, no. 29, pp. 5801-5807, 2005.

[95] D. Hodgson, and S. Russell, "Nitinol melting, manufacture and fabrication," *Minimally Invasive Therapy Allied Technologies,* vol. 9, no. 2, pp. 61-65, 2000.

[96] H. Lin, K. Lin, and Y. Chen, "A study on the machining characteristics of TiNi shape memory alloys," *Journal of materials processing technology,* vol. 105, no. 3, pp. 327-332, 2000.

[97] K. Weinert, and V. Petzoldt, "Machining of NiTi based shape memory alloys," *Materials Science Engineering: A,* vol. 378, no. 1-2, pp. 180-184, 2004.

[98] S. Wu, H. Lin, and C. Chen, "A study on the machinability of a Ti49. 6Ni50. 4 shape memory alloy," *Materials Letters,* vol. 40, no. 1, pp. 27-32, 1999.

[99] M. Kong, D. Axinte, and W. Voice, "Challenges in using waterjet machining of NiTi shape memory alloys: An analysis of controlled-depth milling," *Journal of Materials Processing Technology,* vol. 211, no. 6, pp. 959-971, 2011.

[100] D. R. Askeland, and P. P. Phulé, *The science and engineering of materials*: Springer, 2003.

[101] C. Craciunescu, R. Miranda, R. Silva, E. Assuncao, and F. B. Fernandes, "Laser beam interaction with Ni–Mn–Ga ferromagnetic shape memory alloys," *Optics Lasers in Engineering,* vol. 49, no. 11, pp. 1289-1293, 2011.

[102] S. Chen, S. Hsieh, H. Lin, M. Lin, and J. Huang, "Electrical discharge machining of a NiAlFe ternary shape memory alloy," *Journal of alloys compounds,* vol. 464, no. 1-2, pp. 446-451, 2008.

[103] F. Han, J. Jiang, and D. Yu, "Influence of discharge current on machined surfaces by thermo-analysis in finish cut of WEDM," *International Journal of Machine Tools and Manufacture,* vol. 47, no. 7-8, pp. 1187-1196, 2007.

[104] M. Manjaiah, S. Narendranath, and S. Basavarajappa, “Review on non-conventional machining of shape memory alloys,” *Transactions of Nonferrous Metals Society of China,* vol. 24, no. 1, pp. 12-21, 2014.

[105] M. Taheri Andani, C. Haberland, J. M. Walker, M. Karamooz, A. Sadi Turabi, S. Saedi, R. Rahmanian, H. Karaca, D. Dean, and M. Kadkhodaei, “Achieving biocompatible stiffness in NiTi through additive manufacturing,” *Journal of Intelligent Material Systems Structures,* vol. 27, no. 19, pp. 2661-2671, 2016.

[106] B.-Y. Li, L.-J. Rong, and Y.-Y. Li, “Porous NiTi alloy prepared from elemental powder sintering,” *Journal of materials research,* vol. 13, no. 10, pp. 2847-2851, 1998.

[107] Y. Zhao, M. Taya, Y. Kang, and A. Kawasaki, “Compression behavior of porous NiTi shape memory alloy,” *Acta materialia,* vol. 53, no. 2, pp. 337-343, 2005.

[108] C. Zanotti, P. Giuliani, A. Terrosu, S. Gennari, and F. Maglia, “Porous Ni–Ti ignition and combustion synthesis,” *Intermetallics,* vol. 15, no. 3, pp. 404-412, 2007.

[109] M. Bram, A. Ahmad-Khanlou, A. Heckmann, B. Fuchs, H. Buchkremer, and D. Stöver, “Powder metallurgical fabrication processes for NiTi shape memory alloy parts,” *Materials Science Engineering: A,* vol. 337, no. 1-2, pp. 254-263, 2002.

[110] E. Aust, W. Limberg, R. Gerling, B. Oger, and T. Ebel, “Advanced TiAl6Nb7 bone screw implant fabricated by metal injection moulding,” *Advanced Engineering Materials,* vol. 8, no. 5, pp. 365-370, 2006.

[111] M. H. Wu, "Fabrication of nitinol materials and components." pp. 285-292.

[112] C. Haberland, and M. H. Elahinia, "Fabricating NiTi SMA Components," *Shape Memory Alloy Actuators: Design, Fabrication and Experimental Evaluation,* vol. 191, 2015.

[113] T. AYDOĞMUŞ, and A. Ş. BOR, "Production and characterization of porous TiNi shape memory alloys," *Turkish Journal of Engineering Environmental Sciences,* vol. 35, no. 2, pp. 69-82, 2011.

[114] G. S. Upadhyaya, *Powder metallurgy technology*: Cambridge Int Science Publishing, 1997.

[115] L. E. Penrod, "Fabrication and characterization of porous shape memory alloys," Texas A&M University, 2004.

[116] J. Li, F. Chen, Q. Shen, H. Jiang, and L. Zhang, "Fabrication and dielectric properties of Si3N4–MgO–Al2O3 by spark plasma sintering technique," *J Mater Sci–Poland,* vol. 25, pp. 699-707, 2007.

[117] J. Mentz, M. Bram, H. P. Buchkremer, and D. Stöver, "Improvement of mechanical properties of powder metallurgical NiTi shape memory alloys," *Advanced engineering materials,* vol. 8, no. 4, pp. 247-252, 2006.

[118] R. M. German, *Powder metallurgy and particulate materials processing: the processes, materials, products, properties, and applications*: Metal powder industries federation Princeton, 2005.

[119] W. E. Frazier, "Metal additive manufacturing: a review," *Journal of Materials Engineering and Performance,* vol. 23, no. 6, pp. 1917-1928, 2014.

[120] C. K. Chua, K. F. Leong, and C. S. Lim, *Rapid prototyping: principles and applications*: World Scientific, 2003.

[121] M. Namatollahi, A. Jahadakbar, M. J. Mahtabi, and M. Elahinia, "Additive manufacturing (AM)," *Metals for Biomedical Devices*, pp. 331-353: Elsevier, 2019.

[122] N. S. Moghaddam, A. Jahadakbar, A. Amerinatanzi, and M. Elahinia, "Recent advances in laser-based additive manufacturing," *Laser-Based Additive Manufacturing of Metal Parts*, pp. 1-24: CRC Press, 2017.

[123] J. J. Beaman, J. W. Barlow, D. L. Bourell, R. H. Crawford, H. L. Marcus, and K. P. McAlea, "Solid freeform fabrication: a new direction in manufacturing," *Kluwer Academic Publishers, Norwell, MA,* vol. 2061, pp. 25-49, 1997.

[124] L. Lü, J. Fuh, and Y.-S. Wong, *Laser-induced materials and processes for rapid prototyping*: Springer Science & Business Media, 2013.

[125] N. S. Moghaddam, A. Jahadakbar, A. Amerinatanzi, and M. Elahinia, "Recent Advances in Laser-Based Additive Manufacturing," *Laser-Based Additive Manufacturing of Metal Parts: Modeling, Optimization, Control of Mechanical Properties*, 2017.

[126] F. Likibi, M. Assad, P. Jarzem, M. A. Leroux, C. Coillard, G. Chabot, and C.-H. Rivard, "Osseointegration study of porous nitinol versus titanium orthopaedic implants," *European Journal of Orthopaedic Surgery Traumatology,* vol. 14, no. 4, pp. 209-213, 2004.

[127] V. Bhavar, P. Kattire, V. Patil, S. Khot, K. Gujar, and R. Singh, "A review on powder bed fusion technology of metal additive manufacturing." pp. 1-2.

[128] M. Elahinia, N. S. Moghaddam, M. T. Andani, A. Amerinatanzi, B. A. Bimber, and R. F. Hamilton, “Fabrication of NiTi through additive manufacturing: A review,” *Progress in Materials Science,* vol. 83, pp. 630-663, 2016.

[129] C. Haberland, M. Elahinia, J. Walker, and H. Meier, "Visions, concepts and strategies for smart Nitinol actuators and complex Nitinol structures produced by Additive Manufacturing." pp. V001T01A006-V001T01A006.

[130] N. S. Moghaddam, S. Saedi, A. Amerinatanzi, A. Jahadakbar, E. Saghaian, H. Karaca, and M. Elahinia, "Influence of SLM on compressive response of NiTi scaffolds." p. 105960H.

[131] C. Haberland, *Additive Verarbeitung von NiTi-Formgedächtniswerkstoffen mittels Selective-Laser-Melting*: Shaker, 2012.

[132] M. Bram, M. Bitzer, H. Buchkremer, and D. Stöver, “Reproducibility study of NiTi parts made by metal injection molding,” *Journal of materials engineering and performance,* vol. 21, no. 12, pp. 2701-2712, 2012.

[133] J. Mentz, J. Frenzel, M. F.-X. Wagner, K. Neuking, G. Eggeler, H. P. Buchkremer, and D. Stöver, “Powder metallurgical processing of NiTi shape memory alloys with elevated transformation temperatures,” *Materials Science Engineering: A,* vol. 491, no. 1-2, pp. 270-278, 2008.

[134] I. Shishkovsky, E. Y. Tarasova, and A. Petrov, “The synthesis of a biocomposite based on nickel titanium and hydroxyapatite under selective laser sintering conditions,” *Technical Physics Letters,* vol. 27, no. 3, pp. 211-213, 2001.

[135] Y. I. Arutyunov, L. Zhuravel, A. Pokoev, and N. Shishkovskij, “Structure and properties of the Ni-Ti intermetallic phases synthesized upon selective laser

sintering: II. Structure and corrosion behaviour," *Fizika Metallov i Metallovedenie,* vol. 93, no. 2, pp. 85-88, 2002.

[136] I. Shishkovsky, "Shape memory effect in porous volume NiTi articles fabricated by selective laser sintering," *Technical physics letters,* vol. 31, no. 3, pp. 186-188, 2005.

[137] I. Shishkovsky, L. Volova, M. Kuznetsov, Y. G. Morozov, and I. Parkin, "Porous biocompatible implants and tissue scaffolds synthesized by selective laser sintering from Ti and NiTi," *Journal of Materials Chemistry,* vol. 18, no. 12, pp. 1309-1317, 2008.

[138] A. T. Clare, P. R. Chalker, S. Davies, C. J. Sutcliffe, and S. Tsopanos, "Selective laser melting of high aspect ratio 3D nickel–titanium structures two way trained for MEMS applications," *International Journal of Mechanics and Materials in Design,* vol. 4, no. 2, pp. 181-187, 2008.

[139] H. Meier, and C. Haberland, "Experimental studies on selective laser melting of metallic parts," *Materialwissenschaft und Werkstofftechnik,* vol. 39, no. 9, pp. 665-670, 2008.

[140] H. Meier, C. Haberland, and J. Frenzel, "Structural and functional properties of NiTi shape memory alloys produced by selective laser melting," *Innovative developments in design and manufacturing: advanced research in virtual and rapid prototyping*, pp. 291-296, 2011.

[141] C. Haberland, H. Meier, and J. Frenzel, "On the properties of Ni-rich NiTi shape memory parts produced by selective laser melting." pp. 97-104.

[142] C. Haberland, M. Elahinia, J. M. Walker, H. Meier, and J. Frenzel, “On the development of high quality NiTi shape memory and pseudoelastic parts by additive manufacturing,” *Smart materials structures,* vol. 23, no. 10, pp. 104002, 2014.

[143] S. Dadbakhsh, M. Speirs, J. P. Kruth, J. Schrooten, J. Luyten, and J. Van Humbeeck, “Effect of SLM parameters on transformation temperatures of shape memory nickel titanium parts,” *Advanced Engineering Materials,* vol. 16, no. 9, pp. 1140-1146, 2014.

[144] S. Dadbakhsh, M. Speirs, J.-P. Kruth, and J. Van Humbeeck, “Influence of SLM on shape memory and compression behaviour of NiTi scaffolds,” *CIRP Annals,* vol. 64, no. 1, pp. 209-212, 2015.

[145] T. Bormann, B. Müller, M. Schinhammer, A. Kessler, P. Thalmann, and M. de Wild, “Microstructure of selective laser melted nickel–titanium,” *Materials characterization,* vol. 94, pp. 189-202, 2014.

[146] T. Bormann, R. Schumacher, B. Müller, M. Mertmann, and M. de Wild, “Tailoring selective laser melting process parameters for NiTi implants,” *Journal of materials engineering and performance,* vol. 21, no. 12, pp. 2519-2524, 2012.

[147] T. Bormann, M. de Wild, F. Beckmann, and B. Müller, "Assessing the morphology of selective laser melted NiTi-scaffolds for a three-dimensional quantification of the one-way shape memory effect." p. 868914.

[148] M. Speirs, S. Dadbakhsh, S. Buls, J. Kruth, J. Van Humbeeck, J. Schrooten, and J. Luyten, "The effect of SLM parameters on geometrical characteristics of open porous NiTi scaffolds."

[149] T. Habijan, C. Haberland, H. Meier, J. Frenzel, J. Wittsiepe, C. Wuwer, C. Greulich, T. Schildhauer, and M. Köller, “The biocompatibility of dense and porous nickel–titanium produced by selective laser melting,” *Materials Science and Engineering: C,* vol. 33, no. 1, pp. 419-426, 2013.

[150] S. Saedi, A. S. Turabi, M. T. Andani, C. Haberland, H. Karaca, and M. Elahinia, “The influence of heat treatment on the thermomechanical response of Ni-rich NiTi alloys manufactured by selective laser melting,” *Journal of Alloys Compounds,* vol. 677, pp. 204-210, 2016.

[151] T. Duerig, and K. Melton, "Designing with the shape memory effect." pp. 581-597.

[152] M. Mehrpouya, A. Gisario, A. Rahimzadeh, M. Nematollahi, K. S. Baghbaderani, and M. Elahinia, “A prediction model for finding the optimal laser parameters in additive manufacturing of NiTi shape memory alloy,” *The International Journal of Advanced Manufacturing Technology,* vol. 105, no. 11, pp. 4691-4699, 2019.

[153] H. M. Frost, and E. Schönau, “The" muscle-bone unit" in children and adolescents: a 2000 overview,” *Journal of Pediatric Endocrinology Metabolism,* vol. 13, no. 6, pp. 571-590, 2000.

[154] D. Stoeckel, “Nitinol medical devices and implants,” *Minimally invasive therapy & allied technologies,* vol. 9, no. 2, pp. 81-88, 2000.

[155] M. Simon, R. Kaplow, E. Salzman, and D. Freiman, “A vena cava filter using thermal shape memory alloy: experimental aspects,” *Radiology,* vol. 125, no. 1, pp. 89-94, 1977.

[156] T. Duerig, K. Melton, D. Stockel, and C. Wayman, "Engineering Aspects of Shape Memory Alloys,(1990)," *Butter worth-Heinemam, London*, 1990.

[157] G. F. Andreasen, and T. B. Hilleman, "An evaluation of 55 cobalt substituted Nitinol wire for use in orthodontics," *The Journal of the American Dental Association,* vol. 82, no. 6, pp. 1373-1375, 1971.

[158] L. Torrisi, "The NiTi superelastic alloy application to the dentistry field," *Bio-medical materials and engineering,* vol. 9, no. 1, pp. 39-47, 1999.

[159] G. Airoldi, G. Riva, and M. Vanelli, "Superelasticity and shape memory effect in NiTi orthodontic wires," *Journal de Physique IV,* vol. 5, no. C8, pp. C8-1205-C8-1210, 1995.

[160] S. Idelsohn, J. Pena, D. Lacroix, J. Planell, F. Gil, and A. Arcas, "Continuous mandibular distraction osteogenesis using superelastic shape memory alloy (SMA)," *Journal of Materials Science: Materials in Medicine,* vol. 15, no. 4, pp. 541-546, 2004.

[161] B. V. D. Thanopoulos, C. V. Laskari, G. S. Tsaousis, A. Zarayelyan, A. Vekiou, and G. S. Papadopoulos, "Closure of atrial septal defects with the Amplatzer occlusion device: preliminary results," *Journal of the American College of Cardiology,* vol. 31, no. 5, pp. 1110-1116, 1998.

[162] K. A. Hausegger, A. H. Cragg, J. Lammer, M. Lafer, F. Flückiger, G. E. Klein, M. H. Sternthal, and E. Pilger, "Iliac artery stent placement: clinical experience with a nitinol stent," *Radiology,* vol. 190, no. 1, pp. 199-202, 1994.

[163] J. Laborde, N. Borenstein, L. Behr, B. Farah, and J. Fajadet, "Percutaneous implantation of the corevalve aortic valve prosthesis for patients presenting high

risk for surgical valve replacement," *EuroIntervention: journal of EuroPCR in collaboration with the Working Group on Interventional Cardiology of the European Society of Cardiology,* vol. 1, no. 4, pp. 472-474, 2006.

[164] D. S. Levi, N. Kusnezov, and G. P. Carman, "Smart materials applications for pediatric cardiovascular devices," *Pediatric research,* vol. 63, no. 5, pp. 552, 2008.

[165] A. Johnson, and F. Alicandri, "Thermoconstrictive surgical appliance," Google Patents, 1974.

[166] M. Geetha, A. K. Singh, R. Asokamani, and A. K. Gogia, "Ti based biomaterials, the ultimate choice for orthopaedic implants–a review," *Progress in materials science,* vol. 54, no. 3, pp. 397-425, 2009.

[167] R. G. Tang, K. R. Dai, and Y. Q. Chen, "Application of a NiTi staple in the metatarsal osteotomy," *Bio-medical materials engineering,* vol. 6, no. 4, pp. 307-312, 1996.

[168] K. Dai, X. Hou, Y. Sun, R. Tang, S. Qiu, and C. Ni, "Treatment of intra-articular fractures with shape memory compression staples," *Injury,* vol. 24, no. 10, pp. 651-655, 1993.

[169] Z. Laster, A. MacBean, P. Ayliffe, and L. Newlands, "Fixation of a frontozygomatic fracture with a shape-memory staple," *The British journal of oral maxillofacial surgery,* vol. 39, no. 4, pp. 324, 2001.

[170] O. N. Schipper, S. E. Ford, P. W. Moody, B. Van Doren, and J. K. Ellington, "Radiographic Results of Nitinol Compression Staples for Hindfoot and Midfoot Arthrodeses," *Foot ankle international,* vol. 39, no. 2, pp. 172-179, 2018.

[171] M. Schmerling, M. Wilkov, A. Sanders, and J. Woosley, "A proposed medical application of the shape memory effect: a NiTi Harrington Rod for the treatment of scoliosis," *Shape Memory Effects in Alloys*, pp. 563-574: Springer, 1975.

[172] J. O. Sanders, A. Sanders, R. More, and R. Ashman, "A preliminary investigation of shape memory alloys in the surgical correction of scoliosis," *Spine,* vol. 18, no. 12, pp. 1640-1646, 1993.

[173] A. E. Sanders, J. O. Sanders, and R. B. More, "Nitinol spinal instrumentation and method for surgically treating scoliosis," Google Patents, 1994.

[174] D. Wever, J. Elstrodt, A. Veldhuizen, and J. v Horn, "Scoliosis correction with shape-memory metal: results of an experimental study," *European Spine Journal,* vol. 11, no. 2, pp. 100-106, 2002.

[175] R. Contro, V. Dallolio, G. Franzoso, D. Gastaldi, and P. Vena, "Biomechanical study of a pathologic lumbar functional spinal unit and a possible surgical treatment through the implant of an interspinous device," 2005.

[176] S. Abkowitz, J. M. Siergiej, and R. R. Regan, "Titanium-nickel alloy manufacturing methods," Google Patents, 1972.

[177] L. Petrini, and F. Migliavacca, "Biomedical applications of shape memory alloys," *Journal of Metallurgy,* vol. 2011, 2011.

[178] J. S. Sandhu, W. T. DeCarbo, and M. H. Hofbauer, "Digital arthrodesis with a one-piece memory nitinol intramedullary fixation device: a retrospective review," *Foot and ankle specialist,* vol. 6, no. 5, pp. 364-366, 2013.

[179] M. B. Canales, M. C. Razzante, D. J. Ehredt Jr, and C. O. Clougherty, "A simple method of intramedullary fixation for proximal interphalangeal arthrodesis," *The Journal of Foot and Ankle Surgery,* vol. 53, no. 6, pp. 817-824, 2014.

[180] D. TARNIŢĂ, D. Tarniţă, D. Popa, D. Grecu, R. TARNIŢĂ, D. Niculescu, and F. Cismaru, "Numerical simulations of human tibia osteosynthesis using modular plates based on Nitinol staples," *Romanian Journal of Morphology embryology,* vol. 51, no. 1, pp. 145-150, 2010.

[181] D. Carter, T. Orr, and D. Fyhrie, "Relationships between loading history and femoral cancellous bone architecture," *Journal of Biomechanics,* vol. 22, no. 3, pp. 231-244, 1989.

[182] S. C. Cowin, "Bone remodeling of diaphyseal surfaces by torsional loads: theoretical predictions," *Journal of biomechanics,* vol. 20, no. 11-12, pp. 1111-1120, 1987.

[183] D. B. Kimmel, "A paradigm for skeletal strength homeostasis," *Journal of Bone Mineral Research,* vol. 8, no. S2, pp. S515-S522, 1993.

[184] D. J. Hadjidakis, and I. I. Androulakis, "Bone remodeling," *Annals of the New York Academy of Sciences,* vol. 1092, no. 1, pp. 385-396, 2006.

[185] H. M. Frost, "Skeletal structural adaptations to mechanical usage (SATMU): 1. Redefining Wolff's law: the bone modeling problem," *The Anatomical Record,* vol. 226, no. 4, pp. 403-413, 1990.

[186] T. Sugiyama, L. B. Meakin, W. J. Browne, G. L. Galea, J. S. Price, and L. E. Lanyon, "Bones' adaptive response to mechanical loading is essentially linear

between the low strains associated with disuse and the high strains associated with the lamellar/woven bone transition," *Journal of bone mineral research* vol. 27, no. 8, pp. 1784-1793, 2012.

[187] H. M. Frost, "Bone "mass" and the "mechanostat": a proposal," *The anatomical record,* vol. 219, no. 1, pp. 1-9, 1987.

[188] L. Lanyon, "Using functional loading to influence bone mass and architecture: objectives, mechanisms, and relationship with estrogen of the mechanically adaptive process in bone," *Bone,* vol. 18, no. 1, pp. S37-S43, 1996.

[189] H. Frost, "A determinant of bone architecture. The minimum effective strain," *Clinical orthopaedics and related research*, no. 175, pp. 286-292, 1983.

[190] C. Straatsma, "Principles Of Bone Remodeling," LWW, 1963.

[191] D. B. Burr, M. R. Forwood, D. P. Fyhrie, R. B. Martin, M. B. Schaffler, and C. H. Turner, "Bone microdamage and skeletal fragility in osteoporotic and stress fractures," *Journal of Bone and Mineral Research,* vol. 12, no. 1, pp. 6-15, 1997.

[192] R. B. Martin, and D. B. Burr, *Structure, function, and adaptation of compact bone*: Raven Pr, 1989.

[193] R. Huiskes, H. Weinans, and B. Van Rietbergen, "The relationship between stress shielding and bone resorption around total hip stems and the effects of flexible materials," *Clinical orthopaedics and related research*, pp. 124-134, 1992.

[194] J. Black, *Biological performance of materials: fundamentals of biocompatibility*: Crc Press, 2005.

[195] T. Albrektsson, P.-I. Brånemark, H.-A. Hansson, and J. Lindström, "Osseointegrated titanium implants: requirements for ensuring a long-lasting,

direct bone-to-implant anchorage in man," *Acta Orthopaedica Scandinavica,* vol. 52, no. 2, pp. 155-170, 1981.

[196] L. F. Cooper, "Biologic determinants of bone formation for osseointegration: clues for future clinical improvements," *The Journal of prosthetic dentistry,* vol. 80, no. 4, pp. 439-449, 1998.

[197] D. Puleo, and A. Nanci, "Understanding and controlling the bone–implant interface," *Biomaterials,* vol. 20, no. 23-24, pp. 2311-2321, 1999.

[198] G. I. Taylor, G. Miller, and F. J. Ham, "The free vascularized bone graft. A clinical extension of microvascular techniques," *Plastic reconstructive surgery,* vol. 55, no. 5, pp. 533-544, 1975.

[199] D. W. Hutmacher, "Scaffolds in tissue engineering bone and cartilage," *The Biomaterials: Silver Jubilee Compendium*, pp. 175-189: Elsevier, 2006.

[200] H. Petite, V. Viateau, W. Bensaid, A. Meunier, C. de Pollak, M. Bourguignon, K. Oudina, L. Sedel, and G. Guillemin, "Tissue-engineered bone regeneration," *Nature biotechnology,* vol. 18, no. 9, pp. 959, 2000.

[201] D. A. Hidalgo, "Fibula free flap: a new method of mandible reconstruction," *Plastic reconstructive surgery,* vol. 84, no. 1, pp. 71-79, 1989.

[202] H. Abukawa, M. Shin, W. B. Williams, J. P. Vacanti, L. B. Kaban, and M. J. Troulis, "Reconstruction of mandibular defects with autologous tissue-engineered bone," *Journal of oral maxillofacial surgery,* vol. 62, no. 5, pp. 601-606, 2004.

[203] A. Abbas, "Reconstruction skeleton for the lower human jaw using CAD/CAM/CAE," *Journal of King Saud University-Engineering Sciences,* vol. 24, no. 2, pp. 159-164, 2012.

[204] M. L. Urken, D. Buchbinder, P. D. Costantino, U. Sinha, D. Okay, W. Lawson, and H. F. Biller, "Oromandibular reconstruction using microvascular composite flaps: report of 210 cases," *Archives of otolaryngology–head & neck surgery,* vol. 124, no. 1, pp. 46-55, 1998.

[205] P. G. Cordeiro, J. J. Disa, D. A. Hidalgo, and Q. Y. Hu, "Reconstruction of the mandible with osseous free flaps: a 10-year experience with 150 consecutive patients," *Plastic & reconstructive surgery,* vol. 104, no. 5, pp. 1314-1320, 1999.

[206] F. W. Virgin, T. A. Iseli, C. E. Iseli, J. Sunde, W. R. Carroll, J. S. Magnuson, and E. L. Rosenthal, "Functional outcomes of fibula and osteocutaneous forearm free flap reconstruction for segmental mandibular defects," *The Laryngoscope,* vol. 120, no. 4, pp. 663-667, 2010.

[207] O. N. Militsakh, A. Werle, N. Mohyuddin, E. B. Toby, J. D. Kriet, D. I. Wallace, D. A. Girod, and T. T. Tsue, "Comparison of radial forearm with fibula and scapula osteocutaneous free flaps for oromandibular reconstruction," *Archives of Otolaryngology–Head and Neck Surgery,* vol. 131, no. 7, pp. 571-575, 2005.

[208] A. S. Herford, and E. Ellis, "Use of a locking reconstruction bone plate/screw system for mandibular surgery," *Journal of oral and maxillofacial surgery,* vol. 56, no. 11, pp. 1261-1265, 1998.

[209] B. T. Goh, S. Lee, H. Tideman, and P. J. Stoelinga, "Mandibular reconstruction in adults: a review," *International journal of oral maxillofacial surgery,* vol. 37, no. 7, pp. 597-605, 2008.

[210] J. Boyd, P. J. Gullane, L. E. Rotstein, D. H. Brown, and J. C. Irish, “Classification of mandibular defects,” *Plastic and reconstructive surgery,* vol. 92, no. 7, pp. 1266-1275, 1993.

[211] M. L. Urken, H. Weinberg, C. Vickery, D. Buchbinder, W. Lawson, and H. F. Biller, “Oromandibular reconstruction using microvascular composite free flaps: report of 71 cases and a new classification scheme for bony, soft-tissue, and neurologic defects,” *Archives of Otolaryngology–Head Neck Surgery,* vol. 117, no. 7, pp. 733-744, 1991.

[212] J. S. Brown, C. Barry, M. Ho, and R. Shaw, “A new classification for mandibular defects after oncological resection,” *The Lancet Oncology,* vol. 17, no. 1, pp. e23-e30, 2016.

[213] E. Ellis III, and L. R. Walker, “Treatment of mandibular angle fractures using one noncompression miniplate,” *Journal of oral and maxillofacial surgery,* vol. 54, no. 7, pp. 864-871, 1996.

[214] L. Trebing, and J. Thalgott, "Locking plate and bone screw," Google Patents, 1997.

[215] R. A. Young, "Locking bone plate," Google Patents, 2010.

[216] J. Lee, M. Kim, W. Choi, P. Yoon, K. Ahn, H. Myung, S. Hwang, B. Seo, J. Choi, and P. Choung, “Concomitant reconstruction of mandibular basal and alveolar bone with a free fibular flap,” *International journal of oral and maxillofacial surgery,* vol. 33, no. 2, pp. 150-156, 2004.

[217] J. Fennis, P. Stoelinga, and J. Jansen, “Mandibular reconstruction: a histological and histomorphometric study on the use of autogenous scaffolds, particulate

cortico-cancellous bone grafts and platelet rich plasma in goats," *International Journal of Oral Maxillofacial Surgery,* vol. 33, no. 1, pp. 48-55, 2004.

[218] N. Shayesteh Moghaddam, "Toward patient specific long lasting metallic implants for mandibular segmental defects," 2015.

[219] M. C. Kennady, M. R. Tucker, G. E. Lester, and M. J. Buckley, "Histomorphometric evaluation of stress shielding in mandibular continuity defects treated with rigid fixation plates and bone grafts," *International journal of oral maxillofacial surgery,* vol. 18, no. 3, pp. 170-174, 1989.

[220] T. Nagasao, J. Miyamoto, T. Tamaki, and H. Kawana, "A comparison of stresses in implantation for grafted and plate-and-screw mandible reconstruction," *Oral Surgery, Oral Medicine, Oral Pathology, Oral Radiology, Endodontology,* vol. 109, no. 3, pp. 346-356, 2010.

[221] R. R. Bos, F. Rozema, G. Boering, A. Nijenhuis, A. Pennings, and A. Verwey, "Bio-absorbable plates and screws for internal fixation of mandibular fractures: A study in six dogs," *International journal of oral and maxillofacial surgery,* vol. 18, no. 6, pp. 365-369, 1989.

[222] N. S. Moghaddam, M. Elahinia, M. Miller, and D. Dean, "Enhancement of Bone Implants by Substituting Nitinol for Titanium (Ti-6Al-4V): A Modeling Comparison." pp. V001T03A031-V001T03A031.

[223] T. S. Kaneko, J. S. Bell, M. R. Pejcic, J. Tehranzadeh, and J. H. Keyak, "Mechanical properties, density and quantitative CT scan data of trabecular bone with and without metastases," *Journal of biomechanics,* vol. 37, no. 4, pp. 523-530, 2004.

[224] M. T. Andani, N. S. Moghaddam, C. Haberland, D. Dean, M. J. Miller, and M. Elahinia, “Metals for bone implants. Part 1. Powder metallurgy and implant rendering,” *Acta biomaterialia,* vol. 10, no. 10, pp. 4058-4070, 2014.

[225] S. T. Lovald, J. D. Wagner, and B. Baack, “Biomechanical optimization of bone plates used in rigid fixation of mandibular fractures,” *Journal of oral and maxillofacial surgery,* vol. 67, no. 5, pp. 973-985, 2009.

[226] K. Martin. "titanium-osteosynthesis," 2/21/2020, 20220.

[227] T. Nagasao, J. Miyamoto, and H. Kawana, “Biomechanical evaluation of implant placement in the reconstructed mandible,” *International Journal of Oral and Maxillofacial Implants,* vol. 24, no. 6, 2009.

[228] R. Mehrabi, M. Kadkhodaei, and A. Ghaei, "Numerical implementation of a thermomechanical constitutive model for shape memory alloys using return mapping algorithm and microplane theory." pp. 351-354.

[229] R. Mehrabi, and M. Kadkhodaei, “3D phenomenological constitutive modeling of shape memory alloys based on microplane theory,” *Smart Materials Structures,* vol. 22, no. 2, pp. 025017, 2013.

[230] M. Shirani, R. Mehrabi, M. T. Andani, M. Kadkhodaei, M. Elahinia, and M. T. Andani, "A modified microplane model using transformation surfaces to consider loading history on phase transition in shape memory alloys." pp. V001T01A001-V001T01A001.

[231] D. A. Hidalgo, “Titanium miniplate fixation in free flap mandible reconstruction,” *Annals of plastic surgery,* vol. 23, no. 6, pp. 498-507, 1989.

[232] T. W. Korioth, D. P. Romilly, and A. G. Hannam, "Three-dimensional finite element stress analysis of the dentate human mandible," *American Journal of Physical Anthropology,* vol. 88, no. 1, pp. 69-96, 1992.

[233] S. Saedi, S. E. Saghaian, A. Jahadakbar, N. S. Moghaddam, M. T. Andani, S. M. Saghaian, Y. C. Lu, M. Elahinia, and H. E. Karaca, "Shape memory response of porous NiTi shape memory alloys fabricated by selective laser melting," *Journal of Materials Science: Materials in Medicine,* vol. 29, no. 4, pp. 40, 2018.

[234] A. W. Hansen, L. T. Führ, L. M. Antonini, D. J. Villarinho, C. E. B. Marino, and C. d. F. Malfatti, "The electrochemical behavior of the niti alloy in different simulated body fluids," *Materials Research,* vol. 18, no. 1, pp. 184-190, 2015.

[235] A. R. Pelton, J. Dicello, and S. Miyazaki, "Optimisation of processing and properties of medical grade Nitinol wire," *Minimally Invasive Therapy & Allied Technologies,* vol. 9, no. 2, pp. 107-118, 2000.

[236] S. Shabalovskaya, J. Anderegg, F. Laab, P. Thiel, and G. Rondelli, "Surface conditions of Nitinol wires, tubing, and as-cast alloys. The effect of chemical etching, aging in boiling water, and heat treatment," *Journal of Biomedical Materials Research Part B: Applied Biomaterials: An Official Journal of The Society for Biomaterials, The Japanese Society for Biomaterials, and The Australian Society for Biomaterials and the Korean Society for Biomaterials,* vol. 65, no. 1, pp. 193-203, 2003.

[237] B. Katona, E. Bognár, B. Berta, P. Nagy, and K. Hirschberg, "Chemical etching of nitinol stents," *Acta of bioengineering and biomechanics,* vol. 15, no. 4, 2013.

[238] C. Ma, M. T. Andani, H. Qin, N. S. Moghaddam, H. Ibrahim, A. Jahadakbar, A. Amerinatanzi, Z. Ren, H. Zhang, and G. L. Doll, "Improving surface finish and wear resistance of additive manufactured nickel-titanium by ultrasonic nano-crystal surface modification," *Journal of Materials Processing Technology,* vol. 249, pp. 433-440, 2017.

[239] N. S. Moghaddam, S. Saedi, A. Amerinatanzi, A. Hinojos, A. Ramazani, J. Kundin, M. J. Mills, H. Karaca, and M. Elahinia, "Achieving superelasticity in additively manufactured NiTi in compression without post-process heat treatment," *Scientific reports,* vol. 9, no. 1, pp. 1-11, 2019.

[240] R. F. Hamilton, B. A. Bimber, M. T. Andani, and M. Elahinia, "Multi-scale shape memory effect recovery in NiTi alloys additive manufactured by selective laser melting and laser directed energy deposition," *Journal of Materials Processing Technology,* vol. 250, pp. 55-64, 2017.

[241] S. Saedi, N. S. Moghaddam, A. Amerinatanzi, M. Elahinia, and H. E. Karaca, "On the effects of selective laser melting process parameters on microstructure and thermomechanical response of Ni-rich NiTi," *Acta Materialia,* vol. 144, pp. 552-560, 2018.

[242] M. Nematollahi, G. Toker, S. Saghaian, J. Salazar, M. Mahtabi, O. Benafan, H. Karaca, and M. Elahinia, "Additive manufacturing of ni-rich nitihf 20: Manufacturability, composition, density, and transformation behavior," *Shape Memory and Superelasticity,* vol. 5, no. 1, pp. 113-124, 2019.

[243] W. Simka, M. Kaczmarek, A. Baron-Wiecheć, G. Nawrat, J. Marciniak, and J. Żak, “Electropolishing and passivation of NiTi shape memory alloy,” *Electrochimica Acta,* vol. 55, no. 7, pp. 2437-2441, 2010.

[244] A. Bagheri, M. J. Mahtabi, and N. Shamsaei, “Fatigue behavior and cyclic deformation of additive manufactured NiTi,” *Journal of Materials Processing Technology,* vol. 252, pp. 440-453, 2018.

[245] A. Jahadakbar, “The Additively Manufactured Porous NiTi and Ti-6Al-4V in Mandibular Reconstruction: Introducing the Stiffness-Matched and the Variable Stiffness Options for the Reconstruction Plates,” University of Toledo, 2016.

[246] S. A. Chirani, M. Barati, L. Saint-Sulpice, P. Bayati, M. Nematollahi, M. Mahtabi, A. Jahadakbar, and M. Elahinia, "Self-heating and fatigue of additively manufactured NiTi." pp. 11-13.